MAX PLANCK INSTUTUTE FOR POLYMER RESEARCH

JOHANNES GUTENBERG UNIVERSITÄT MAINZ

Advances in Solution Processing of Organic Semiconductors for Organic Semiconducting Devices

DISSERTATION

Zur Erlangung des Grades

„Doktor der Naturwissenschaften“

am Fachbereich Chemie, Pharmazie, Geographie und Geowissenschaften

der Johannes Gutenberg-Universität und in Kooperation

mit dem Max-Planck-Institut für Polymerforschung

in Mainz

David Trieb

Geboren in Worms

Mainz, 2024

Dekan: Prof. Dr. Eva Rentschler, Johannes Gutenberg-Universität Mainz

1. Gutachter:

2. Gutachter:

Tag der mündlichen Prüfung: 22.01.2025

Abstract

Organic semiconductors have emerged as an intriguing and well-explored class of materials in recent years, with the potential to replace traditional inorganic semiconductors. One advantage of organic semiconductors is their reliance on hydrocarbons, eliminating the need for expensive and typically toxic inorganic elements, which pose risks to both human health and the environment. Another benefit of organic semiconducting materials lies in the ability to precisely tailor their properties through molecular design and synthesis, yielding organic semiconductors specifically optimized for desired functionalities.

Common to all organic semiconductors is the presence of a conjugated system comprising alternating single and double bonds. Such systems can be realized in both small molecules and polymers. Charge transport within these systems occurs through hopping of charge carriers within this conjugated framework. By judiciously selecting side chains for polymers or functional groups for molecules, the properties of the organic semiconductor can be tailored. For instance, the emission wavelength of emitters for organic light-emitting diodes (OLEDs) can be tuned across the entire spectrum, or side chains can be added to enhance solubility.

This work focuses on the fabrication of films of organic semiconductors from solution and the preparation of blends of organic semiconductors with other materials to enhance the properties of the films.

In Chapter 4 of this study, the possibility of increasing the permittivity of organic semiconductor films is investigated. A high permittivity is necessary to achieve high efficiency in organic solar cells (OSCs). Organic semiconductors typically have a low permittivity. Therefore, they were mixed with materials possessing a high permittivity to achieve a film with an increased permittivity. It was found that this approach is feasible in principle; however, it negatively affects the charge transport through the organic semiconductor.

In Chapter 5, the improvement of electron injection into organic semiconductors is investigated. To achieve this, a method is employed whereby a thin layer of approximately 4 nm thickness is placed between the semiconductor and the electrode. Previous studies have demonstrated that this approach is effective for efficiently injecting holes. It was found that this principle can also be applied to negative charge carriers. Additionally, a method was developed to apply this thin layer from solution onto an organic semiconductor film.

In Chapter 6, the feasibility of manufacturing OLEDs from solution is investigated, aiming for comparable efficiency to OLEDs produced through other manufacturing methods. Initially, the processability of various emitters from solution was examined, along with the blending of emitters with polymers to enhance the physical stability of films against subsequently applied layers. It was observed that blending films with polymers for use in OLEDs is feasible in principle; however, a reduction in efficiency occurs when an additional layer from solution is to be processed onto it.

Zusammenfassung

Innerhalb der letzten Jahre haben sich organische Halbleiter zu einer interessanten und gut untersuchten Klasse entwickelt, welche das Potential hat, klassische anorganisch Halbleiter zu ersetzten. Ein Vorteil von organische Halbleiter ist, dass diese auf Kohlenwasserstoff basieren und daher ohne teure und in der Regel toxische, sowohl für den Menschen als auch für die Umwelt, anorganische Elemente auskommen. Ein weiterer Vorteil von organischen Halbleitermaterialen ist die Möglichkeit, diese mittels molekularem Design gezielt zu synthetisieren, um organische Halbleiter zu erhalten, welche genau auf die zu erfüllenden Aufgaben abgestimmt sind.

Gemeinsam ist allen organischen Halbleitern, dass diese ein durchkonjugierbares System aus Einfach- und Doppelbindungen besitzen. Solche Systeme können sich sowohl in einfachen Molekülen als auch in Polymeren realisiert werden. Der Ladungstransport innerhalb dieser Systeme wird durch das hüpfen von Ladungsträgern innerhalb dieses konjugierbaren Systems realisiert. Durch geschickte Wahl der Seitenketten von Polymeren oder funktionellen Gruppen an Molekülen können dann die Eigenschaften des organischen Halbleiters angepasst werden. Beispielsweise kann die Emissionswellenlänge von Emittern für organische Leuchtdioden (OLED) über das gesamte Spektrum eingestellt werden oder es können Seitenketten zur Erhöhung der Löslichkeit hinzugefügt werden.

In dieser Arbeit liegt der Fokus auf der Herstellung von Filmen der organische Halbleiter aus Lösung und der Herstellung von Mischungen von organischen Halbleitern mit anderen Materialen um die Eigenschaften der Filme zu verbessern.

In Kapitel 4 dieser Arbeit wird untersucht, ob es möglich ist, die Permitivität von Filmen organischer Halbleiter zu erhöhen. Eine hohe Permitivität ist notwendig, um in Organischen Solarzellen (OSC) eine möglichst hohe Effizienz zu erhalten. Organische Halbleiter haben in der Regel eine niedrige Permitivität. Daher wurden diese mit Materialen mit einer hohen Permitivität gemischt um so einen Film mit einer erhöhten Permitivität zu erreichen. Dabei hat sich herausgestellt, dass die prinzipiell möglich ist, allerdings dabei der Ladungstransport durch den organischen Halbleiter negativ beeinflusst wird.

In Kapitel 5 wird untersucht, wie die Injektion negativer Ladungen in organische Halbleiter verbessert werden kann. Dazu wird ein Verfahren angewendet, eine dünne Schicht von ca. 4 nm Dicke zwischen den Halbleiter und die Elektrode zu platzieren. Es wurde bereits in früheren Studien gezeigt, dass dies ein geeigneter Weg ist, um positive Ladungen effizient zu injizieren. Es stellte sich heraus, dass dieses Prinzip auch auf negative Ladungsträger angewandt werden kann. Daneben wurde auch eine Methode entwickelt, diese dünne Schicht aus Lösung auf einen organischen Halbleiterfilm aufzutragen.

In Kapitel 6 wird untersucht, ob OLEDs auch aus Lösung hergestellt werden können und dabei genauso effizient sind wie OLEDs aus anderen Herstellungsverfahren. Dazu wurde zuerst die Prozessierbarkeit von verschiedenen Emitter aus Lösung untersucht sowie die Mischung von Emitter mit Polymeren um die physikalische Stabilität von Filmen gegenüber darauf aufgetragenen Schichten zu verbessern. Es hat sich gezeigt, dass die Mischung von Filmen mit

Polymeren für den Einsatz in OLEDs prinzipiell möglich ist, jedoch tritt eine Effizienz-verringerung ein wenn eine weitere Schicht darauf aus Lösung prozessiert werden soll.

Table of content

1. Introduction

In the last decade organic semiconductors have become increasingly popular for various applications, with as main driver OLED displays with a current market size of 60 billion USD. These commercial OLEDs consist of complex multi-layer stacks of in vacuum evaporated small organic molecules, making them expensive. A strong cost reduction would be obtained when OLED displays could be printed from solution. This thesis aims to provide deeper insights into the process of depositing organic semiconductors from solution. Solution processing offers a convenient, quick and cheap way to deposit organic semiconductors even on large scale. As part of this approach, this thesis explores the fabrication of blended films comprising organic semiconductors and other materials, with the aim of enhancing film characteristics such as physical stability. Additionally, blends have the potential to impart additional features to the film beyond organic semiconducting properties, such as an increased dielectric constant. By investigating the possibilities for fabricating organic semiconducting films from solution, this thesis seeks to advance the understanding of this versatile deposition method.

2. Theoretical Background

In this chapter, the physical and chemical background for the studies in this thesis will be provided. Therefore, the chapter is divided into five sections. First, the working principles of organic semiconductors will be explained along with examples of organic semiconductors. The second section will offer insights into the application of organic semiconductors with a particular focus on their utilization in organic light emitting diodes (OLED) and organic solar cells (OSC), as detailed in the subsequent sections. Finally, the last section will elucidate the deposition techniques of organic semiconductors.

2.1. Organic Semiconductors

Organic semiconductors are evolving as an intriguing alternative to well established inorganic semiconductors. Composed primarily of carbon and hydrogen, organic semiconductors eliminate the need for silicon as well as heavy metals, infamous for their toxicity and high cost.[1] The diverse variety of organic molecules facilitates tailored design to precisely match the requirements of specific applications.[2] For instance, the emission wavelength of organic semiconductors used in OLEDs can be finely tuned across the entire visible spectrum.[3] In the subsequent section, the mechanism of charge transport in organic semiconductors will be explained, accompanied by an introduction to the two primary classes: polymeric organic semiconductors and small molecule organic semiconductors.

2.1.1. Charge transport in organic materials

For organic materials to exhibit semiconductivity, there are certain requirements for the molecular structure. An example of such semiconducting material is polyacetylene, depicted in Figure 2.1. As for all polymers, it is characterized by the repetitive arrangement of monomers in a chain-like structure. Said polymer is composed of CH-groups interconnected by both σ and π bonds. These different bonds originate from the hybridization of carbon atomic orbitals. In polyacetylene, carbon exhibits a sp^2 hybridization.[4] Therefore, each carbon atom forms three σ bonds and one π bond, with the σ bonds connecting to adjacent carbon atoms and hydrogen atom, while the π bond extends to an adjacent carbon atom. Consequently, this arrangement yields a structure in which single and double bonds alternate. The π-bonds in the polymer are delocalized within their mesomeric boundary structure. The semiconducting behavior of polyacetylene is attributed to the presence of these delocalized π-bonds.[5] For the discovery of (semi)conductance in this material, Alan Heeger, Alan MacDiarmid and Hideki Shirakawa were awarded with the Nobel Prize in Chemistry 2000.[6]

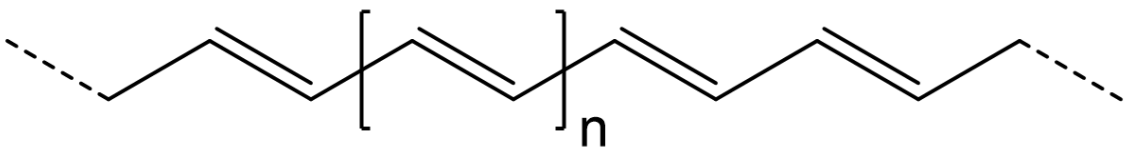

Figure 2.1. Chemical structure of polyacetylene.

The charge transport in such organic semiconductors differs from their inorganic counterparts. Unlike inorganic semiconductors, where charge transport is appropriately

described by a band model, such an approach is unsuitable for organic semiconductors. This discrepancy arises from the inherent disorder present in organic semiconductors, distinguishing them from their ordered inorganic counterparts.[7] A more fitting depiction of the behavior of organic semiconductors involves considering the highest occupied molecular orbital (HOMO) and the lowest unoccupied molecular orbital (LUMO). The energy distribution within these states exhibits a Gaussian-shaped density of states (DOS), as illustrated in Figure 2.2 (left). Within these Gaussian DOS profiles, charge transport manifests through a hopping process, where charges leap from one state to another, as depicted schematically in Figure 2.2 (right).[8] Notably, hole transport takes place in the HOMO-DOS, while the electron transport will occur in the LUMO-DOS.

Owing to the low dielectric constant of organic semiconductors ($\epsilon \approx 3$) coulombic effects play a significant role, in stark contrast to inorganic semiconductors, where charges are treated as free charges at room temperature.[9] This discrepancy arises due to the distinctive electrostatic environment of organic semiconductors. Additionally, the absence of strong orbital interactions contributes to a short mean free pathway for charge carriers in organic semiconductors. Consequently, charges become localized within the material and are transported through a hopping process from one site to the next.[10] This hopping process necessitates an overlap of the wave functions between the two sites involved in the charge transfer.

Disparities in the charge transport mechanisms between organic and inorganic semiconductors can also be observed in the temperature-dependence of the charge-carrier mobility. In the case of inorganic semiconductors, an increase in temperature results in a reduction of the mobility. This phenomenon can be explained by considering that elevated temperatures lead to an increased presence of phonons and other lattice distortions within the inorganic semiconductor crystal. Consequently, the mean free pathway for charge carriers diminishes, leading to a decrease in current flow.[11] Conversely, in organic semiconductors, an increase in temperature correlates with an increase of mobility.[12] This phenomenon arises from the surplus energy available to charges, enabling them to overcome activation energy barriers during the hopping process from site to site, analogues to the principles outlined in Marcus theory.[13] In this framework, charges are located within parabolic potential wells and necessitate a specific energy input to overcome these potential barriers and transition to an adjacent well.[14,15] This temperature dependent behavior aligns as well with the principles of the energetic disorder in organic semiconductors.[16] The difference in temperature dependent charge transport illustrates the distinctions between organic and inorganic semiconductors.

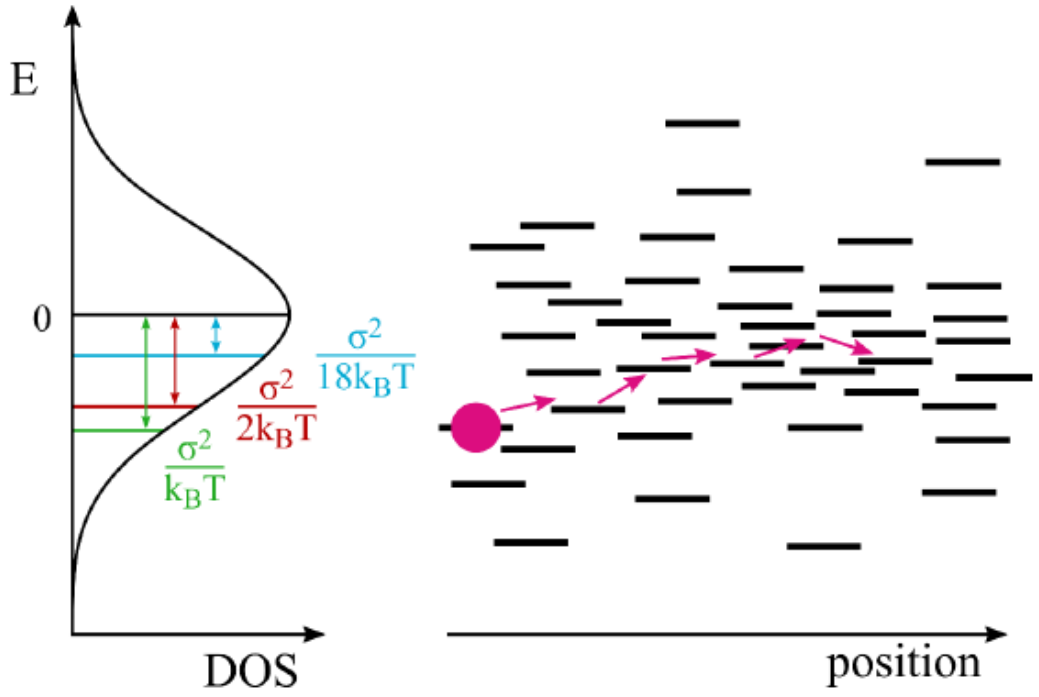

Figure 2.2. Left. Typical Gaussian DOS of an organic semiconducting material. Right. Schematic plot of hopping of a charge carrier (purple) through an organic semiconductor. Black lines indicate free states from the organic semiconductor. Figure adopted from [17].

2.1.2. Polymers as organic semiconductors

To utilize the semiconducting attributes for applications such as polymeric light-emitting diodes (PLEDs), numerous polymers have been developed. A common feature among these polymers is the presence of a conjugated backbone, which gives the semiconducting properties. An extensively studied category is represented by poly(*p*-phenylene vinylene) (PPV) derivatives, exemplified by poly[2-methoxy-5-(2-ethylhexyloxy)-1,4-phenylenevinylene] (MEH-PPV) and super-yellow p-phenylene vinylene (SY-PPV) (structural formula in Figure 2.3(a) and (b), respectively).[18] Both of these polymers consist of a PPV-backbone characterized by complete conjugation. The different side chains attached to the benzene rings enable fine-tuning of the polymer's emission wavelength and enhance the solubility, thereby optimizing processability.[19] These design considerations facilitate the creation of PLEDs with tailored emission characteristics and improved handling during fabrication processes.

Beyond their application in PLEDs, polymeric organic semiconductors find utility in various other technological domains, including organic transistors and organic solar cells.[20] In this thesis, the semiconducting polymer poly[[N,N'-bis(2-octyldodecyl)naphthalene-1,4,5,8-bis(dicarboximide)-2,6-diyl]-alt-5,5'-(2,2'-bithiophene)] (PNDI(2OD)-2T)), serves as an illustration of an n-type organic semiconductor, meaning the charge transport is predominantly electron dominated. The chemical structure is depicted in Figure 2.3(c). This n-type organic semiconductor exhibits an electron mobility between 1 to 8 $cm^2 V^{-1} s^{-1}$.[21] These materials are suitable for applications in transistors and p-n junctions, avoiding the need for traditional inorganic materials such as silicon.

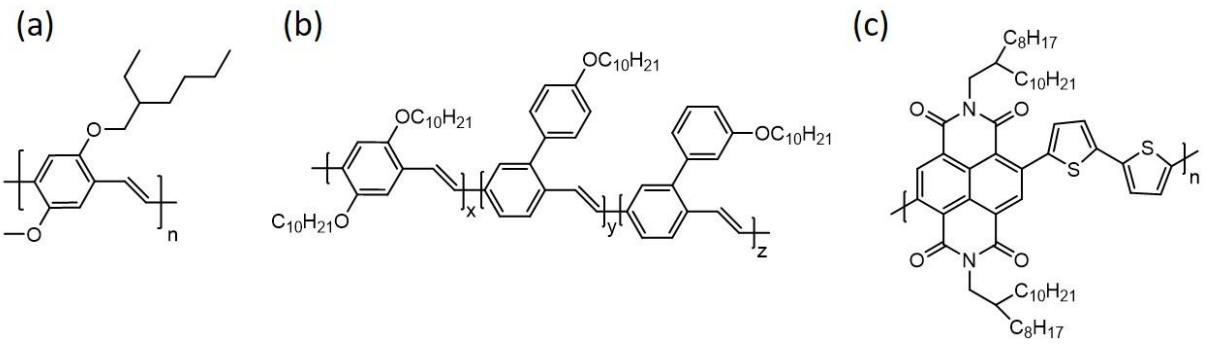

Figure 2.3. Chemical structures of examples of polymeric organic semiconductors. (a) MEH-PPV. (b) Super-Yellow-PPV. (SY-PPV) (c) PNDI(2OD)-2T.

Polymers, while serving as organic semiconductors in OLEDs, exhibit a drawback in terms of their relatively low internal quantum efficiency (IQE) (see Subsection 2.3.5) when used in OLEDs. This limitation arises from two main factors. Firstly, polymers can only be processed from solution, restricting their incorporation into relatively simple device structures only (see Section 2.3).[22] Secondly, the inherent disorder within polymeric chains has until recently restricted the synthesis of polymers to those only emitting fluorescence for applications in OLEDs.[23] Consequently, the theoretical maximum IQE is capped at 25 %, as only 25 % of the generated excitons in such a polymer are singlet excitons, capable of decaying through fluorescence (compare with Figure 2.4(a)). Such an exciton can be conceptualized as a coulombically bound electron hole pair. In response to these challenges, small molecule organic semiconductors have been developed to mitigate the limitations associated with polymers. The subsequent section will introduce these materials and their potential to overcome the efficiency constraints posed by polymeric organic semiconductors in OLEDs.

2.1.3. Small molecules as organic semiconductors

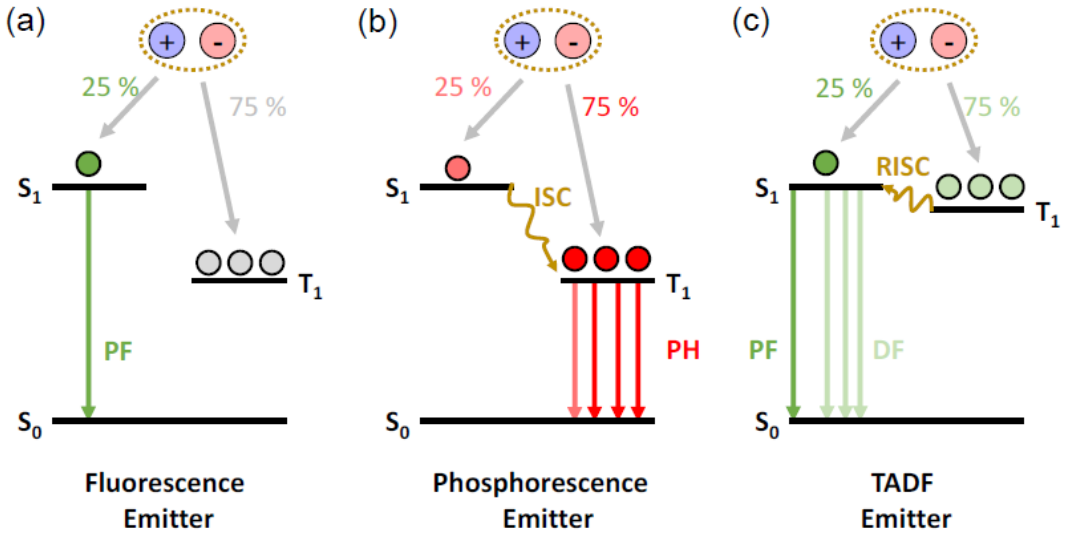

Figure 2.4. Jablonski diagrams of working principles of the three generation of OLED-emitters. (a) Fluorescent emitter only showing prompt fluorescence (PF) from the S_1 state. (b) Phosphorescent emitter emitting phosphorescence (PH) from the T_1 state. (c) TADF emitter emitting fluorescent light via PF or as delayed fluorescence (DF) after reverse inter system crossing (RISC) from the T_1 to the S_1 state. Figure adopted from [24].

To advance the efficiency of OLEDs, enhancements in the emitter compounds have been essential. Consequently, a multitude of small molecules have been engineered to replace the semiconducting polymer emitters in OLEDs. Analogous to semiconducting polymers, these small molecules feature a conjugated system, and their charge transport mechanisms align with the principles discussed in Subsection 2.1.1.[25]

The small molecules utilized in OLEDs can be categorized into three generations. The initial generation comprises fluorescent emitters, with tris(8-hydroxyquinoline)aluminum (Alq_3) serving as an example, as illustrated in Figure 2.4(a). However, as this first generation of fluorescent emitters works according to the same principles as discussed in Subsection 2.1.2 for polymers used in PLEDs and shown in Figure 2.4(a), the internal quantum efficiency is capped at a theoretical maximum of 25 %.[26]

The theoretical maximum for the IQE in fluorescent emitters arises from the formation of excitons within these emitters. An exciton can be conceptualized as a coulombically bound hole in the HOMO together with an electron in the LUMO of the organic semiconductor. Both the hole and the electron possess a spin, which can be either parallel or antiparallel to each other. When the spins are antiparallel, their sum S is 0. The multiplicity M depends on the sum of the spins, as shown in the following equation:

$$M = 2S + 1. \tag{1}$$

For $S = 0$, this yields $M = 1$, indicating that there is only one state for this total spin, known as a singlet state. Conversely, for parallel spins, *S* sums up to 1. According to equation 1, this results in $M = 3$, meaning that three states are possible in this scenario. Hence, these states are referred to as triplet states. Since all four states (three triplet states and one singlet state) have the same probability of being created by the formation of an exciton, the probability for the exciton to be in a singlet state (and to decay via fluorescence) is limited to 25 %. To overcome the limitations posed by the first-generation emitters and use the potential of the 75 % triplet excitons, a second generation of small molecules was developed.[27] The decisive difference compared to the fluorescent emitters is the utilization of phosphorescent light emission by the second-generation emitters, illustrated in Figure 2.4(b). Phosphorescence is a process wherein triplet excited states relax to the ground singlet state. This relaxation would typically be forbidden by quantum mechanics due to the required spin flip; however, heavy metals are incorporated into these compounds to facilitate spin-orbit coupling, enabling the spin flip to occur efficiently.[28] To maximize efficiency, not only the 75 % triplet excitons but also the 25 % singlet excitons should be utilized. To transfer the singlet excitons to triplet excitons, a process called inter-system crossing (ISC) is employed. This process, also challenged by the spin selection rule, is made possible by the efficient spin-orbit coupling facilitated by heavy metals. The exemplary phosphorescent emitter tris(2-phenylpyridine)iridium(III) ($Ir(ppy)_3$), depicted in Figure 2.5(b), highlights the incorporation of heavy metals in these compounds. However, it is essential to note that the use of heavy metals in these compounds poses certain challenges. These metals are often rare and, consequently, expensive.[29] Moreover, many of these metals are toxic, complicating the handling and recycling of materials incorporating them.[30]

In response to the limitations associated with the second generation of emitters, Uoyama et al. utilized another approach in 2012 to develop purely organic emitters for OLEDs, offering a theoretical efficiency of up to 100 %.[31] They synthesized materials, which work with the principle of thermally activated delayed fluorescence (TADF). The design rule for TADF materials is to minimize the energy gap between the excited singlet state (S_1) and the triplet state (T_1), as illustrated in Figure 2.4(c).[32] This design allows the generated triplet excitons to undergo a process known as reverse inter-system crossing (rISC), transitioning from T_1 back to S_1, followed by decay from S_1 via fluorescence.[33] Consequently, all excited states can, in principle, decay through fluorescence without reliance on heavy metals. To realize such a minimal energy gap between the S_1 and T_1 states, it is essential to minimize the wave function overlap between the ground and excited states (HOMO and LUMO) of the emitter. This objective can be achieved through molecular design by coupling an electron-rich donor with an electron-deficient acceptor. When these groups are connected in a perpendicular arrangement, the HOMO and LUMO become localized in the donor and acceptor, respectively, leading to reduced interaction between these states.[34] However, it is important to note that a fully perpendicular system would result in a low photoluminescence quantum yield (PLQY), which would diminish the efficiency of the emitter.[35] An exemplary TADF material synthesized by Uoyama et al. is 1,2,3,5-tetrakis(carbazol-9-yl)-4,6-dicyanobenzene (4CzIPN), depicted in Figure 2.5(c), where the carbazoles are the donors while the nitrile-groups together with the central phenyl ring serve as acceptor.[31] The research to synthesize new TADF emitters is subject of current investigations.[36, 37]

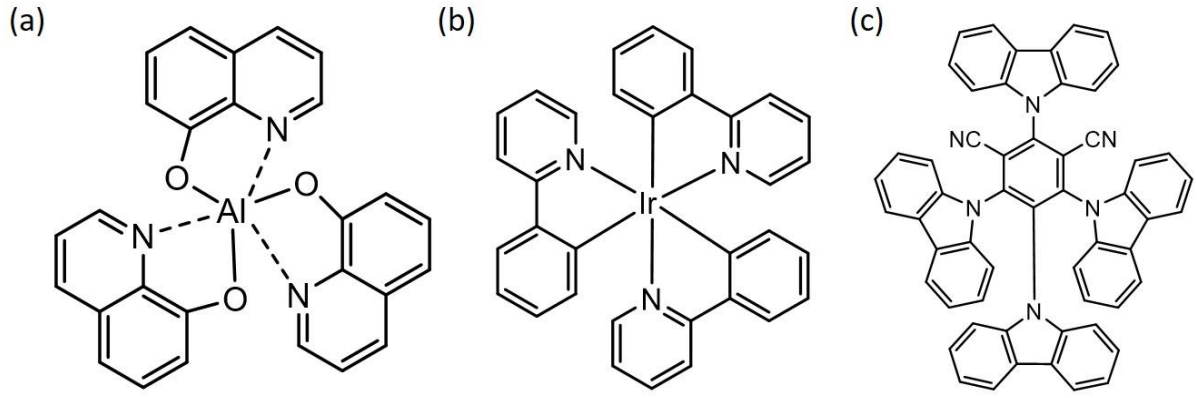

Figure 2.5. Examples for the three generation of small molecule emitters for OLEDs. (a) 1st generation fluorescent emitter Alq_3 (b) 2nd generation phosphorescent emitter $Ir(ppy)_3$ (c) 3rd generation TADF emitter 4CzIPN.

In addition to their application in OLEDs, organic semiconducting small molecules have been specifically developed for use in organic solar cells, particularly as non-fullerene acceptors.[38] In this context, these molecules serve as electron transport material, facilitating the transport of the generated negative charges to the extraction electrode. For a more in-depth understanding of the mechanisms underlying organic solar cells, further details can be found in Section 2.4 Furthermore, in OLEDs, organic semiconductors that do not emit light are employed to transport injected charges to the emissive layer. These materials fall into various classes, such as electron transport, electron blocking, hole transport, and hole blocking materials.[39] Each material is specifically designed to fulfill its intended function, particularly on the HOMO and LUMO levels of these materials.[40] The tailored design of these organic

semiconductors ensures their effectiveness in facilitating charge transport within the specific layers of OLED devices and therefore increase the efficiency.

2.2. Physics and operation of organic semiconducting devices

In order to make use of the organic semiconductors introduced in the preceding section, they are incorporated into organic semiconducting devices. In this context, a device refers to the application of organic semiconductors within an electric circuit, facilitating practical access to their semiconducting properties. These properties of organic semiconductors can be harnessed for various applications such as emitting light in OLEDs, converting light to electrical power in OSCs, or acting as a switch in organic field transistors (OFET). Such devices serve as organic counterparts to their inorganic semiconductor equivalents. To fully utilize the potential of organic semiconductors in these devices, efficient charge injection (or extraction) and an in-depth understanding of charge carrier transport are critical factors in designing efficient devices. In this chapter, first methods for achieving efficient charge injection are explored, followed by an investigation of charge carrier mobilities in what are known as single carrier devices.

2.2.1. Charge injection into organic semiconductors

Organic semiconductors do not inherently generate charges; therefore, charges must be injected for OLEDs or generated through light absorption in the case of OSCs. Efficient charge carrier injection or extraction is crucial for all organic semiconducting devices.[41] The most efficient way of charge injection is the establishment of an ohmic contact. In case of such contacts, the quantity of charge carriers in the organic semiconductor is not constrained by the injection from the electrodes. Instead, it is limited by the number of carriers that can be introduced and effectively transported by the organic semiconductors themselves.[42] Therefore, the aim for any organic semiconducting device is to establish such an ohmic contact.

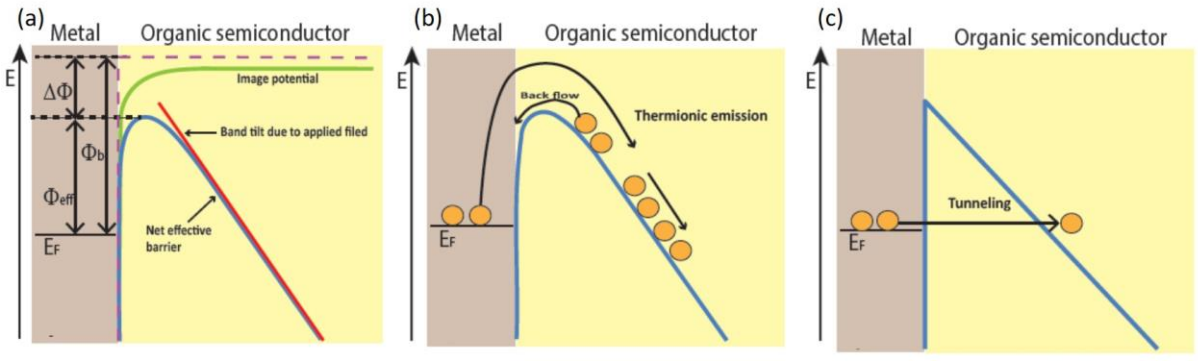

Figure 2.6. Schematic overview of the effects at the metal/semiconductor interface. (a) Band bending at the interface due to the build-up of an image potential (green line) and the applied electric field (red line). The blue line shows the resulting net band bending. (b) Thermionic accumulation of charges at the interface due to high fields and low mobility of the charge carriers in the organic semiconductor. (c) Tunneling of charge carriers from the metal through the barrier into the organic semiconductor via Fowler-Nordheim tunneling. Figure adopted from [43].

The simplest method of creating a contact involves a metal directly in contact with an organic semiconductor. However, this direct interface does usually not form an ohmic contact.[44] As depicted in Figure 2.6(a), a potential (Φ_b) between the fermi level of the metal and the LUMO (or HOMO in case of hole injection) builds up. When an electron is injected into the organic semiconductor, a positive charge accumulates on the metal surface, referred to as an image charge. The resulting potential, the image potential Φ_i is given by:[45]

$$\Phi_i = \frac{-q}{(16\pi\varepsilon x)}. \tag{2}$$

Where *q* is the elementary charge, ε the dielectric constant and *x* the distance between the charge and the metal surface. As a consequence of this phenomenon, the effective barrier Φ_{eff} is lower then Φ_b under the application of an electric field. The difference between those two values, denoted as $\Delta\Phi$ is dependent on the external electric field *E*, which is applied to the device. The value of $\Delta\Phi$ can be described by the following equation:

$$\Delta\Phi = \sqrt{\frac{qE}{4\pi\varepsilon}}. \tag{3}$$

This mechanism of barrier lowering at the interface between a metal and an organic semiconductor under the application of an electric field, is often referred to in literature as "image-force barrier lowering".[46] Despite the lowering of the barrier, it is important to note that a certain amount of energy for charge injection remains necessary.

To overcome this effective barrier Φ_{eff}, charges can be injected via thermionic emission. In this process, charges surmount the barrier using thermal energy for injection into the organic semiconductor. While the Richardson-Schottky equation aptly describes this mechanism for inorganic semiconductors, it requires modifications for application to organic semiconductors.[47] This adaptation is essential due to the typically lower charge carrier mobilities in organic semiconductors, often differing by orders of magnitudes from their inorganic counterparts. To accommodate this difference, the effective number of states *N* where the charges can be injected in as well as the charge carrier mobility μ are incorporated into the equation.[48] Thus, the current density *J* injected into the organic semiconductor can be expressed as:

$$J = qN\mu E(0)\exp\left(-\frac{q\Phi_{eff}}{kT}\right). \tag{4}$$

The equation includes *E(0)*, which represents the electric field at the metal-semiconductor interface. This formulation acknowledges that buildup of charges occurs at the interface between the metal and organic semiconductor. As a result, charges have the potential to flow back from the organic semiconductor to the metal, as illustrated in the schematic in Figure 2.6(b).[49]

In instances where the temperature is insufficient enabling thermionic emission or when the organic semiconductor layer is very thin, charge injection can alternatively occur through tunneling through the barrier from the metal into the organic semiconductor, as depicted in

Figure 2.6(c). This tunneling phenomenon is commonly referred to as Fowler-Nordheim tunneling.[50]

The mechanism for charge injection into organic semiconductors discussed above assumes the perfect formation of the interface between the metal and organic semiconductors. However, in reality, chemical reactions between the metal and the organic semiconductor may occur at the interface. These reactions can alter the chemical potential at the interface and introduce additional dipoles.[51] As a consequence, charges transferred from the metal into the organic semiconductor may be injected into tail states of the DOS. This phenomenon leads to the pinning of the Fermi level and, in turn, an increase in the energy gap.[52]

This process is highly dependent on the deposition of the materials at the interface.[53] It has also been reported that the DOS in the initial few nanometers of the organic semiconductor differs from the DOS in the bulk.[54] This leads to additional band bending effects at the interface, resulting in the formation of a charge injection barrier. Typically, this barrier has a magnitude of 0.3 – 0.4 eV.[55]

The aforementioned effects constrain the efficiency of charge injection into organic electronic devices, thereby diminishing their overall performance. Imperfect charge injection can further contribute to errors, such as the underestimation of charge carrier mobilities, in case it is not recognized that charge injection hampers the current, rather than the charge transport inside the semiconductor. In response to these limitations on injection currents, strategies have been developed to establish ohmic contacts.[42]

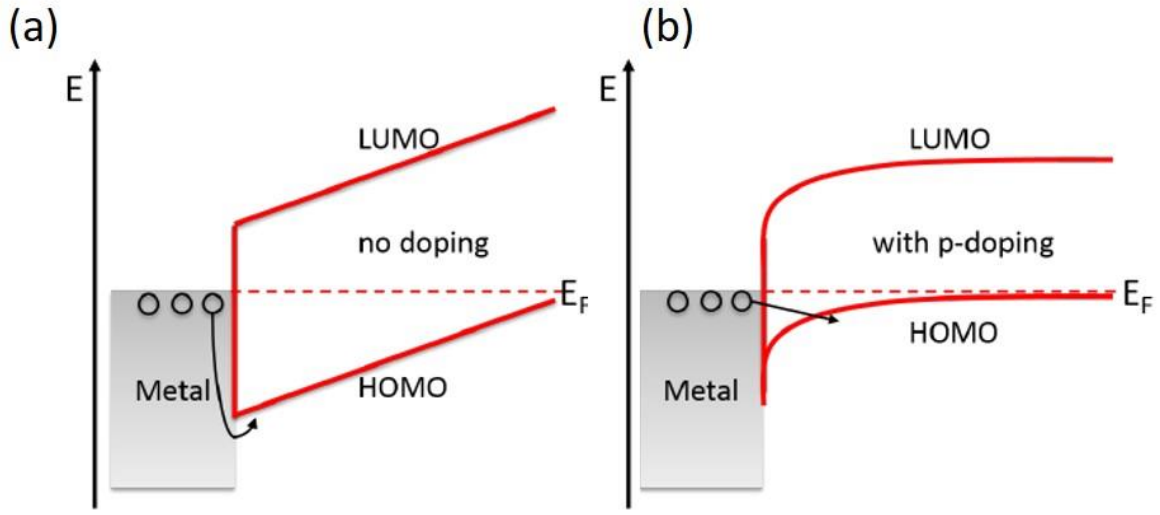

Figure 2.7. schematic drawing of the energy levels at the interface with and without doping of the organic semiconductor. (a) Undoped organic semiconductor showing a big injection barrier. (b) Doping of the organic semiconductor shows a big reduction of the injection barrier. Figure edited from [43].

One of the strategies utilized to establish an ohmic contact involves doping the organic semiconductor. To facilitate ohmic hole injection, a p-doped layer is introduced between the metal and the organic semiconductor. P-type doping is achieved by the utilization of a small concentration of an electron-accepting material that captures an electron, resulting in the generation of a hole in the HOMO. Upon contact of a metal with a p-doped semiconductor,

band bending occurs in the semiconductor to align the Fermi levels on both sides of the interface. This substantial reduction in the injection barrier is evident in Figure 2.7(b), in stark contrast to a device without doping, as illustrated in Figure 2.7(a).[56] In an undoped organic semiconductor, the charge density is too low to induce band bending. A parallel approach can be adopted to achieve ohmic electron injection through n-type doping with an electron donor material, with the mechanism operating inverse to p-type doping.[57]

An alternative approach for establishing an ohmic contact involves the electrostatic decoupling of the organic semiconductor from the metal electrode. This method requires the insertion of a thin interlayer, approximately 2-5 nm in thickness, between the metal electrode and the organic semiconductor.[58] A crucial criterion for realizing electrostatic decoupling is an energy offset for the HOMO/LUMO levels between the organic semiconductor and the interlayer material. In the case of ohmic hole injection, the absolute value of the ionization energy (IE) of the interlayer should be higher than the HOMO of the organic semiconductor. For instance, the use of a C_{60} interlayer serves as an example to achieve ohmic hole contact.[59] Conversely, for ohmic electron injection, the electron affinity (EA) of the interlayer material should be smaller than the LUMO of the organic semiconductor. This has been demonstrated using TPBi as an interlayer material.[60] It should be noted that in the selection of the interlayer material, considerations extend beyond the energy levels. Some interlayer materials may aggregate on the organic semiconductor-interlayer interface, thereby reducing the electronic decoupling effect the interlayer should have.[58]

2.2.2. Single-carrier devices

To explore the behavior of the two distinct charge carriers, holes and electrons, within the semiconductor—particularly their mobilities, charge injection and contributions to charge transport in a double carrier device—it is imperative to employ single carrier devices. As the term "single" implies, these devices exclusively involve only one species of charge carriers in the charge transport process. This characteristic enables the scrutiny of mobility and other properties concerning either hole or electron transport, facilitating a more profound understanding of the functionalities of organic semiconductors.[19, 61] For the investigation of the hole transport, hole-only devices (HO) are fabricated, which can be also be applied analogously for electron transport by means of electron-only devices (EO).

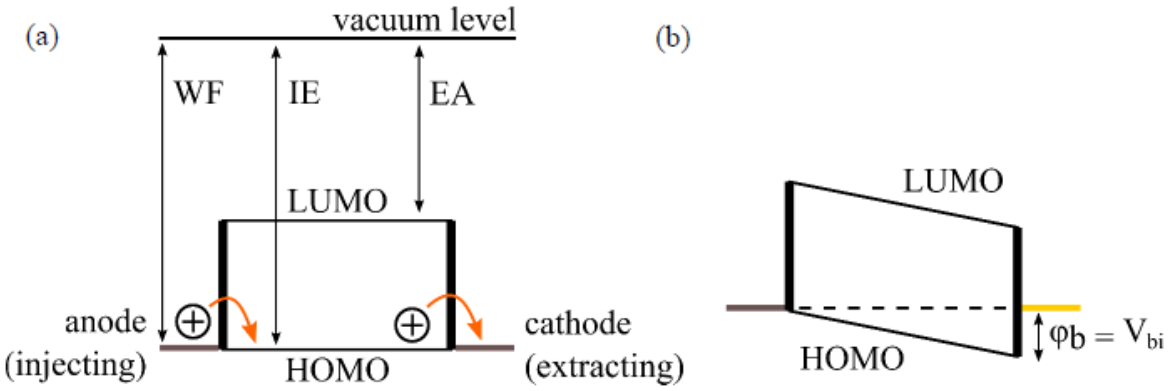

Figure 2.8. Schematic drawing of hole only devices. (a) Symmetric hole only designs with two ohmic contacts. (b) Asymmetrical hole only device with an injection barrier ϕb on the right side. Figure adopted from [17].

To fabricate a single-carrier device, the selection of electrodes plays a critical role. For HO-devices, it is essential to use electrode materials that form an ohmic contact with the HOMO of the organic semiconductor. This requirement is met by materials with a work function (WF) equal to or higher than the IE of the organic semiconductor, as illustrated in Figure 2.8(a). Typically, high work function materials such as MoO_3, indium-tin-oxide (ITO), or Au are utilized as electrode materials.[62] As discussed in the previous section, the incorporation of a thin C_{60} layer might be necessary to achieve an ohmic hole contact. The high work function of these materials inhibits the injection of electrons into the LUMO. Therefore, the device current comprised solely of a hole current. When a contact is ohmic, meaning no injection barrier is present, the resulting device current is just depending on the mobility of the holes. In a J-V diagram of a device were both electrodes are ohmic contacts, the forward bias and the reverse bias should exhibit symmetry. In such devices with two ohmic contacts the resulting current for forward and revers bias only depend on the applied electric field and the charge carrier mobilities and is independent of the injection from the electrodes. An example of such a J-V curve is depicted in Figure 2.9(a), black symbols. In case, one contact is not ohmic, as shown in Figure 2.8(b), a barrier builds up (ϕ_b). This results in an asymmetric J-V characteristic, as is shown in Figure 2.9(a), red symbols.

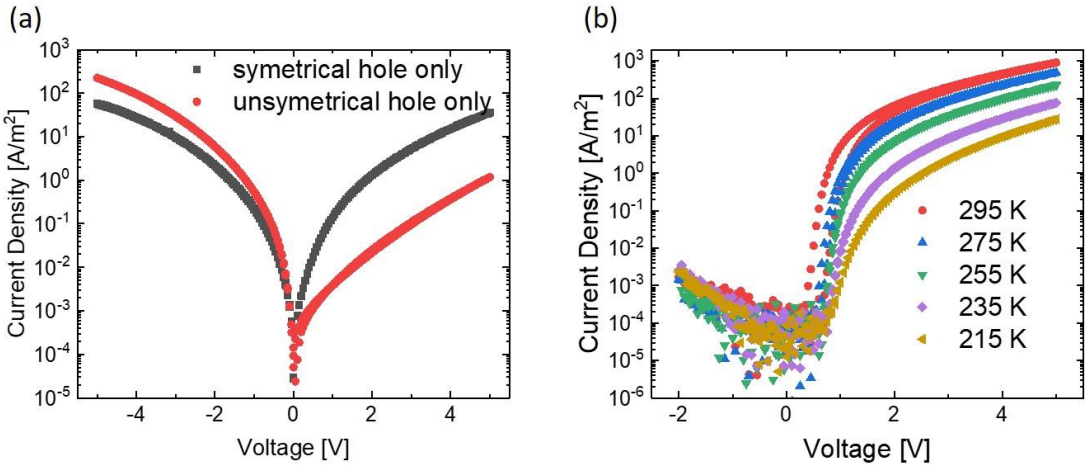

Figure 2.9. Typical J-V curves for hole- and electron-only devices. (a) Hole only devices with a symmetric device current (black) and an asymmetric device current (red). (b) Electron only device measured at different temperatures.

To create an electron-only device, it is essential for the electrodes to align with the LUMO of the organic semiconductor to facilitate efficient electron injection. This alignment is typically achieved by utilizing low work function metals like LiF, Ba, or Ca, which match the EA of the organic semiconductor.[63] Due to practical considerations in the fabrication process, only one electrode is made of such material and is dedicated to electron injection. A counter electrode of bare aluminum is used for extraction of electrons. The work function of aluminum is sufficiently low to prevent hole injection under forward bias. However, due to the offset between the work function and the electron affinity of the semiconductor, electron injection from aluminum under reverse bias is limited. As a result, the *J-V* curve displays a strongly reduced current in reverse bias. Figure 2.9(b) illustrates an example of a J-V curve for such an electron-only device.

In an ideal scenario, where charge injection is achieved through ohmic contacts, the current in a single-carrier device is limited by the buildup of space charge in the semiconductor. As a result, a space-charge-limited current is established, of which the magnitude depends on the charge-carrier mobility. For an intrinsic semiconductor, free of charge traps, and neglecting diffusion, the space-charge-limited current is described by the Mott-Gurney law, which reads:

$$J = \frac{9}{8}\varepsilon\mu\frac{V^2}{L^3}. \tag{5}$$

Here, *J* is the current density, ε the dielectric constant, μ represents the respective charge carrier mobility, and *L* denotes the thickness of the semiconducting layer in the device. The application of this formula assumes trap-free charge transport, signifying the absence of states within the bandgap of the organic semiconductor that can be occupied by charge carriers.[64] If charge carriers are caught in such trap states, they can no longer contribute to charge transport.

As the charge-carrier mobility in an organic semiconductor decreases with decreasing temperature, as discussed in Subsection 2.1.1, and the space-charge-limited current is directly proportional to the mobility, the current density also decreases with decreasing temperature. A device lacking temperature dependence implies that the measured current does not represent organic semiconducting behavior but is primarily attributable to leakage current. Leakage currents typically originate from direct contact between top and bottom electrode. The temperature-dependent *J-V* measurements of single-carrier devices allow for the extraction of charge-carrier mobilities as a function of temperature. This is commonly achieved through numerical simulation of these curves by a drift diffusion model. This model elucidates the behavior of the charge transport with a term for the drift of the charge carriers induced by the electric field, along with a second term that describes transport due to a gradient of the charge density.[65] Within this model, the mobility of the charge carriers can be described by an extended gaussian disorder model (EGDM) as proposed by Pasveer et al.[66] Within the EGDM, the mobility of charge carriers is characterized by three parameters: μ_0, which denotes the mobility in the absence of an electric field, *σ,* which represents the energetic disorder of the DOS, and *a,* the average hopping distance.[17] A typical temperature-dependent electron-only curve utilized for modelling is depicted in Figure 2.9(b).

2.2.3. Double-carrier devices

Once the characteristics of the individual charge carriers are understood, the subsequent step involves fabricating devices where both carriers are utilized. Such devices are organic diodes, such as OLEDs and organic solar cells. In these devices, one electrode contacts the LUMO for electron injection or extraction, while another electrode connects to the HOMO for hole injection or extraction. A diverse range of devices has been developed to use the unique properties of organic semiconductors. While this work primarily focuses on OLEDs and OSCs, these devices will be explored in greater detail in the subsequent sections.

2.3. Working principles of OLEDs

An important application for organic semiconductors are OLEDs. In these devices, charges are injected into the organic semiconductor to recombine and produce light. This section will provide an overview of the development of OLEDs, covering aspects such as device design, electrical characteristics, and the recombination processes taking place in OLEDs. The discussion will also include the determination of the OLED efficiency and processes that may impact and reduce efficiency.

2.3.1. Historical background of OLEDs

The initial utilization of organic materials to generate light dates back to the 1960s, employing anthracene crystals as the emissive layer. However, these early OLEDs required several hundred volts for light extraction due to a relatively thick layer of 10-20 µm of the organic material, rendering them impractical for applications.[67] The first OLEDs based on thin films of evaporated small molecules were developed at Kodak and published in 1987 by Tang and van Slycke.[68] A few years later, in 1990, it was discovered that semiconducting emissive polymers like PPV could also be employed in OLEDs.[18] This breakthrough opened the field for the development of various polymers designed to create OLEDs with a diverse range of colors. Additionally, the advantages for solution deposition techniques such as spin coating or slot die coating became apparent in these PLEDs.[19]

To enhance OLED systems and elevate their efficiencies, multilayer OLEDs were introduced.[68] These devices consist of several layers, each serving a specific role to improve the overall efficiency. The exploration of TADF materials for OLEDs in 2012 marked the discovery of a new class of emitters.[31] The ongoing interest and development of OLEDs are evident from both academia and industry, as illustrated by the continuous publication of research papers and patents year after year, as depicted in Figure 2.10.

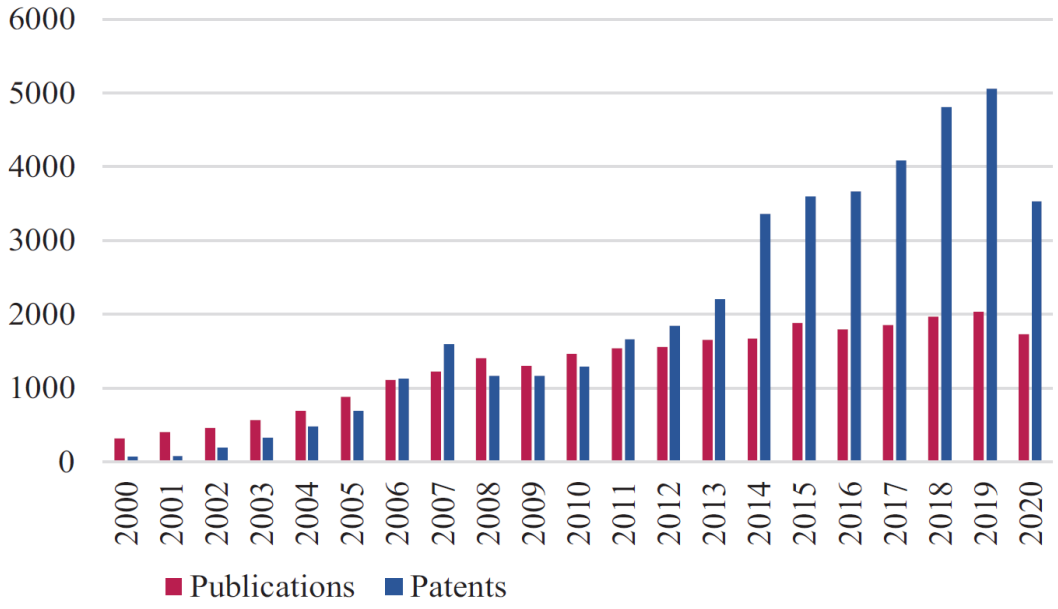

Figure 2.10. Number of publications and patents for OLEDs over the last 20 years. Figure adopted from [69].

2.3.2. Device design of OLEDs

The initial development of OLEDs featured a straightforward device design. A polymeric organic semiconductor, serving as the emissive layer, was sandwiched between two electrodes.[18] A schematic representation of such a structure is depicted in Figure 2.11(a). The requirement for the electrodes is that the work function of one electrode aligns with the LUMO for electron injection, while the other electrode aligns with the HOMO for hole injection. When an electric field with a positive bias voltage is applied, electrons and holes are injected into the semiconductor. These injected charges can form excitons which subsequently can decay to emit light.[70]

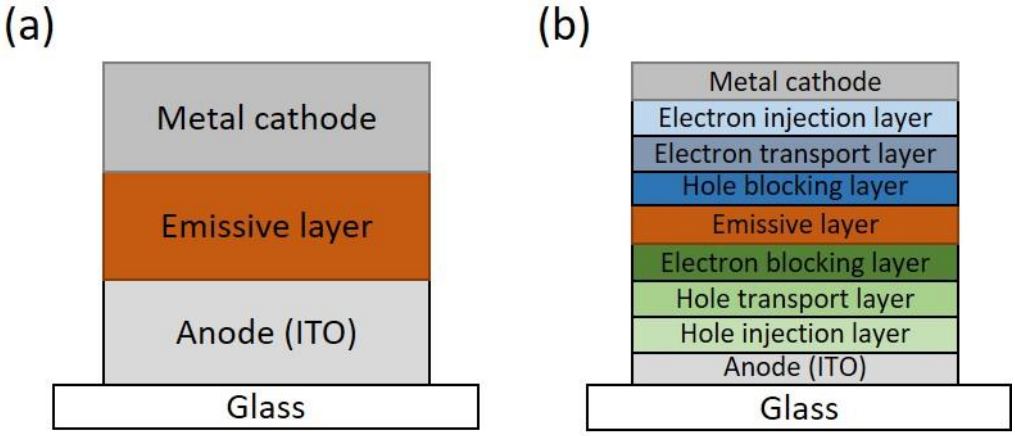

Figure 2.11. Typical device designs for OLEDs. (a) Single layer OLED. (b) Multilayer OLED.

To enable the extraction of light, one of the electrodes must be transparent. ITO is commonly employed as anode for hole injection, providing transparency in the optical regime, enabling the outcoupling of photons, and simultaneously serving as an electrical conductor.[71] However, the drawback of this simple design lies in the low efficiency achieved with these basic PLEDs, prompting the development of more sophisticated multilayer OLEDs, as mentioned earlier.

The inefficiency of the device can not only be attributed to the emitter. The device structure is also responsible for the low efficiency of PLEDs. In the majority of organic semiconductors used as emitters in OLEDs, the hole and electron mobility differ by orders of magnitude.[22] Additionally, there is a higher occurrence of trap states for electrons than for holes.[72] If an electron is caught in such a trap state, it cannot contribute to charge transport and might diminish the recombination.[73] The differences in mobility between holes and electrons as well as trapping of charge carriers lead to a shift of the recombination zone towards the metallic cathode.[74] The recombination zone is the region in the device where the majority of excitons decay to emit light. As illustrated in Figure 2.12, when the emissive layer is thin and/or the recombination profile is close to the cathode, a substantial amount of light is lost due to surface plasmons generated at the metal-semiconductor interface.

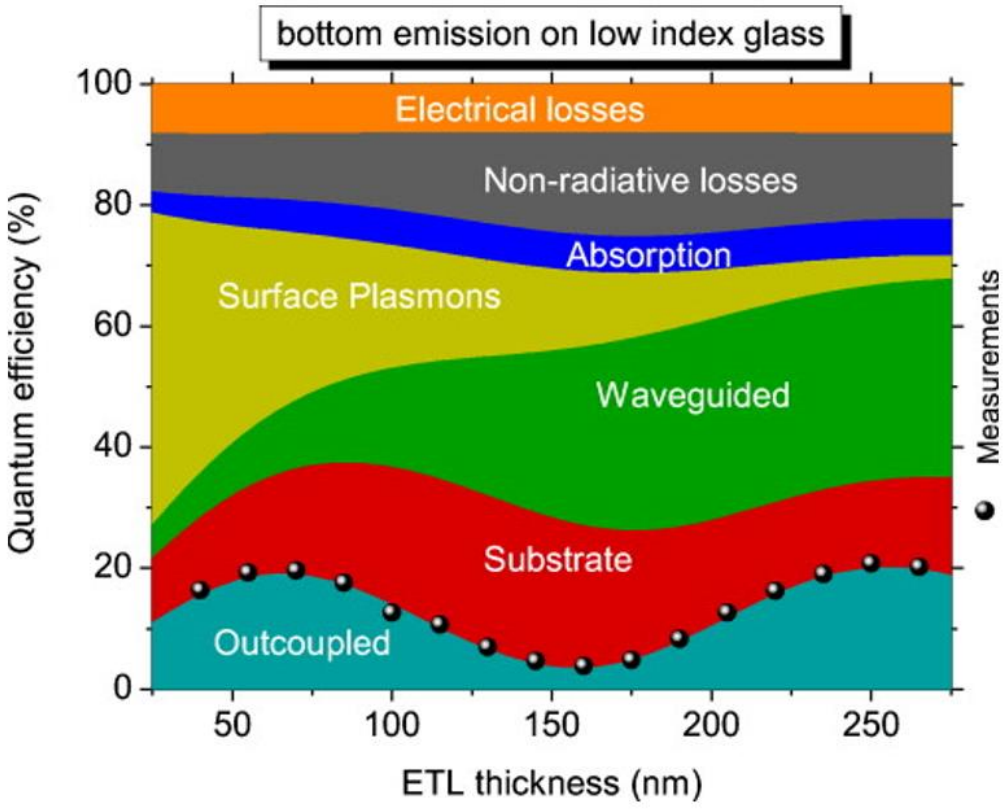

Figure 2.12. Out coupled light and loss processes for an OLED with respect to theire relative portion and the thickness dependence on each loss process. Figure adopted from [75].

To minimize losses resulting from the generation of surface plasmons, the control over the position of the recombination zone is critical. This necessity underscores one of the main motivations behind the development of multilayer structures. These structures comprise multiple layers of organic semiconductors, with each layer and material serving a specific purpose. As a result, the materials can be meticulously designed to efficiently fulfill their designated tasks. A schematic representation of such a multilayer structure OLED can be observed in Figure 2.11(b). The hole and electron injection layers (HIL and EIL) in these multilayer structures aim to facilitate efficient (ohmic) charge injection of their respective carriers. The task of the hole and electron blocking layers (HBL and EBL) is the prevention of charges and excitons from leaving the emissive layer, thereby maximizing recombination within the active layer. Multilayer OLEDs also incorporate hole and electron transport layers (HTL and ETL) to facilitate the efficient transport of charge carriers inside the device and place the recombination zone at the optically ideal position inside the microcavity.[76] Consequently, the HOMO and LUMO levels of all materials in this multilayer stack need to be aligned with each other.[77] Any variations in a single material can significantly impact the performance of the OLED. While multilayer stacks offer high efficiency, they are not without drawbacks. Utilizing various materials in such devices, each needing synthesis or purchase, emerge in significant expenses. Additionally, quick changes on such a stack are challenging, as a modification to one material can have implications for other layers. The numerous interfaces between layers make theoretical simulation of device operation very difficult, resulting in a limited understanding of how such a device operates.

To simplify the device, recent advancements have led to the development of single-layer OLEDs with high efficiency. However, meeting specific requirements for the emitter is crucial for the successful operation of such an OLED. Achieving a balance in charge transport is essential to prevent recombination near the electrodes. This balance entails ensuring equal mobility for both holes and electrons. Additionally, efficient single layer OLEDs require trap-free charge transport. Traps, potentially originating from impurities like water clusters and oxygen within the emissive layer, can impede charge transport.[72] Despite working under inert conditions inside a nitrogen filled glovebox during device fabrication and measurements, trace amounts of water and oxygen can still introduce trap states into the device. However, since the energy levels of trap states from water and oxygen are known, it is possible to define an energy window for the semiconductor IE and EA, for which these water and oxygen traps do not influence charge transport in an organic semiconductor. This window spans from -3.6 to -6 eV, indicating that organic semiconductors with both their IE and EA within these values can be considered trap free.[64] For instance, the TADF emitter 9,10-bis(4-(9*H*carbazol-9-yl)−2,6-dimethylphenyl)−9,10-diboraanthracene (CzDBA) with a HOMO at -5.93 eV and a LUMO at -3.45 eV positions the energy levels close to the borders of this trap-free window.[78] If CzDBA is sandwiched between two ohmic contacts, this can yield a single-layer OLED with an external quantum efficiency reaching up to 19 %.[60] The ongoing search for other materials, particularly for blue single-layer OLEDs, remains a current research focus.[79]

2.3.3. Device operations and electrical characteristics of OLEDs

To explain the device operations of OLEDs and how they convert electric power into light, it is most straightforward to consider a single-layer device, as depicted in Figure 2.13. Here, (a) represents the injection of charges into the HOMO or LUMO of the emissive organic semiconductor. These injected charges subsequently flow within the organic semiconductor toward the opposite electrode assisted by the applied electric field (b). The charges continue to flow until they recombine and form an exciton (c). This exciton then decays, resulting in light emission (d). In cases where charges do not form excitons, they can be extracted at the opposite electrode (e). An alternative loss process for injected charges is trapping, where the charges occupy states within the bandgap and no longer contribute to either charge transport or light output, as they may recombine nonradiatively (f).

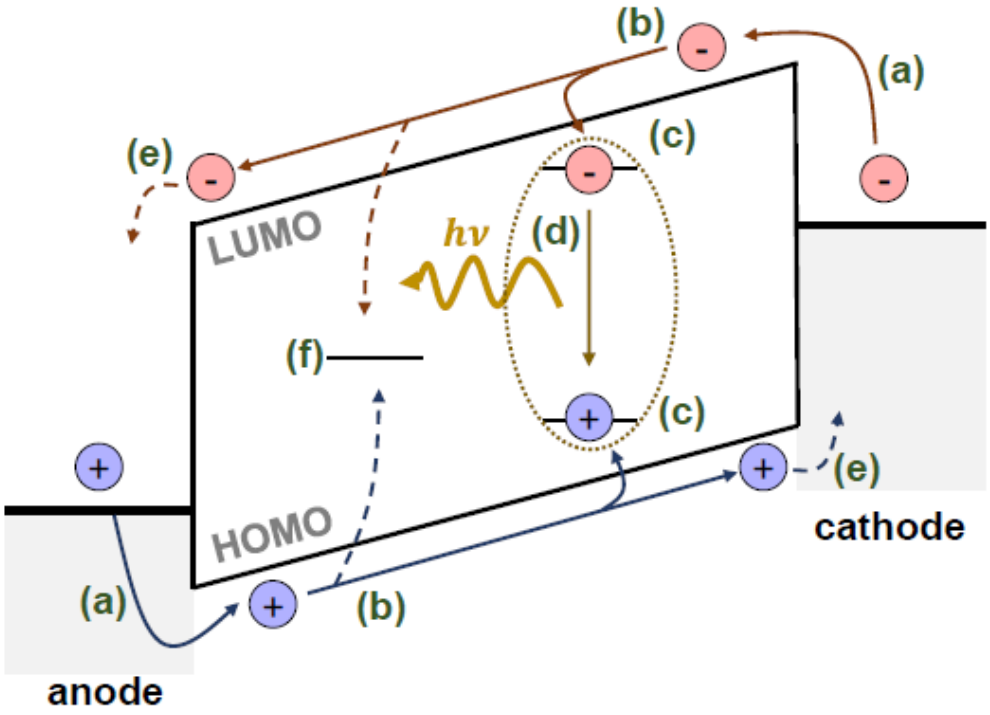

Figure 2.13. Device Operation in an OLED. (a) Charge injection. (b) Charge transport. (c) Exciton formation. (d) Recombination. (e) Charge carrier quenching at the electrodes. (f) Charge carrier traps. Figure adopted from [24].

Figure 2.14 illustrates a typical J-V curve of an OLED with either trap free electron or hole transport (or both). In such a curve, three distinct regimes can be identified.[19] The first regime, at low voltage, is known as the leakage regime. The leakage current is a parasitic current that arises from local short circuits in the device, for instance due to pinholes inside the active layer, allowing for current flow directly between the anode and the cathode, bypassing the organic semiconductor. The leakage current typically has a linear dependence on voltage and is temperature independent. Due to the difference in work function between the two electrodes, a certain voltage is required to overcome the resulting difference in chemical potential. This voltage, at which the chemical-potential disparity between the two electrodes is surpassed, is denoted as the built-in voltage V_{bi}. As long as the voltage is below V_{bi}, a built-in electric field exist, which opposes the direction of the injected current, as schematically shown in Figure 2.15(a).[80] This has the consequence that the current is not due drift, but arises from diffusion.

A positive diffusion current is present for any voltage above 0 V, but is typically overshadowed by the leakage current at low voltages. As the voltage is further increased and approaches V_{bi}, the diffusion current rises above the leakage current. In the *J-V* characteristics, this can be identified as a second regime, referred to as the diffusion regime. The current in this regime increases exponentially with voltage, as depicted in Figure 2.14.[81] In this regime, the current density *J* can be empirically described by the Shockley diode equation for PN-junctions:

$$J = J_0 \left[\exp\left(\frac{eV}{\eta k_B T}\right) - 1 \right]. \tag{6}$$

Here, J_0 represents the saturation current, and η is an ideality factor. At the exact point, where $V_{bi} = V$, flat band conditions apply, signifying that there is no internal electric field inside the device, as illustrated in Figure 2.15(b). With a further increase in voltage, the device enters the third regime, known as the drift-dominated regime. In this regime, the electric field points in the same direction as the injected current. To describe the current density *J* in such a double-carrier device, the Mott-Gurney law (4) needs to be modified to account for the involvement of two different charge-carrier species in charge transport.[82]

In such a double carrier device, two extreme cases can be considered. In the first case, it is assumed that the probability of bimolecular recombination *B* of holes and electron is low. Then, the current density *J* can be described by the plasma limit, which follows the equation:[83]

$$J = \sqrt{\frac{9\pi}{8}} \cdot \epsilon \cdot \sqrt{\frac{2q\mu_h\mu_e(\mu_h+\mu_e)}{\varepsilon B}} \cdot \frac{V^2}{L^3}. \tag{7}$$

Here, μ_h is the hole mobility and μ_e is the electron mobility and *L* is the thickness of the emissive layer. By contrast, when the probability of recombination approaches unity, the mobility in the Mott-Gurney law (4) can be considered as the sum of the electron and hole mobility:[84]

$$J = \frac{9}{8}\varepsilon(\mu_h + \mu_e)\frac{V^2}{L^3}. \tag{8}$$

In both cases, the equations imply that the current depends quadratically on the voltage. In case of ohmic contacts, the drift current is a space-charge-limited current. However, as opposed to a single-carrier device, for a recombination probability smaller than unity the current does not only depend on the mobility, but also on the recombination strength.

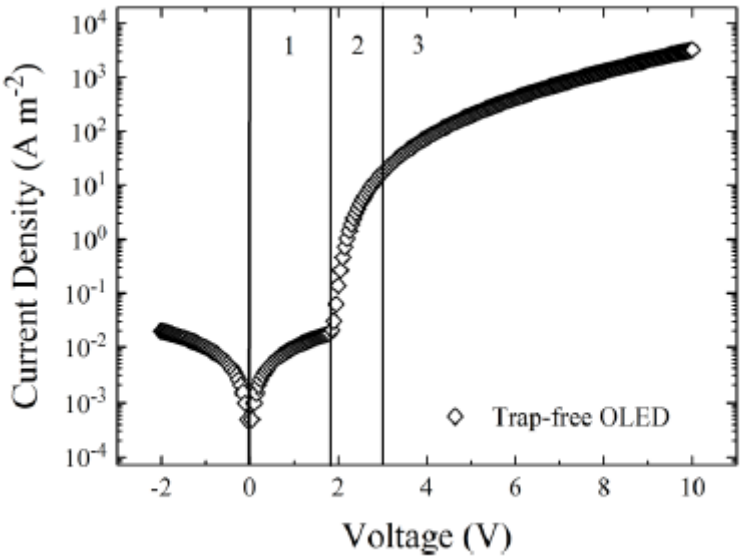

Figure 2.14. Typical *J-V* curve of a trap-free OLED. Figure adopted from [17].

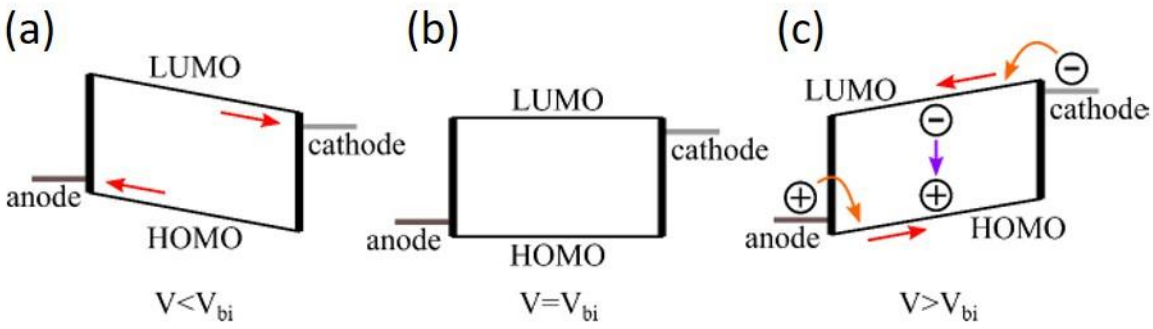

Figure 2.15. Schematic description of the charge-carrier flow dependent on the applied voltage. Figure edited from [17].

2.3.4. Recombination processes in OLEDs

As described in the previous section, the recombination of charge carriers is the process that generates light. In this section, an overview of the processes occurring during recombination will be provided. There are two types of recombination that can occur in OLEDs. One of them is bimolecular recombination, an emissive process where a free hole and a free electron recombine.[83] As a result of the small mean-free path in organic semiconductors – with a hopping distance of typically 1-2 nm – being smaller than the critical radius for Coulomb attraction, bimolecular recombination is a diffusion-limited process of the Langevin type. As a result of this Langevin recombination, an exciton is formed on the organic semiconductor, which can decay radiatively. The fraction of radiative decay, leading to the emission of a photon, depends on the photoluminescence quantum yield (Φ_{PL}) of the emitter. The so produced light can then be outcoupled from the device.

Another type of recombination is trap-assisted recombination, of which the rate is described by the Shockley-Read-Hall (SRH) formalism.[85, 86] This type of recombination is often non-emissive and therefore is a loss process. Trap-assisted recombination is the recombination of a trapped charge carrier with a free carrier of the opposite sign.[81] This underscores the importance of minimizing the number of traps in the design of the device and the emitter to achieve an efficient device.

2.3.5. Efficiency of OLEDs

One metric to assess the performance of an OLED is the determination of the external quantum efficiency (EQE). The EQE represents the percentage of injected charges that can be extracted as light from the device.

$$\mathrm{EQE}\ [\%] = \frac{\text{Extracted photons}}{\text{Injected charges}} \cdot 100 = \gamma \cdot \eta_{\frac{S}{T}} \cdot \Phi_{PL} \cdot \eta_{out}. \tag{9}$$

The EQE depends on several factors:[87] γ is the charge balance factor, $\eta_{S/T}$ is the spin factor, Φ_{PL} is the photoluminescence quantum yield and η_{out} is the outcoupling efficiency. In the following paragraphs, each of these factors will be explained in detail.

The charge balance factor γ includes various factors in the recombination process of an OLED. In an ideal scenario for an OLED with balanced charge transport and the absence of traps, γ

approaches unity, signifying that all the injected charges undergo radiative recombination via Langevin recombination. However, γ can be diminished by non-radiative processes such as SRH-recombination, triplet-polaron quenching (TPQ) and in case of TADF OLEDs by triplet-triplet annihilation (TTA).[88] To increase γ for emitters with imbalanced charge transport the injected charges need to be kept within the emissive layer. This is realized by the introduction of EBL and HBL layers. These layers confine the charges within the emissive layer, thereby enhancing their likelihood of recombination. Additionally, the application of a non-ohmic contact for the charge carrier species with the higher mobility can aid achieving balanced electron and hole currents. As an illustration, in conjugated polymers used in PLEDs, which contain electron traps, γ experiences a reduction to 0.8.[87]

The spin factor $\eta_{S/T}$ involves considering the spin of the generated excitons. As explained in Subsection 2.1.3, for fluorescent emitters, this factor is constrained to 0.25 by quantum mechanics. To enhance this factor, the use of phosphorescent emitters or TADF-materials is essential. For these materials ideally $\eta_{S/T} = 1$ applies. In addition to $\eta_{S/T}$, the Φ_{PL} is another material property influencing the EQE of OLEDs. The Φ_{PL} quantifies, for each emitting material, how many of the generated excited states will undergo radiative decay. A high intrinsic Φ_{PL} of an emitter is crucial for maximizing the EQE of a device.[89]

All the discussed parameters - γ, $\eta_{S/T}$ and Φ_{PL} - contribute to the probability of the injected charges being converted into a photon, a measure referred to as the internal quantum efficiency (IQE). While direct measurement of IQE is impossible, simulation approaches have been developed, approaching to calculate the radiative modes and subtract the loss processes such as non-radiative decays or surface plasmons using Dyadic Green functions.[27, 76] Recent findings indicate that OLEDs with an IQE approaching 100 % are achievable, highlighting that the primary challenge for such devices lies in efficiently extracting the photons from the device.[90]

The outcoupling efficiency η_{out} quantifies how many of the photons produced can be extracted from the device. As illustrated in Figure 2.12, various processes impede the exit of generated photons from the device. As discussed earlier, the creation of surface plasmons at the interface between the metallic cathode and the organic semiconductor contributes to these losses. Another significant factor is waveguided losses, arising from differences in the refractive index (n) among the emitter, substrate, and air.[76] Organic emitters typically have a refractive index around $n = 1.7$, while glass ($n = 1.5$) and air ($n = 1$) have lower refractive indices. Consequently, refraction and total internal reflection can occur at these interfaces, leading to the trapping of light within the device rather than allowing it to escape.

The reabsorption of photons by emitter molecules within the device is another contributing factor to the loss of generated photons. This process is influenced by the absorption cross-section of the emitter.[91] To mitigate this reabsorption, a strategy is to blend the emitter with another material, effectively diluting the emitter.[92] Ongoing research is focused on further enhancing outcoupling efficiency.[93]

2.4. Working principles of OSCs

Organic solar cells (OSCs) operate by converting light into electrical power, providing an inverted functionality compared to OLEDs. Unlike their inorganic counterparts, such as silicon-based solar cells, OSCs utilize organic compounds. This offers advantages in terms of renewability, production, and application, including flexibility for applications like flexible solar cells. In this section, the working principles of OSCs and the ongoing challenges aimed at enhancing their efficiency will be delved into.

2.4.1. Historic development of OSCs

The beginning of development of OSCs dates back to 1958 when Calvin et al. introduced the first models utilizing phthalocyanines.[94] However, these initial organic solar cells only demonstrated photocurrents on the order of microamperes. A significant breakthrough occurred in 1986 when Tang developed the first donor-acceptor systems.[95] Subsequent enhancements were achieved by blending the donor and acceptor materials, as demonstrated by Yu et al.[96] During this period, the focus on the donor material led to the standardization of the acceptor component, commonly using fullerene C_{60} or its derivatives. A notable advancement came in 2016 with the introduction of non-fullerene acceptors, contributing to a substantial increase in the efficiency of organic solar cells to 17 %.[38]

2.4.2. Device design and device operations of OSCs

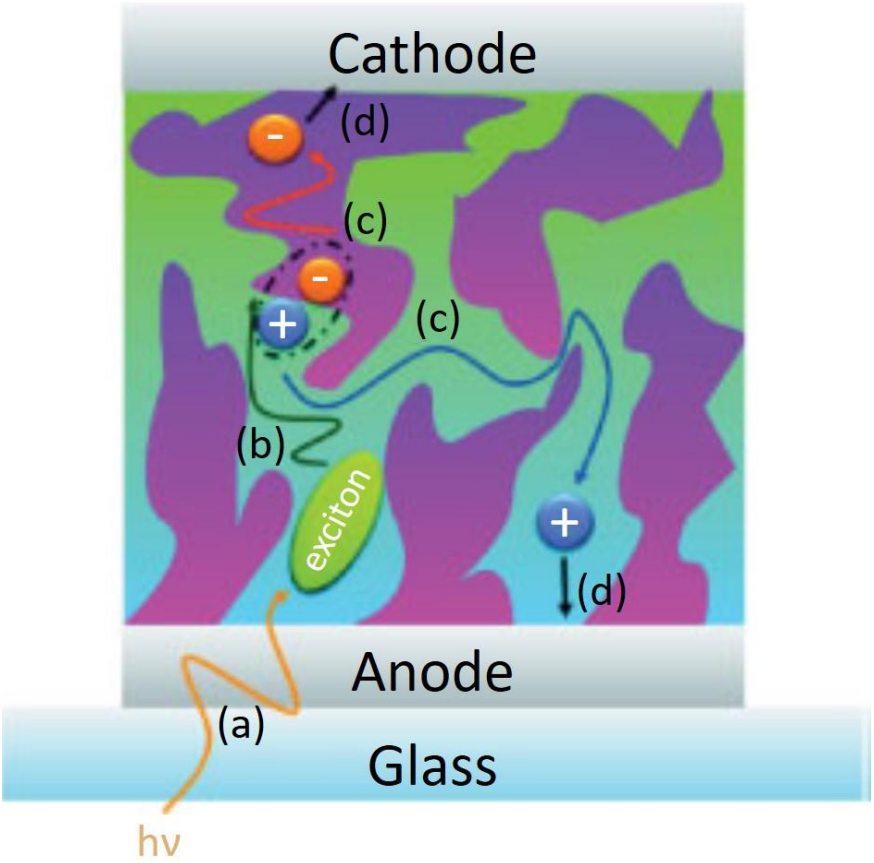

Figure 2.16. Sketch of a BHJ OSC. (a) Exciton formation via light absorption. (b) Exciton diffusion to the interface. (c) Charge separation at the interface. (d) Charge carrier transport the extraction electrodes. Figure adopted from [97].

In Figure 2.16, a schematic representation of a bulk heterojunction (BHJ) organic solar cell (OSC) structure is depicted. Such an OSC comprises a transparent anode, typically ITO, which is sputtered on glass, and a metallic cathode. The transparent anode is necessary for incoming photons to reach the active layer, which is sandwiched between the two electrodes. This active layer is a blend of two organic semiconductors, with one serving as the electron donor and the other as the acceptor. The donor is characterized as an electron-donating material, while the acceptor acts as an electron-accepting material.[98] To achieve such an arrangement, the HOMO and LUMO energy levels of the donor must be higher than those of the acceptor, as illustrated in Figure 2.17. Consequently, the donor facilitates hole transport towards the anode, while the acceptor is responsible for electron transport towards the cathode. Ensuring controlled phase separation within the blend is crucial for optimal charge transport.[99] If the donor and acceptor are perfectly distributed, meaning they are randomly dispersed, charge transport pathways are impeded. Conversely, if significant phase separation occurs, reducing the interface area between the donor and acceptor, fewer excitons can reach the interface, reducing the overall performance of the OSC.

In the operation of an OSC, light penetrates the blend through the transparent anode ((a) in Figure 2.16). The incident light is typically absorbed by the donor, leading to the formation of an exciton. The absorption process is depicted schematically in Figure 2.17 in the donor. Following its formation, the exciton has a limited diffusion length in organic semiconductors, typically within a range of 10 nm, before it undergoes decay.[100] For the exciton to separate into free charges, it requires the aid of the energetic offset between the donor and acceptor, since the exciton-binding energy in organic semiconductors is strong, due to the low dielectric constant. Therefore, the formed exciton must first diffuse towards the donor-acceptor interface ((b) in Figure 2.16). The limited diffusion lengths underscore the critical importance of controlling the phase separation between the donor and acceptor.

When an exciton formed in the donor material reaches the interface between the donor and acceptor ((c) in Figure 2.16), the electron is transferred to the LUMO of the acceptor, forming a charge-transfer state, as illustrated in Figure 2.17. This bound state may dissociate into free charge carriers, which are transported to the cathode for electrons or the anode for holes,

respectively ((d) in Figure 2.16). These charges can then be extracted at the electrodes, allowing the energy from the photon that created the exciton to be harvested.

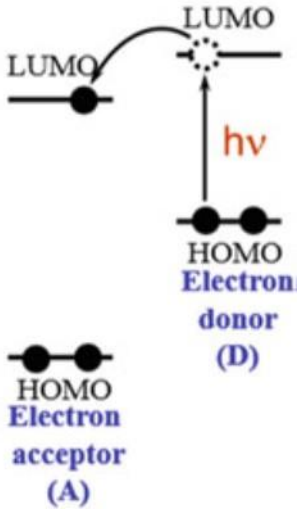

Figure 2.17. Sketch of electronic processes in an OSC comprising a donor and acceptor blend. Figure adopted from [99].

2.4.3. Electrical characterization of OSCs

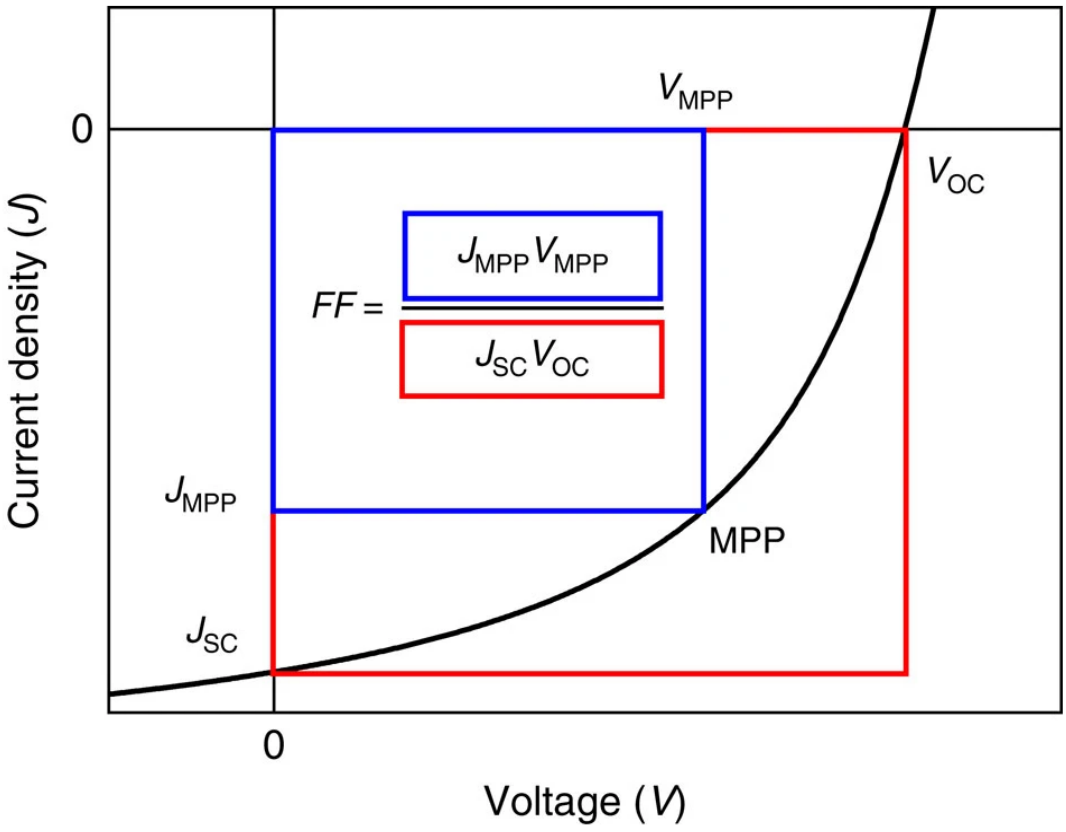

Figure 2.18. Typical J-V diagram of an OSC under illumination. Figure adopted from [101].

In Figure 2.18, a typical J-V diagram for an OSC under illumination can be seen. In the fourth quadrant, the current is negative (implying extraction) while the voltage is positive. The product of the current and the voltage defines the power, a negative value implying that it is output from the device. To determine the performance of such an OSC, it is useful to define two characteristic parameters, which are the short-circuit current density J_{SC} and the open circuit voltage V_{OC}. The short circuit current is the current that flows when no voltage is applied to the device. On the other hand, V_{OC} is the voltage that needs to be applied for the current to reach zero. The maximum power point (MPP) is reached, when the product of $J \cdot V$ reaches its minimum (largest negative value). The corresponding values for current und voltage are denoted as J_{MPP} and V_{MPP} respectively. The ratio of J_{MPP} times V_{MPP} and J_{SC} times V_{OC} is called the fill factor *FF*.

$$FF = \frac{J_{\mathrm{MPP}} \cdot V_{\mathrm{MPP}}}{J_{\mathrm{SC}} \cdot V_{\mathrm{OC}}}. \tag{10}$$

The fill factor is a measure for how close J_{MPP} and V_{MPP} are to their theoretical maximum values, J_{sc} and V_{oc}. Therefore, the larger the fill factor, the higher the efficiency of the OSC. The power-conversion efficiency η is defined by the output power divided by the input power, and can also be expressed in terms of J_{sc}, V_{oc}, and *FF*.

$$\eta = \frac{P_{MPP}}{P_{\mathrm{in}}} = \frac{FF \cdot J_{\mathrm{SC}} \cdot V_{\mathrm{OC}}}{P_{\mathrm{in}}}. \tag{11}$$

P_{in} is the power of the light that shines on the device. For testing purposes, this is usually set to $1000\ \frac{W}{m^2}$ as it corresponds to the solar energy reaching the earth at an angle of 48.2°. This implies that solar energy has to travel 1.5 times through the Earth's atmosphere compared to a perpendicular approach, with all the energy loss processes involved during this travel. This condition is also known as the AM1.5 spectrum.[102]

2.4.4. The influence of the dielectric constant on OSCs

In contrast to inorganic semiconductors, two materials are necessary to separate the charges from the generated excitons.[103] The design is driven by the low dielectric constant of organic semiconductors. According to Coulombs law,

$$F = \frac{1}{4\pi\varepsilon_r\varepsilon_0} \cdot \frac{q_1 q_2}{r^2} \tag{12}$$

the force *F* between two charges depends on the elementary charges of the electron and the hole (q_1 and q_2), the distance between these two charges r and the relative permittivity ε_r of the materials used. Typical organic materials have a relative permittivity of $\varepsilon_r \approx 3$, while silicon for example has a relative permittivity of $\varepsilon_r \approx 12$.[99] As ε_r is in Equation 12 in the denominator, a lower ε_r increases the coulombic force between the charges.

In Figure 2.19, an example is shown illustrating the consequences of the difference in dielectric constant between organic and inorganic materials. If the dielectric constant in known for a material, the exciton diameter can be determined using the following equation:

$$a_0 = \frac{\hbar^2 \varepsilon_0 \varepsilon_r}{e^2}\left(\frac{1}{m_e^*} + \frac{1}{m_h^*}\right). \quad (13)$$

Here, a_0 is the exciton diameter, $\hbar$ the reduced Planck constant, e the elementary charge, m_e^* the effective electron mass and m_h^* the effective hole mass. In this example, the high dielectric constant of silicon leads to an exciton diameter of 9 nm. Due to this distance between the hole and electron, the photogenerated exciton can immediately separate into free charges, generating a photocurrent.[104] On the other hand, the example for C_{60} with a low dielectric constant of $\varepsilon_r = 4.4$ (still high for organic materials[105]) results in an exciton with only a 0.5 nm diameter. Here, the probability of dissociation of the exciton into free charges is very low due to the high Coulombic force resulting from Equation 12. Therefore, the photocurrent of a single material organic solar cell is very small. To improve this charge separation, the blend of the two materials, as discussed in the previous section, is necessary for an efficient OSC.

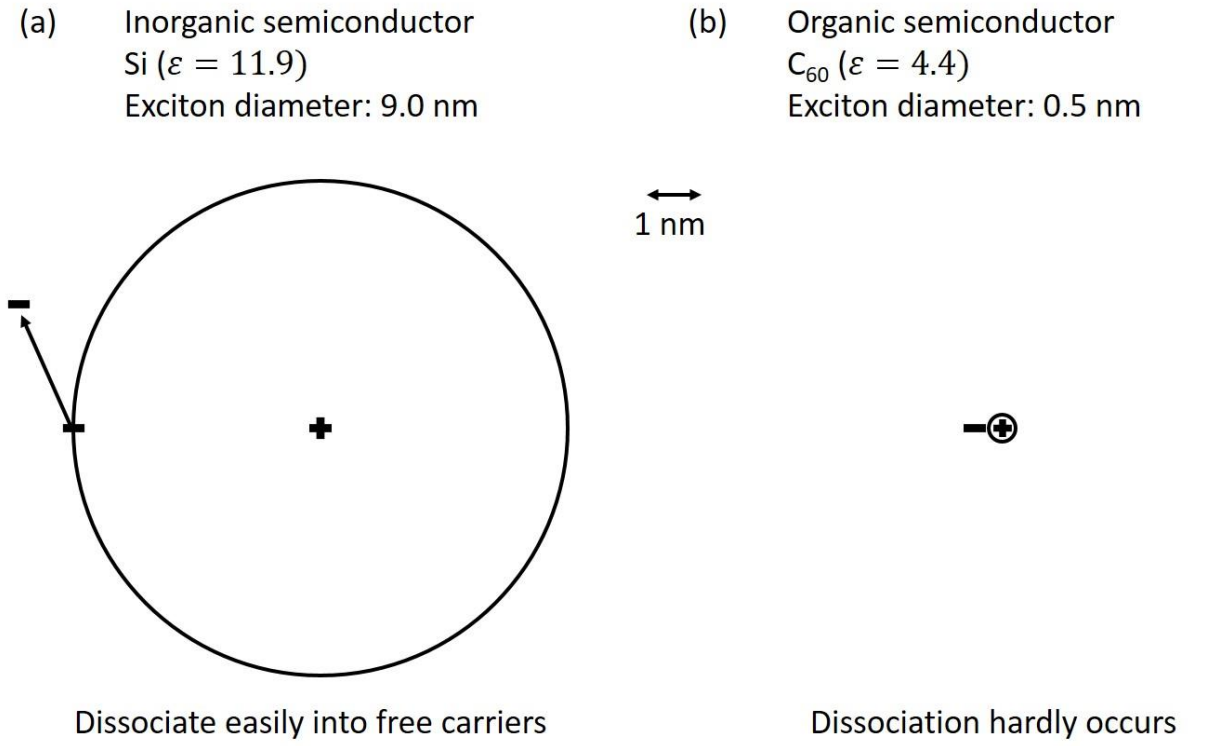

Figure 2.19. Graphic illustration of the different exciton diameters for (a) silicon and (b) C_{60} showing the influence of the dielectric constant for exciton decay into free charges. Figure recreated from [99].

2.5. Processing of organic semiconductors

In the preceding section, an elucidation was provided on how organic semiconducting devices function, emphasizing the importance of meticulously controlling various layers for the creation of efficient devices. Notably, precise thickness control is necessary for interlayers, and managing the degree of phase separation is crucial in the case of organic solar cells (OSCs). This section will offer an overview of the two primary deposition techniques for organic semiconductors - evaporation and solution processing. Furthermore, the physical background of polymer mixing will be introduced.

2.5.1. Evaporation of organic semiconductors

One method for depositing small-molecule organic semiconductors involves thermal evaporation. In this process, the organic molecules are sublimed in a vacuum. Typically performed under high vacuum conditions (e.g., $2 \cdot 10^{-6}\,\mathrm{mbar}$ with our equipment) the organic molecules are heated until they transition into a gaseous state and then are deposited on a substrate to form a film.[70] In Figure 2.20, a schematic of such an apparatus is displayed. The grey area represents the chamber, enclosing all the systems utilized in this process. Connected to this chamber are the vacuum pumps (not shown). Within the chamber, the organic material slated for sublimation is placed in a ceramic crucible. Once vacuum is applied, the material is heated until it vaporizes (sublimes). The rate of sublimation is typically monitored by piezo balances. The vaporized material then will deposit and form a film on the surface of a substrate, located in a substrate holder usually placed above the crucible. Since multiple samples are often fabricated simultaneously, the substrate holder typically rotates to ensure uniform thickness across all samples, regardless of their location in the holder.[106]

Such a system offers precise control over film thickness, as the evaporation process can be slow, typically in the range of 0.01 nm/s. The slow evaporation allows the material to find the energetically favorable positions during deposition, promoting good crystallization of the materials. Another advantage is the ease of stacking layers from different materials, making this method highly applicable in the fabrication of multilayer OLEDs. Indeed, controlling the evaporation rate is crucial for achieving good film formation, particularly at interfaces where charges transfer between different materials. A slow and precise evaporation rate, especially during the initial nanometers of film deposition, is essential to ensure the formation of a well-defined interface and, consequently, an efficient performance of the device.[107]

As all methods, the evaporation method has its drawbacks. It is not applicable for polymers, as they cannot undergo sublimation. Additionally, the slow deposition rate, with a typical rule of thumb being 1 nm/min, makes the fabrication process time-consuming. Furthermore, considerable energy is required to operate vacuum pumps in order to achieve the necessary vacuum conditions. It must be noted, that the material efficiency, referring to the proportion of the organic semiconductor utilized on the substrate at the end of the process, is very low for the evaporation method.[108] Due to the complexity and associated costs the evaporation process presents challenges. For instance, commercially available OLEDs are primarily utilized in high-end electronic devices such as smartphones or television screens, where the benefits of OLED technology justify the higher price points.[109]

In conclusion, while the evaporation method offer precise and easily controllable films suitable for applications like multilayer OLEDs, its drawbacks lies in the slow deposition rate and the low material efficiency. Consequently, while evaporation remains suitable for academic research and high-end industrial applications, its impracticalities hinder the widespread use of organic semiconductors in more cost-sensitive applications like ceiling lamps.

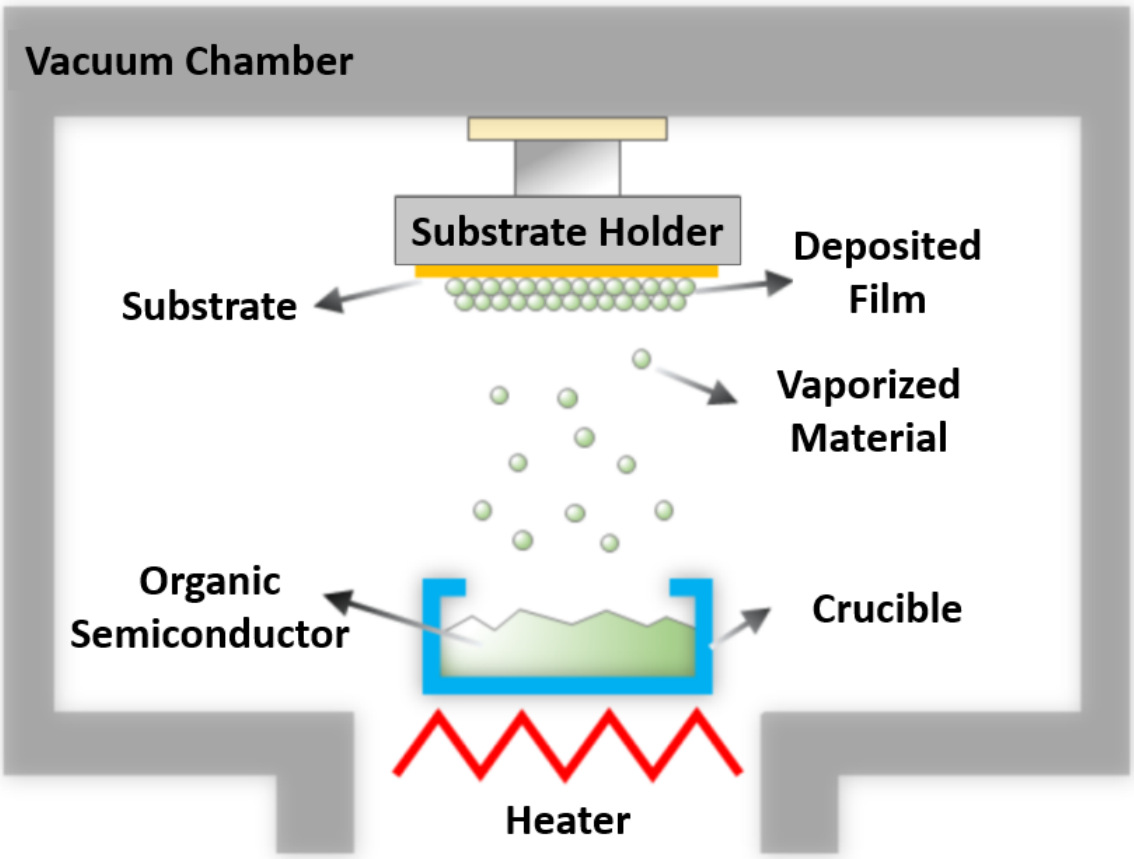

Figure 2.20. Sketch of the equipment for thermic evaporation of small molecule semiconductors on to substrates for film deposition purposes. Figure edited from [110].

2.5.2. Solution processing of organic semiconductors

An alternative to evaporating organic semiconductors is to process them using a solution-based method. In this process, the materials are dissolved in a solvent and applied to a substrate. The solvent evaporates, leaving behind the organic semiconducting film. Various methods exist for solution processing, ranging from simple drop casting to advanced techniques like printing or meniscus-guided coating, as illustrated in Figure 2.21.

The most straightforward method of solution processing a film is drop casting. In this process, the solution containing the organic semiconductor is dropped onto a substrate. Once the solvent evaporates, the film is formed. While this method is extremely simple and requires no specialized equipment, the drawback is that the film thickness may not be uniform across the substrate.[111]

To achieve more precise control over the crystallization process, various meniscus-guided coating procedures have been developed. These techniques share the common feature of maintaining a constant meniscus of the solution across the entire substrate surface. This is typically achieved by moving the substrate under the equipment that creates the meniscus, as depicted in the red box in Figure 2.21. The advantage of such a method is the ability to process a uniform film over a large substrate area. By varying the substrate speed, the

crystallization process can be influenced, providing access to a variety of films with different properties.[112] The meniscus-guided coating technique is often employed in the fabrication of OFETs and for large-area industrial applications of organic semiconductors using roll-to-roll processing methods.[113]

Another group of solution processing methods includes printing methods, where the solution is deposited on the substrate in a controlled manner. Inkjet printing of organic semiconductors has received considerable attention, opening the door to large batch processing of organic materials, especially organic semiconductors. While such applications are intriguing, they are also complex. In inkjet printing, factors such as ink viscosity, surface tension, and nozzle diameter significantly influence the resulting film.[114] This underscores the challenges involved in developing a printing procedure. Nevertheless, the potential applications for such methods, especially in industry, are extensive.

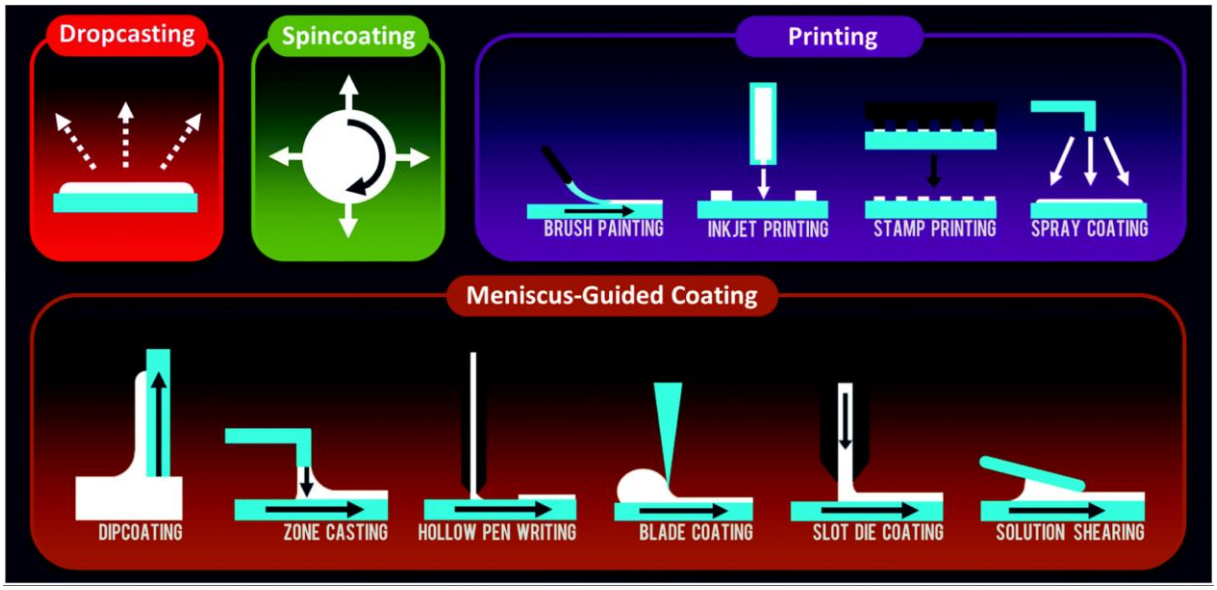

Figure 2.21. Overview over several methods for solution processing of organic materials. Figure adopted from [115].

For the solution processing of the films fabricated for the devices used in this thesis, the applied procedure is called spin coating. In Figure 2.21, the four steps involved in this process are shown. In the first step, the solution with the dissolved organic semiconductor is placed on top of the substrate (a). This substrate is placed on top of a spinning plate. After placing the solution, the substrate is spun at a certain speed (b). This spinning leads to the homogeneous spreading of the solution on top of the substrate (c). The thickness of the resulting solution layer depends on the spinning speed, the viscosity of the solution and the wetting properties of the substrate surface, but not on the amount of solution put on top of the substrate surface. As these parameters are easy to control, the film thickness is usually controlled by variation of the spinning speed, where faster spinning leads to a thinner film. After spinning, the solvent evaporates (d), and the dissolved semiconductor precipitates, forming a film uniform over the substrate.[116]

The spin-coating method offers the advantage of facile and reproducible production of uniform films. The film thickness in spin coating is solely influenced by the material properties

of the used solvent (vapor pressure, surface tension and viscosity), the concentration of the organic semiconductor in the solvent, the spinning speed, and the wetting properties of the substrate, all of which are easily controllable parameters. However, it is noteworthy that the scalability of this process is limited. In summary, spin coating stands out as a straightforward and effective technique for generating uniform films of organic semiconductors, particularly in a testing environment for solution-processed systems.

In contrast to the evaporation method, stacking multiple layers on top of each other in solution-processed devices poses big challenges. When attempting to solution process a layer onto another, there is a risk of solvent interaction with the underlying layer. This interaction may lead to potential damage to the layer or result in intermixing of the two layers, thereby impacting the interface crucial for the device's proper functioning. To safeguard the underlying layer, one approach is the use of the orthogonal solvent method.[117] Materials and solvents can generally be categorized as either hydrophilic or hydrophobic. For instance, when dealing with a hydrophobic underlying layer such as most polymers, it becomes feasible to employ hydrophilic solvents like alcohols for solution processing on top of such layers.[118]

In general, solution processing offers convenient and scalable manufacturing at a low cost. However, it comes with the disadvantage that a solvent is required, which can influence the film, particularly its crystallization—a critical factor for the proper functioning of organic semiconductors. Additionally, the stacking of layers for multilayer devices is not as straightforward as it is with thermal evaporation.

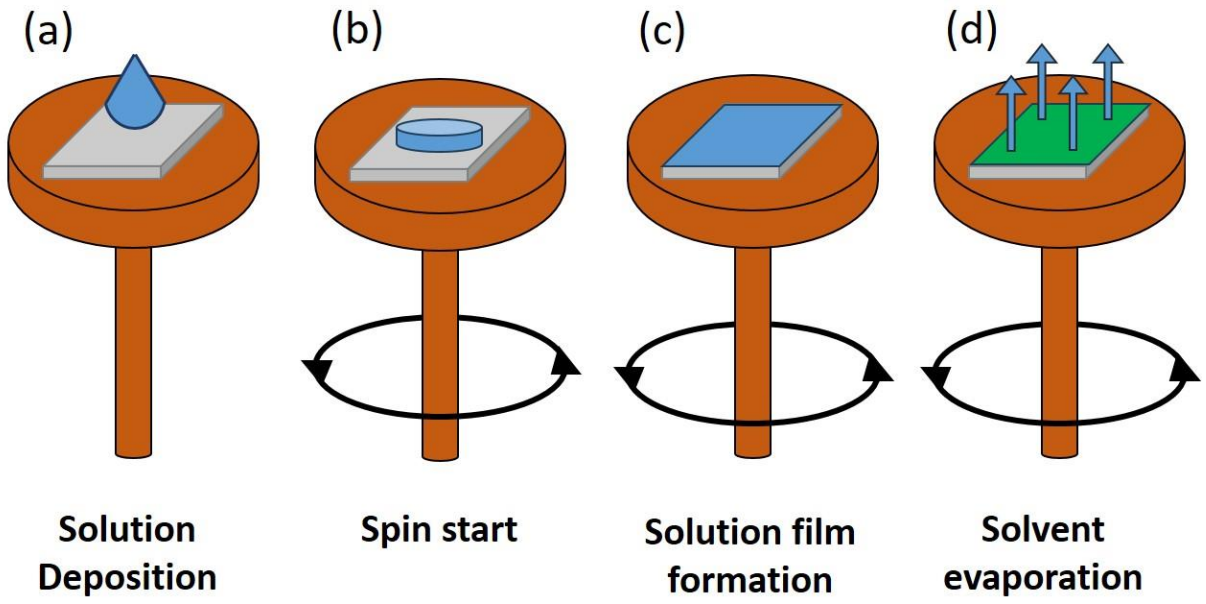

Figure 2.22. Schematic drawing of the steps during spin coating. In orange, the spincoater chuck is shown, grey represents the substrate, blue the solution and green the resulting film. Figure recreated from [119].

2.5.3. Polymer blends

For BHJ blends of materials, mixing is necessary. The same applies to OLEDs when two materials are blended, such as in the case of trap dilution.[120] Ideally, mixing is a favorable process as it increases the entropy of a mixture (ΔS_{mix}) compared to the individual materials

before mixing. Unfortunately, according to the Gibbs-Helmholtz equation, there is also an enthalpy of mixing (ΔH_{mix}) contributing to the Gibbs energy of mixing (ΔG_{mix}):

$$\Delta G_{mix} = \Delta H_{mix} - T\Delta S_{mix}. \quad (14)$$

To achieve mixing, ΔG_{mix} must be negative. This is mostly the case if ΔH_{mix} is negative. ΔH_{mix} can also be positive, resulting from interactions between molecules such as van der Waals interactions. In this case, whether two materials mix or phase separate depends on the temperature. For polymer solutions, the change in entropy is not as easy to determine as for small molecules. Paul Flory and Maurice Loyal Huggins developed the Flory-Huggins theory, a model which describes the mixing of polymers with a solvent in a 2D lattice.[121] In this lattice, each site can be occupied by either the solvent or one monomer of the polymer, representing the entropy of the system. They introduced an interaction parameter χ to describe the interaction between the polymer and the solvent. Consequently, the energy of mixing for polymers can be described as follows:[122]

$$\Delta G_{mix} = RT[n_1 ln\phi_1 + n_2 ln\phi_2 + \chi\phi_1\phi_2]. \quad (15)$$

Here, *n* is the mole and φ the volume fraction of each component.

As described, mixing is not always an easy process, particularly when polymers come into play. Phenomena like aggregation and phase separation must always be considered by dissolving a material or making a blend of two materials from a solution.

3. Objectives

Chapter 4 of this thesis is devoted to enhance the dielectric constant of organic semiconductors. As outlined in the preceding chapter, the low dielectric constant of organic semiconductors necessitates the blending of two materials for an efficient OSC. Theoretically, increasing the dielectric constant could obviate the need for a donor-acceptor system, simplifying the device structure of an OSC.[123] This enhancement is pursued by blending the active layer with materials exhibiting high dielectric constants. The goal is to elevate the overall dielectric constant of the film, ideally facilitating exciton splitting within the layer and enabling efficient single-layer OSCs. Materials utilized for increasing the dielectric constant include organic compounds with high dielectric constants, such as camphoric acid anhydride, as well as economically viable inorganic materials like TiO_2 nanoparticles [124].

In the subsequent Chapter 5, the focus shifts to enabling efficient charge injection into organic semiconductors. The investigation aims to determine if the interlayer strategy, developed by Kotadiya et al. for ohmic hole injection, could be adapted for electron injection.[59] The study centers on the electron-transport material PNDI(2OD)-2T, for which ohmic electron injection was unsuccessful with previously published strategies.[125] To facilitate the application of the interlayer strategy, the feasibility of solution-processed interlayers on top of the polymer is explored and compared with traditional evaporated interlayers. Solution processing could offer a convenient method for applying such interlayers.

In Chapter 6, the feasibility of solution processing of OLEDs based on TADF is investigated. While efficient OLEDs have traditionally been fabricated using thermal evaporation, this method has drawbacks, as discussed in Subsection 2.6.1.[90] Solution processing presents an accessible alternative for such systems. Building on the solution-deposition of multiple layers on top of each other as described in Chapter 5, the orthogonal-solvent method is used to fabricate highly efficient multilayer OLEDs. To enhance the stability of the underlying organic semiconductor films against the solvents utilized for subsequent layers, the emitters are incorporated in inexpensive polymers such as polystyrene, which allows for the fabrication of fully solution-processed TADF OLEDs with reduced materials costs.

4. Increasing the dielectric constant of organic semiconductor films

This chapter explores a strategy for enhancing the dielectric constant of organic semiconductors. The low dielectric constant of organic semiconductors poses a challenge for the development of efficient single-material OSC, as discussed in Section 2.4. The first section of this chapter (4.1) focuses on outlining the general approach to increase the dielectric constant. This is followed by sections (4.2 and 4.3) detailing the results obtained using different materials for enhancing the dielectric constant. Finally, after the summary of the results (4.4), the materials and procedures utilized in this project are elucidated in section 4.5.

4.1. Idea of this project

In this project, a concept was developed to increase the dielectric constant of the organic semiconductor film by dispersing a material with a high dielectric constant into the film. As illustrated in Figure 4.1, the green-highlighted material with a high dielectric constant was intended to be finely dispersed within the layer of the organic semiconductor (shown in blue). The aim was to achieve a higher dielectric constant of the film without affecting the charge carrier transport in the organic semiconductor. Since all charge transports are intended to occur within the organic semiconductor, the high dielectric constant material must not contribute to the charge transport. Therefore, the energy levels of these materials are not pertinent, and the material can also have the properties of an electrical insulator.

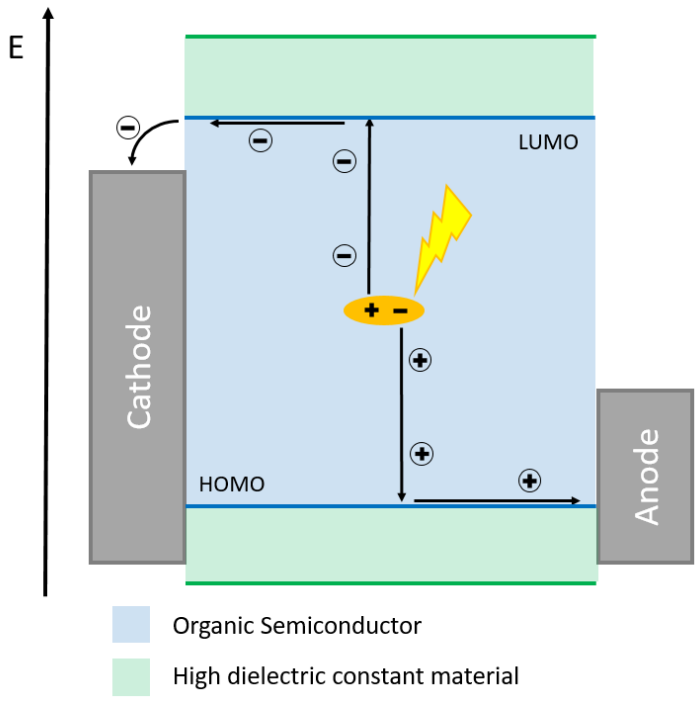

Figure 4.1. Schematic sketch and proposed working principle of a single semiconductor OSC. The active layer consists of a blend of an organic semiconductor (blue) and a material with a high dielectric constant (green) fine dispersed in the organic semiconductor. After absorption of a photon (yellow) an exciton (orange) is generated, which decays into free charge carriers traveling to their respective electrodes.

The advantage of fabricating a film comprising an organic semiconductor and a material that enhances the dielectric constant lies in the simplification of the operational principles of OSCs and the avoiding of the voltage loss due to donor-acceptor offset. With this approach, an OSC could function analogously to an inorganic solar cell, where both light absorption and charge separation occur within a single material.[123, 126] This is feasible due to the high dielectric constant of silicon, commonly used in inorganic solar cells. For a detailed understanding of the significance of the dielectric constant, refer to Section 2.4. In the proposed OSC configuration, akin to inorganic solar cells, charges would separate immediately after the absorbed light generating an exciton (depicted in orange in Figure 4.1). Subsequently, the resulting free charges would be driven to the electrodes by the applied electric field and then extracted.

In such a system, the role of the organic semiconductor encompasses light absorption, charge separation, and charge transport to the electrodes. Conversely, the high dielectric constant material is not involved in these processes. Ideally, it should not affect the charge carrier transport within the semiconductor at all. To ensure efficient charge transport in the organic semiconductor as well as a uniform dielectric constant in the film, it is necessary for the material with the high dielectric constant to be uniformly dispersed within the film and should not tend to phase separate.

To achieve this objective, several materials with high dielectric constants were tested for the project, described in this chapter. To maintain the system entirely organic, organic molecules with high dielectric constants were explored. One such example used in this study is camphoric acid anhydride (CAA), which has a reported dielectric constant of $\varepsilon = 24$.[124] The molecular structure of this material is depicted in Figure 4.2(a). In addition to small molecules, certain polymers are also known to exhibit high dielectric constants and were investigated in this study. Polyfluorinated alkyl polymers, such as the triblockcopolymer poly(1,1-diefluoroethylene-1,1,2-trifluoroethylene-1-chloro-1-fluoroethylene) (p(VDF-TRFE-CFE)), exemplify this behavior and possesses a dielectric constant of up to $\varepsilon = 50$.[127] While these polymers are typically utilized in organic ferroelectric applications where a high dielectric constant is essential, in this study, they are employed solely to augment the dielectric constant.[128] The molecular structure of p(VDF-TRFE-CFE) is illustrated in Figure 4.2(b).

In addition to organic compounds, numerous inorganic materials also possess high dielectric constants. In this study, titanium dioxide nanoparticles (TiO_2-NP) were employed for this purpose. As TiO_2-NPs are commonly used in everyday applications such as white wall paint, it is readily available and cost-effective [129]. However, nanoparticles from inorganic materials like TiO_2-NPs have a tendency to aggregate in solution, similar to polymers. As mentioned earlier, aggregation can lead to phase separation, which is undesirable. Also, due to the ionic character of TiO_2-NPs, they cannot be dispersed in organic solvents together with the organic semiconductor to be processed from solution. To address these issues, modifications to the TiO_2-NPs were evaluated. Coating the TiO_2-NPs with surfactants, such as dodecylphosphonic acid and hexylamine (as depicted in Figure 4.2(c,d) respectively), is intended to prevent aggregation of the TiO_2-NPs, make them dispersible in organic solvents and facilitate their compatibility with the organic semiconductor.

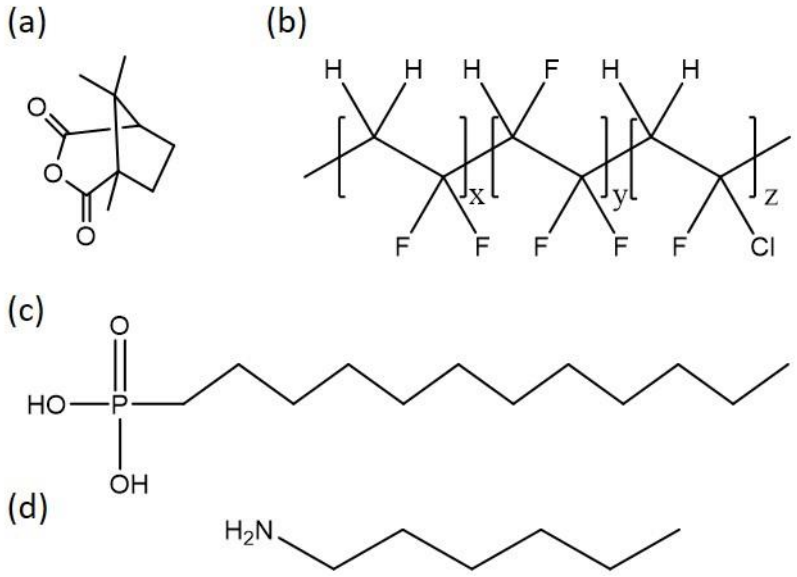

Figure 4.2. Molecular structure of the materials used to increase the dielectric constant. (a) Camphoric acid anhydride (CAA) and (b) P(VDF-TRFE-CFE). (c) and (d) show the molecular structure coated on TiO_2-Nanoparticles to achieve solubility in organic solvents. These are (c) Dodecylphosphonic acid and (d) Hexylamine.

In the subsequent chapters, the impact of blending these high dielectric materials into organic semiconductors will be investigated with a focus on the effects on charge transport and the dielectric constant of the semiconducting films.

4.2. Utilization of purely organic dopants to increase the dielectric constant

This section illustrates the incorporation of organic high dielectric constant materials into organic semiconducting films and examines how the resulting increase in dielectric constant influences charge transport. Initially, this is demonstrated with CAA, followed by investigations involving p(VDF-TRFE-CFE). The well-known organic semiconductor MEH-PPV is utilized for preliminary tests to establish the proof of principle, alongside the non-fullerene acceptor IT-4F, serving as a representative material commonly employed in OSCs.[19, 38]

4.2.1. Camphoric acid anhydride

In the initial phase of this project, MEH-PPV was blended with CAA to create a composite film incorporating both materials. Figure 4.3(a) demonstrates that doping the film resulted in an increase in the dielectric constant. Specifically, the dielectric constant rose from $\varepsilon = 3$ for pure MEH-PPV (red) to $\varepsilon = 6$ for a blend consisting of 50 % (w/w) of MEH-PPV and CAA (black). Figure 4.3(b) illustrates the impact of this blend on the charge transport properties. In this figure, the J-V curves for EO and HO devices are depicted for both pure MEH-PPV (EO in black, HO in red) and the MEH-PPV/CAA blend (EO in blue and HO in green). Here, the effect of the blend is clearly evident. The hole current appears to be approximately an order of magnitude lower for the blend compared to pure MEH-PPV. This reduction could result from the dilution of the semiconductor within the film, leading to fewer hopping sites available in the blend compared to the pure MEH-PPV film, thereby reducing the charge transport capability and

resulting in decreased current.[130] However, the situation worsens concerning electron current in the blend, as electron charge carriers are no longer able to effectively transport through the blended film, signaled by the absence of a measurable current in the EO-device of the MEH-PPV/CAA blend.

For double-carrier devices fabricated using the blend of MEH-PPV with CAA and pure MEH-PPV, the J-V characteristics are depicted in Figure 4.3(c). This figure illustrates that with increasing the amount of CAA the leakage current is increased, as it can be seen in the low voltage region. However, for the current density in the in the drift regime, for all devices values in the order of 10^3 A m^{-2} are achieved. This is in line with the hole currents discussed before, as they were not that severely affected by the addition of CAA as the electron currents. The differences in charge transport can be a result from phase separation within the film. As evident from Figure 4.3(d), this microscopy image shows white(ish) and red(ish) regions. The white(ish) regions can be attributed to CAA, while the red(ish) regions corresponds to MEH-PPV. Additionally, it can also not be ruled out, that the addition of CAA, with a LUMO of -0.7 eV may introduce trap states or affects the charge injection.[131]

The experiments presented in this section demonstrate the feasibility of increasing the dielectric constant of a film by blending it with a high dielectric constant material. However, the observed phase separation and the associated losses in charge transport makes CAA unsuitable for application in organic semiconducting devices.

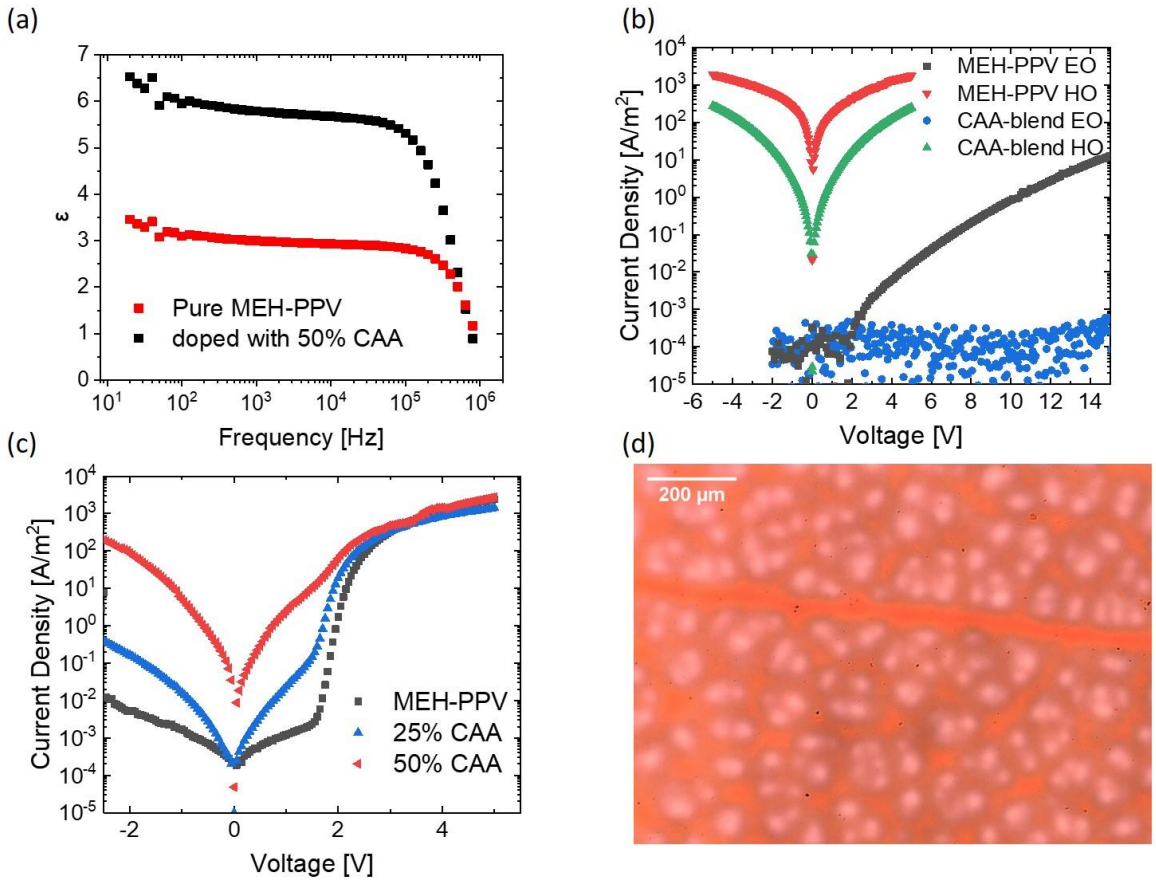

Figure 4.3. Electrical and optical characterization for devices consisting a blend of MEH-PPV with CAA. (a) Frequency depended dielectric constant for the pure MEH-PPV (red) as well as for blend with 50 % CAA (black). (b) J-V curves for single carrier devices (HO and EO) again for pure MEH-PPV (red and black) and for a blend with 50 % CAA (green and blue). Franziska Walz recorded the data for the EO of pure MEH-PPV. (c) Double carrier devices for pure MEH-PPV (black) and a blend with 25 % CAA (blue) and 50 % CAA (red). (d) Microscope picture of a MEH-PPV-CAA blend with 50 % CAA.

4.2.2. Polyfluorinated Polymers

As demonstrated in the previous subsection, the incorporation of the small molecule CAA to enhance the dielectric constant resulted in phase separation. This subsection aims to explore whether using a polymer to increase the dielectric constant yields better results. Therefore, p(VDF-TRFE-CFE) is employed, first blended with MEH-PPV and subsequently with the non-fullerene acceptor IT-4F.

MEH-PPV blended with p(VDF-TRFE-CFE)

Similar to the previously discussed blend, the inclusion of p(VDF-TRFE-CFE) into the film results in an increased dielectric constant. As depicted in Figure 4.4(a), the dielectric constant for pure p(VDF-TRFE-CFE) in this study is determined to be $\varepsilon = 26 \pm 1$ (green). Conversely, pure MEH-PPV exhibits a dielectric constant of $\varepsilon = 3$ (red). When combined in a 1:1 mixture (50 % (w/w) MEH-PPV and 50 % (w/w) p(VDF-TRFE-CFE)), the dielectric constant of the blend is determined to be $\varepsilon = 17 \pm 2$ (black). This value falls between the dielectric constants of the individual materials, supporting the concept that blending can effectively increase the dielectric constant of the film.

To assess the impact of incorporating p(VDF-TRFE-CFE), an insulator, onto an organic semiconducting film, a double carrier device using a blend of MEH-PPV with p(VDF-TRFE-CFE) was fabricated and compared to one using pure MEH-PPV to investigate the charge transport properties. The resulting J-V curves are shown in Figure 4.4(b). Both devices exhibit the typical shape of a double carrier curve, with three distinct regimes, as discussed in Chapter 2.3.3. There is only a slight shift to lower voltages for the built-in voltage (V_{bi}) in the blend (red) compared to pure MEH-PPV (black). The overall current density at 5V is one order of magnitude lower for the blend, attributed to the lower amount of semiconductor in the blend compared to pure MEH-PPV. Consequently, with fewer hopping sites in the film due to the lower amount of semiconductor, a naturally lower current is expected and observed.

The atomic force microscopy (AFM) images of the mixture provided in Figure 4.4(c) for the height and 4(d) for the phase reveal clear evidence of phase separation. This outcome is anticipated as the blend comprises two polymers. According to the Flory Huggins theory, polymer miscibility is typically low, and due to their chain-like structure, polymers tend to form ball-like arrangements.[132] These structures are evident in the AFM-height image, corroborated by the phase image, which depicts distinct phases for the different materials. Particularly at the interface between the two materials, significant changes in phase are observed.

Overall, these experiments demonstrate that blending an organic semiconductor with a high dielectric polymer like p(VDF-TRFE-CFE) can increase the dielectric constant while only minimally affecting the J-V characteristics. However, the use of two polymers within a blend promotes phase separation. To expand the scope of the investigation, in the next part of this section, MEH-PPV is replaced by a small molecule semiconductor in an attempt to minimize phase separation.

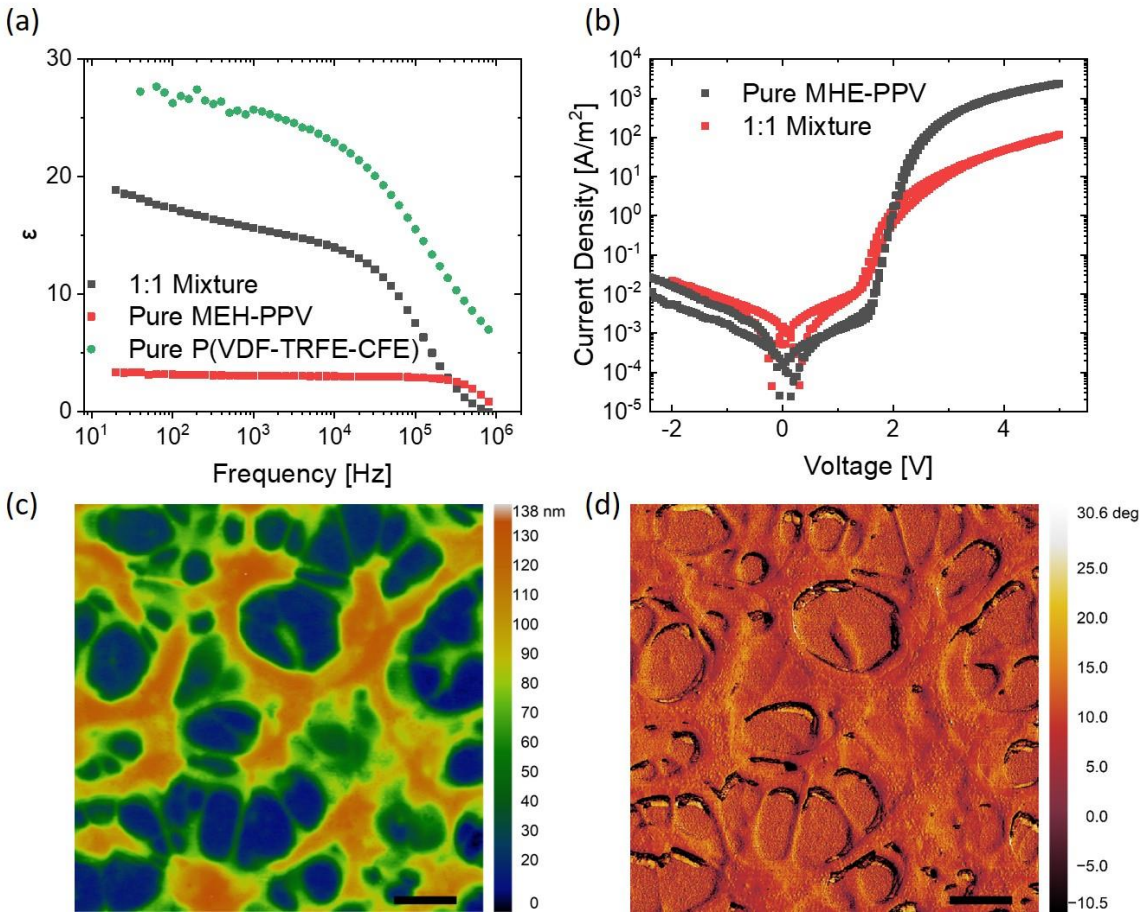

Figure 4.4. MEH-PPV blended with P(VDF-TRFE-CFE). (a) Dielectric constant versus frequency plots for pure MEH-PPV (red), pure P(VDF-TRFE-CFE) (green) and the 1:1 blend of both materials (black). (b) Double carrier J-V characteristics for pure MEH-PPV (black) and the 1:1 blend (red). (c) AFM height profile of a 1:1 blend of MEH-PPV with p(VDF-TRFE-CFE). The scalebar represents 2 µm. (d) The corresponding phase picture to the AFM height profile shown in (c) The scalebar represents 2 µm.

IT-4F blended with p(VDF-TRFE-CFE)

As blending polymers with polymers often leads to phase separation, in this section, the small molecule organic semiconductor IT-4F is employed to replace the polymeric organic semiconductor MEH-PPV. Typically, IT-4F is utilized in BHJ OSCs as a non-fullerene acceptor responsible for electron transport towards the cathode, in this study, it is utilized as a semiconductor while blended with p(VDF-TRFE-CFE).

As with the previous experiments in this chapter, the dielectric constant of the blend comprising 66 % (w/w) IT-4F and 33 % (w/w) p(VDF-TRFE-CFE) was examined. The dielectric constant for both the blend and pure IT-4F is depicted in Figure 4.5(a). For pure IT-4F, a dielectric constant of $\varepsilon = 3$ was determined, which is typical for organic materials.[133] However, for the blend of the two materials, two types of films were fabricated, distinguished by whether they underwent annealing after spincoating or not. Annealing is crucial for achieving a high dielectric constant in a film of pure p(VDF-TRFE-CFE), as the dielectric constant of p(VDF-TRFE-CFE) strongly depends on the film's morphology.[134] As illustrated in Figure 4.5(a), the addition of p(VDF-TRFE-CFE) to IT-4F increases the film's dielectric constant, with a more significant increase observed for annealed films. In the case of annealed films,

the dielectric constant reaches values up to $\varepsilon = 6.5$, compared to only $\varepsilon = 5$ for non-annealed films.

To assess the device performance of the blend, the J-V curves of double carrier devices were compared. Figure 4.5(b) illustrates these curves for devices made of the p(VDF-TRFE-CFE)/IT-4F blend, which was annealed (red) or not (black) and compares these to a device made of pure IT-4F (blue). Both films exhibited comparable thicknesses, with pure IT-4F at 190 nm and the blend at 220 nm. Upon comparison of the curves, they appeared similar in shape, but the current density of the blended film was lower. Additionally, a distinction between the annealed and non-annealed blended films was observed. Surprisingly, the annealed film, despite offering a higher dielectric constant, performed worse than the non-annealed film. However, irrespective of annealing, both blended films demonstrated a significant drop in current density compared to pure IT-4F. Unfortunately, this reduction cannot be solely attributed to the decrease in organic semiconductor in the blended film.

Once again, the disparity in charge transport can be attributed to the morphology of the film. To elucidate this, AFM images of both the annealed and non-annealed films have been taken as shown in Figure 4.5(c-f). Figures c and d depict the height profiles of the non-annealed and annealed films, respectively, while Figures e and f display the corresponding phase images (with e representing the non-annealed film and f the annealed film). Both height profiles reveal clear indications of phase separation, albeit less pronounced compared to the blend of MEH-PPV with p(VDF-TRFE-CFE) discussed in the preceding section. This reduced degree of phase separation is evident from the smaller grain sizes observed in the raised areas of the height images, as well as from the phase images. Such a lesser degree of phase separation is expected when a small molecule is mixed with a polymer, rather than blending two polymers together. This reduced phase separation also explains the lower dielectric constant observed in the blended film of IT-4F with p(VDF-TRFE-CFE) compared to the MEH-PPV/p(VDF-TRFE-CFE) blend, in addition to the smaller amount of p(VDF-TRFE-CFE) present in the IT-4F blends. The dielectric properties of p(VDF-TRFE-CFE) films are influenced by the morphology (packing) of the polymer. When grain sizes are smaller, the formation of such morphology is hindered, resulting in a lower dielectric constant. Therefore, these findings are consistent with the measured dielectric constant values.

In summary, the conducted experiments demonstrate the feasibility of organic doping to enhance the dielectric constant, utilizing both small molecules and polymers with a high dielectric constant for this purpose. However, the observed phase separation in such blends significantly disrupts charge transport within the organic semiconductors, thereby impeding their practical application.

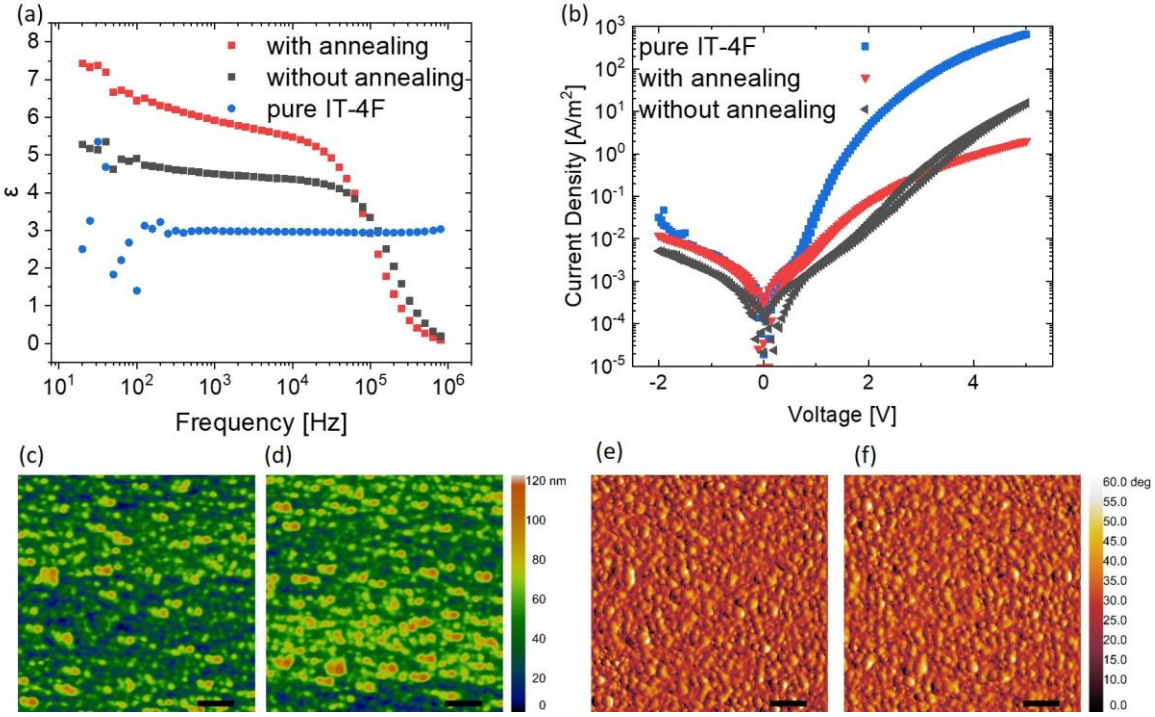

Figure 4.5. (a) Dielectric constant of pure IT-4F (blue) and blends of IT-4F with p(VDF-TRFE-CFE) with (red) and without annealing (black). (b) Double carrier device J-V curves for devices made from IT-4F (blue) and blends of IT-4F with p(VDF-TRFE-CFE) with (red) and without annealing (black). The thickness of the IT-4F layer was determined to be 190 nm for pure IT-4F and 230 nm for the blend with p(VDF-TRFE-CFE). For all devices, a TPBi interlayer was inserted. (c) AFM-height picture of a blend from IT-4F with p(VDF-TRFE-CFE) without annealing. (d) AFM-height picture of a blend from IT-4F with p(VDF-TRFE-CFE) after annealing. (e) AFM-phase picture of a blend from IT-4F with p(VDF-TRFE-CFE) without annealing. (f) AFM-phase picture of a blend from IT-4F with p(VDF-TRFE-CFE) after annealing. The scalebar for all AFM-pictures is 2 µm.

4.3. Titanium dioxide nanoparticles as additive to increase the dielectric constant

The mechanism for increasing the dielectric constant, as discussed in the preceding section, can also be achieved through the utilization of inorganic nanoparticles. To mitigate material costs and potential environmental impacts, inexpensive and readily available materials are preferred for nanoparticles used in this project. This rationale has led to the selection of TiO_2-NPs for the experiments conducted in the project. For the same reasons as discussed in the previous section, IT-4F is employed as the organic semiconductor, as depicted in its structural formula in Figure 4.6(c).

To incorporate TiO_2-NPs into an organic film, they cannot be used without further treatment such as encapsulation, coating, or masking. TiO_2 is inherently polar due to its ionic bonds, making TiO_2-NPs hydrophilic.[135] This characteristic poses challenges when dealing with organic solvents and the organic semiconductor utilized in the experiments, which are hydrophobic. If TiO_2-NPs were directly mixed with the organic semiconductor, they would aggregate, resulting in the formation of clusters within the organic semiconductor film. This contradicts the desired outcome of achieving an ideal dispersion of the TiO_2-NPs within the film. This behavior is schematically illustrated in Figure 4.6(a).

To prevent such issues, the TiO_2-NPs can be coated with surfactants. Surfactants are a class of materials that have both hydrophobic and hydrophilic parts. The hydrophobic portions typically consist of long alkyl chains, while the hydrophilic portions are usually polar groups such as acids or amines.[136] In this study, dodecylphosphonic acid and hexylamine were used as surfactants. The molecular structure of these molecules is shown in Figure 4.2 and d respectively. These surfactants cover the TiO_2-NPs with their hydrophilic ends, leaving the hydrophobic ends exposed outward from the TiO_2-NPs. A schematic representation of the TiO_2-NPs coated with surfactants can be seen in Figure 4.6(b).

Viewed from a solvent perspective, the coated TiO_2-NPs appear to be hydrophobic because only the alkyl chain interacts with the solvent. With this coating, the TiO_2-NPs can be dispersed in an organic solvent and incorporated into an organic film without or with minimal aggregation, thereby increasing the dielectric constant of the film, as illustrated in Figure 4.6(b).

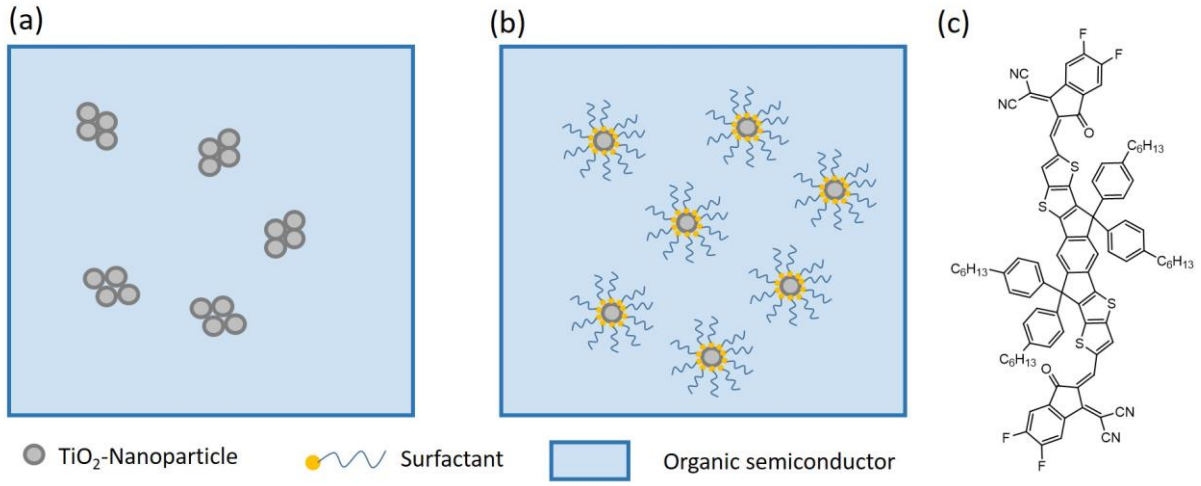

Figure 4.6. (a) Schematic drawing of bare TiO_2-NPs forming aggregates in an organic semiconductor film. (b) Schematic drawing of coated TiO_2-NPs dispersed in an organic semiconductor film. (c) Molecular structure of IT-4F.

The dielectric constant for pure TiO_2 depends on the exact crystal structure and even on the crystal axis. For typical anatase-type TiO_2, a dielectric constant of $\varepsilon = 31$ is reported.[137] The TiO_2-NPs used in this project are also of the anatase type. As shown in Figure 4.7(a), incorporating coated TiO_2-NPs into a film consisting of 66 % (w/w) IT-4F and 33 % (w/w) coated TiO_2-NPs increases the dielectric constant by one order of magnitude, from $\varepsilon = 3$ for pure IT-4F (black) to $\varepsilon > 30$ for the blend of IT-4F with TiO_2-NPs (red). This significant increase in the dielectric constant would be large enough to facilitate the separation of an exciton into free charge carriers without the need for a second layer within an OSC.[99]

The morphology of the films changed upon incorporating the TiO_2-NPs, although not as significantly as observed with organic doping. An increased roughness compared to pure IT-4F can be observed in the AFM picture of the blend (Figure 4.7(b)), as the coated TiO_2-NPs are much bulkier than IT-4F. However, the wide distribution of spots in this AFM image indicates a good dispersion of the TiO_2-NPs in the film. This good dispersion is further confirmed by the

AFM phase image of the blend (Figure 4.7(c)), where changes in phase occur rapidly rather than over larger areas as seen in organic blends. In contrast, no phase change within the film is observed for pure IT-4F (Figure 4.7(e)), as expected for a pure organic semiconductor film. The overall thickness of the films is also comparable, with a film of pure IT-4F having a thickness of 119 nm and the film with incorporated TiO_2-NPs measuring 143 nm.

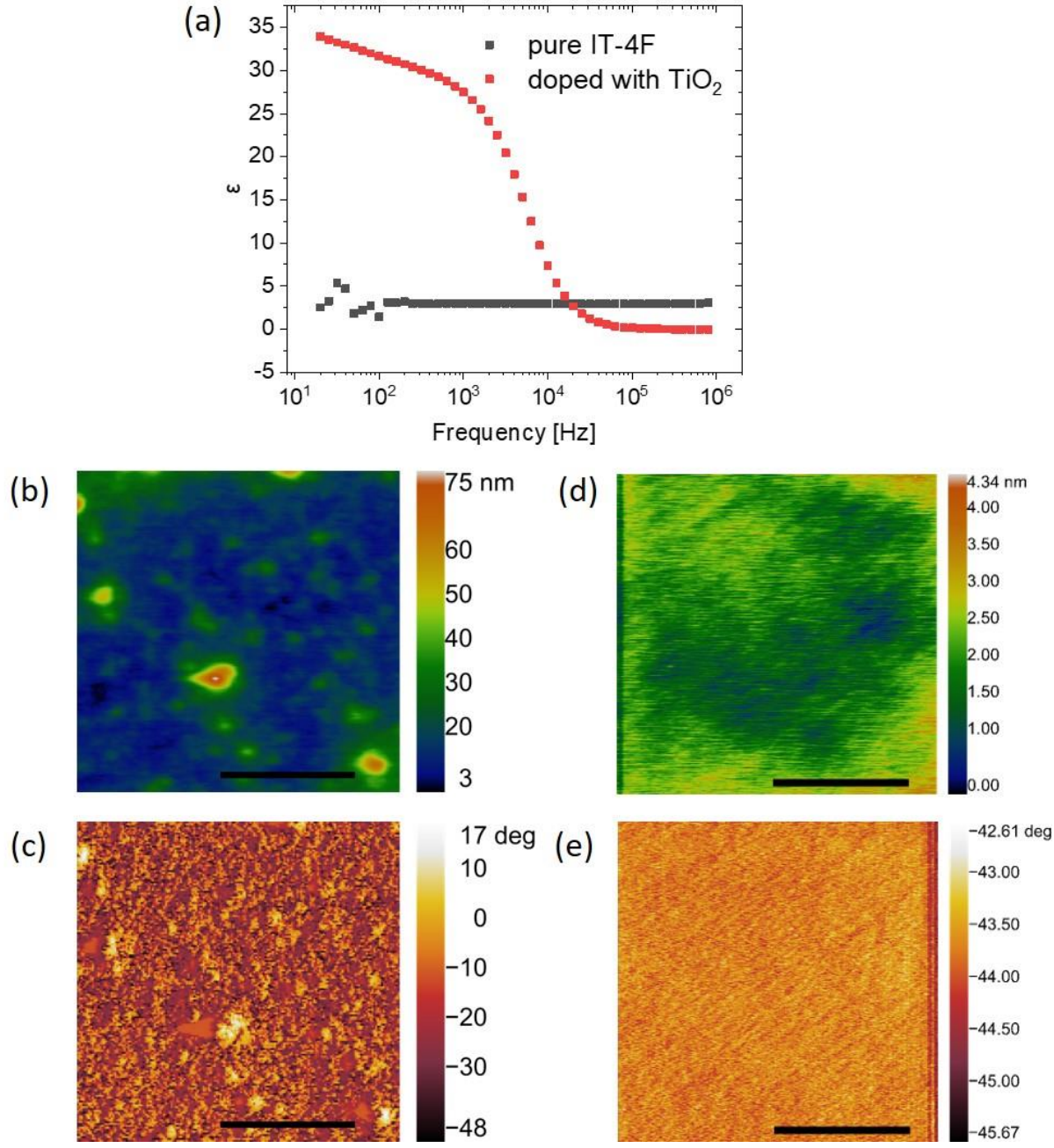

Figure 4.7. (a) Dielectric constant for a film of pure IT-4F (black) and a film of IT-4F doped with coated TiO_2-NPs (red). (b) AFM-height picture of the IT-4F film doped with coated TiO2-NPs. (c) AFM-phase picture of the IT-4F film doped with coated TiO_2-NPs. (d) AFM-height picture of pure IT-4F. (e) AFM-phase picture of pure IT-4F. The scalebar for all AFM-pictures is 2 µm.

To further explore the impact of doping IT-4F with TiO_2-NPs a comparison is made between a double carrier device using the doped film and one fabricated with pure IT-4F. The resulting J-

V curves are illustrated in Figure 4.8(a), black for pure IT-4F and red for the blend of IT-4F with TiO_2-NPs. A built-in voltage of $V_{bi} = 0.7\,V$ is observed for the pure IT-4F device. In case for the blend of IT-4F with TiO_2-NPs, V_{bi} reduces to $V_{bi} = 0.3\,V$. Despite this difference, the current density in the diffusion-dominated regime for both devices, whether made of pure IT-4F or the TiO_2-doped film, is within the same order of magnitude. This marks an improvement over the previously discussed organic doped films, where doping led to a reduction in current density. Nevertheless, the reduction in the built-in voltage suggests that the TiO_2-NPs may play a role in the charge transport mechanism.

In Figure 4.8(b), the behavior of the devices under reverse bias under illumination is depicted. In a double carrier device, under reverse bias, no charge injection occurs, so the number of charge carriers is depending upon the separated excitons. In a standard organic semiconductor exhibit a low dielectric constant, excitons generated by light absorption typically do not separate into free charges but rather recombine, leading to the elimination of charges. Thus, under reverse bias, no current should be measured except for a small leakage current. However, for films with an increased dielectric constant, exciton separation into free charges becomes easier, potentially resulting in an increased current under reverse bias. This behavior is illustrated in Figure 4.8(b). While no current can be observed under reverse bias for pure IT-4F due to its low dielectric constant (black), the TiO_2-doped film behaves differently (red). It clearly exhibits a current under reverse bias, indicating the presence of generated charge carriers. This observation aligns with the measured increase of the dielectric constant, which facilitates the separation of excitons into free charges.

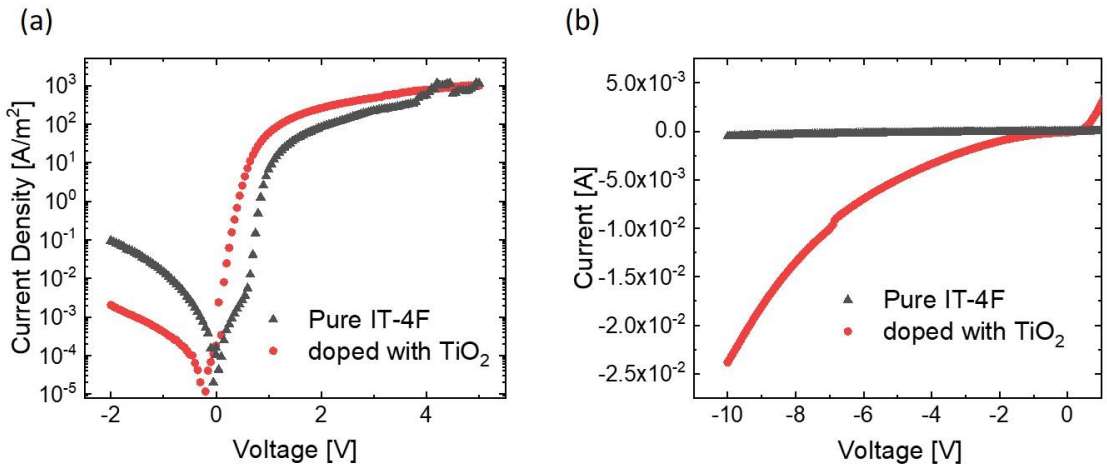

Figure 4.8. (a) J-V characteristics for a double carrier device in the dark for pure IT-4F (black) and IT-4F doped with coated TiO_2-NPs (red). (b) Current voltage characteristics at reverse bias under illumination for pure IT-4F and (black) and the IT-4F doped with coated TiO_2-NPs (red).

To further investigate the charge transport properties and the influence of TiO_2-NPs when blended into IT-4F, single-carrier devices were fabricated using TiO_2-NP-doped IT-4F and compared them to devices made of pure IT-4F. In Figure 4.9(a), the temperature-dependent electron-only J-V characteristics for a single-carrier device made of IT-4F blended with TiO_2-NPs are displayed. When juxtaposed to the electron-only device made of pure IT-4F in Figure 4.9(b), both devices exhibit similar shapes and values. Moreover, the decrease in

current with decreasing temperature shows no significant difference between the two devices. Hence, it can be inferred that the addition of TiO_2-NPs to the IT-4F film does not affect electron transport within the blend. The robust electron transport properties of IT-4F are unsurprising, given its design to efficiently transport electrons in BHJ OSCs.[138]

On the contrary, due to poor hole injection from the bottom contact into IT-4F, the J-V characteristic of the hole-only device is primarily dominated by leakage, as illustrated in Figure 4.9(d). The presence of leakage current is evident from the lack of temperature dependence on forward bias in this plot. Additionally, for reverse bias, the temperature dependence is only mildly pronounced. This still indicates an injected current from the MoO_3 contact, but the increase in current density between 295K and 275 K (red and blue curve in Figure 4.9(d)) hint that the device changed during the measurement. As the layer thickness of the IT-4F layer is 121 nm, the mild temperature dependence in reverse bias can also result from the series resistance of ITO. The series resistance of ITO starts to limit the measured current density for $J > 10^3$ A/m^2, as occurs in reverse bias. Furthermore, the fact that the hole current density values reach only 10^1 A m^{-2} in forward bias without any temperature dependence indicates that the real device current is even below the leakage current, indicating a severe hole injection problem for pristine IT-4F from an PEDOT:PSS contact. However, doping IT-4F with TiO_2-NPs alters the hole current behavior, exhibiting temperature dependence even under forward bias (Figure 4.9(c)). This change in behavior is accompanied by a significant shift in the curve shape compared to pure IT-4F. The increase in current under forward bias is much more pronounced, while the maximum current density under reverse bias is three orders of magnitude lower than that of pure IT-4F. These findings indicate that the hole injection into TiO_2-NPs-doped IT-4F is substantially influenced by the presence of TiO_2-NPs. Based on this data, it cannot be ruled out that, despite the coating of TiO_2-NPs some kind of phase separation occur, which strongly reduces the hole injection from MoO_3. Furthermore, the measured electron and hole currents seems to be unbalanced, but it remains an open question, whether this is a result of the semiconductor's properties or an injection problem.

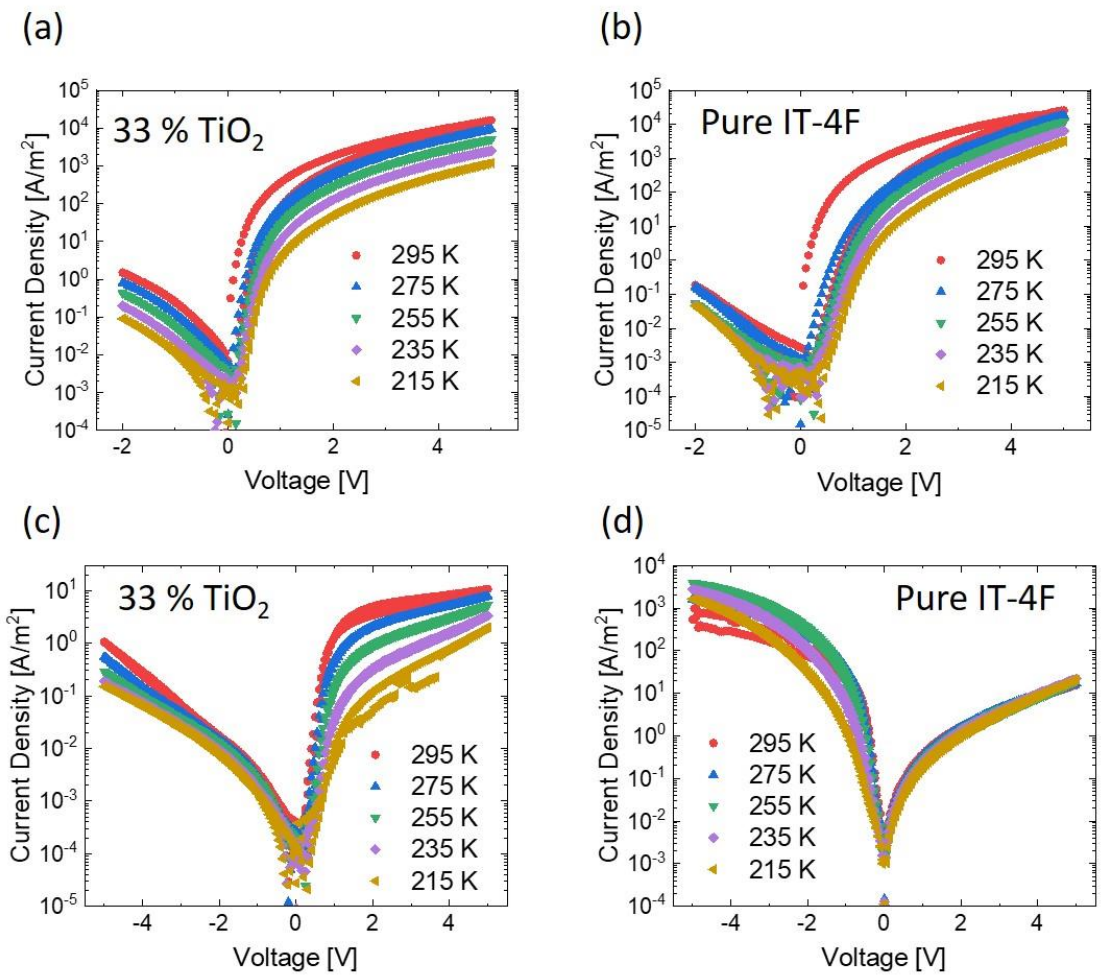

Figure 4.9. Temperature dependent J-V diagrams of single carrier devices. (a) EO of IT-4F blended with coated TiO_2-NPs. (b) EO of pure IT-4F. (c) HO of IT-4F blended with coated TiO_2-NPs. (d) HO of pure IT-4F.

Despite the observed effects on hole transport in IT-4F doped with TiO_2-NPs, an OSC incorporating this blend was fabricated to explore whether the increased dielectric constant would enhance the photovoltaic efficiency. Figure 4.10(a) displays the J-V characteristics of such an OSC under illumination (red), compared to an OSC comprised of pure IT-4F (black). In forward bias for $V>V_{bi}$, the injected carriers dominate the current. Since the electron current in both pristine and blend device are nearly equal and are much higher than the hole current there is no significant difference in current density, as expected. Obvious is only the smaller V_{bi} for the blend, as also been discussed for Figure 4.8(a). In reverse bias, the difference in the effect of illumination on the pristine and blend film is clearly visible.

To evaluate the efficiency of the OSCs, the fourth quadrant of the current-voltage characteristics needs to be examined, as depicted in Figure 4.10(b), with black for OSCs made of pure IT-4F and red for OSCs from TiO_2-doped IT-4F. As anticipated, in the absence of illumination, the measured current is negligible (empty symbols in Figure 4.10(b)). However, when light is applied to the OSC, a negative current is detected in both cases, attributable to the generation of charge carriers by photon absorption and subsequent exciton separation into free charges. As expected, the negative current is noticeably higher for the device incorporating the TiO_2-NPs-doped organic semiconductor layer. According to the theory of

this project, this is the effect of the increased dielectric constant of the film, which allows photogenerated excitons to easier separate into free charge carriers.

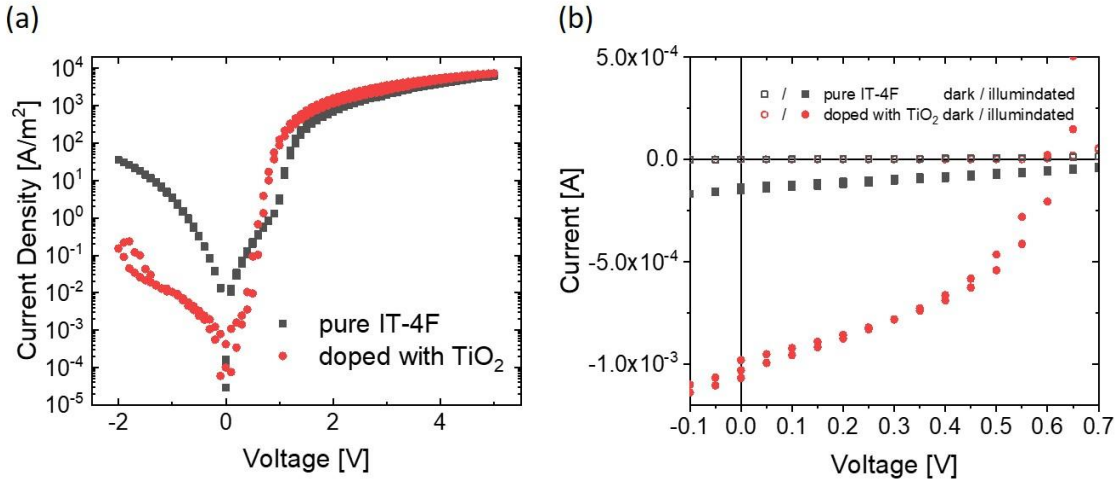

Figure 4.10. (a) J-V diagram of illuminated OSCs made from pure IT-4F (black) and IT-4F doped with coated TiO_2-NPs (red). (b) Fourth quarter of the current voltage characteristic of OSCs under dark conditions (empty symbols) and illuminated conditions (AM 1.5, filled symbols) for pure IT-4F (black) and IT-4F doped with coated TiO_2-NPs (red).

To quantify this efficiency increase, the values extracted from Figure 4.10(b) for determining the efficiency, as described in subsection 2.4.4, are listed in Table 4.1. From these values, it is evident that the short circuit current is a factor of 20 larger for the TiO_2-NPs-doped film than for pure IT-4F. Additionally, the current at the maximum power point is 20 times larger for the TiO_2-NPs-doped film compared to pure IT-4F. However, the open circuit voltage is higher for the OSC made of pure IT-4F as compared to the OSC made of TiO_2-NPs-doped IT-4F. The lower than ideal values determined for V_{OC} mainly result from the barrier created at the hole contact for IT-4F. The reason for the further reduction of V_{OC} for the OSC doped with TiO_2-NPs remains unknown. Conversely to V_{OC}, for the voltage at the maximum power point (V_{MPP}), the values are close together for both OSCs tested.

When the fill factor is calculated for both devices, it is evident that the doping of IT-4F with TiO_2-NPs can increase the FF by 66 %. Upon determining the efficiency η for both devices, it becomes apparent that the OSC using IT-4F doped with TiO_2-NPs outperforms an OSC made of pure IT-4F as the active layer. The numbers indicate an increase by one order of magnitude in efficiency, rising from 0.01 % for pure IT-4F to 0.13 % for IT-4F doped with TiO_2-NPs. This demonstrates that doping IT-4F with TiO_2-NPs, associated with an increase in the dielectric constant, can significantly enhance the efficiency of an OSC.

Table 4.1. Parameters to determine the efficiency of an OSC according to chapter 2.4.4 for the OSCs made of pure IT-4F and IT-4F doped with coated TiO_2-NPs under the illumination of an AM1.5 spectrum.

Parameter	Pure IT-4F	IT-4F doped with coated TiO_2-NPs
I_{SC}	$5.6 \cdot 10^{-5}$ A	$1.0 \cdot 10^{-3}$ A
V_{OC}	0.9 V	0.6 V
I_{MPP}	$2.6 \cdot 10^{-5}$ A	$6.3 \cdot 10^{-4}$ A
V_{MPP}	0.5 V	0.45 V
FF	26.7	44.5
η	0.01 %	0.13 %

4.4. Conclusions

In conclusion, this chapter delves into methods for increasing the dielectric constant of organic semiconductor thin films. This is achieved through doping the organic semiconductor with high dielectric materials, such as the small molecule CAA, the polymer p(VDF-TRFE-CFE), and also inorganic TiO_2-NPs. Incorporating these dopants into a film of an organic semiconductor results in an elevation of the dielectric constant. However, phase separation is observed for blends with the organic materials for enhancing the dielectric constant. This phase separation hinders the application of these blends in organic electronic devices due to the loss in electrical properties of the film.

To circumvent phase separation and achieve an increased dielectric constant, coated TiO_2-NPs were employed. The coating renders them dispersible in the organic semiconductor film. In contrast to the organic dopants, the electrical properties of the doped film compared to the non-doped film remain relatively unchanged. The efficiency of an OSC composed of IT-4F doped with TiO_2-NPs can be increased by one order of magnitude compared to an OSC made of pure IT-4F. However, the resultant efficiency of 0.13 % is still an order of magnitude lower than what can be attained with standard BHJ OSCs. Additionally, for the system comprising IT-4F and TiO_2-NPs, it cannot be ruled out that the TiO_2-NPs contributes to the charge transport within this system.

Hence, while an increase of the dielectric constant can enhance the efficiency of an OSC, it does not elevate it to a level where such systems rival standard BHJ OSCs. The straightforward blending approach encounters numerous challenges, primarily stemming from phase separation, which must be surmounted to produce efficient single-layer OSCs with an elevated dielectric constant.

4.5. Methods

In this section, the materials and methods used in this chapter are provided.

Materials

Camphoric acid anhydride (CAA) was purchased from Alfa Aesar, 3,9-bis(2-methylene-((3-(1,1-dicyanomethylene)-6,7-difluoro)-indanone))-5,5,11,11-tetrakis(4-hexylphenyl)-dithieno[2,3-d:2',3'-d']-s-indaceno[1,2-b:5,6-b']dithiophene (IT-4F) was purchased from Ossila LTd., Poly[2-methoxy-5-(2-ethylhexyloxy)-1,4-phenylenevinylene] (MEH-PPV) was synthesized in house by Verona Maus, poly(3,4-ethylenedioxythiophene) polystyrene sulfonate (PEDOT:PSS) was purchased from Heraeus Gruppe, poly(9,9-bis(3-(pentafluoroethanesulfonylimidosulfonyl)propyl)fluorene-2,7-diyl-*alt*-1,4-phenylene-(*p*-trifluoromethylphenylimino)-1,4-phenylene) sodium salt (p-PTFF) was synthesized by Q. M. Koh and Q. J. Seah from the university of Singapore as describe by Ricciardulli et. al. [139], Acetonitrile 99.5 % (ACN) was purchased from Honeywell, Chlorobenzene (CB) and Chloroform (CF) were purchased from Fisher chemicals, water free Tetrahydrofuran (THF) was purchased form Merck, hydrophobic coated titan dioxide nanoparticles (TiO_2-NP) were purchased from PlasmaChem GmbH. CB and CF were purified by a MBSPS 5 from MBraun before use, ACN was degassed using nitrogen. All other materials were used as received.

Substrate preparation

Glass substrates and ITO-covered glass substrates underwent a rigorous cleaning process in a cleanroom prior to use. They were first treated with water, followed by scrubbing with soap, and then submerged in acetone and isopropanol within an ultrasonic bath. Following this, they were blown dry with nitrogen and placed into an oven at 140°C for 10 minutes. Finally, the samples were exposed to a UV-Ozone oven for an additional 20 minutes.

Device structure and fabrication

In this study, three types of devices were manufactured: EO, HO, and DC or OSCs. The fabrication of these devices took place within a nitrogen-filled glovebox. All metals utilized in the study were evaporated using a system similar to the one described in Subsection 2.5.1. The primary distinction lies in the method of metal evaporation; rather than thermal heating, the metals were evaporated by applying electricity, inducing their evaporation.

The in this study fabricated EOs had the following device structure (from bottom to top):

Al / organic semiconductor / Ba / Al

Here, the bottom Al layer has a thickness of 30 nm, the Ba layer of 5 nm and the top Al layer a thickness of 100 nm. After the deposition of the bottom Al layer, the substrate is exposed to air for 5 minutes.

For HO the following structure is used:

ITO / HIL / organic semiconductor / MoO_3 / Al

The MoO_3-layer exhibits a thickness of 10 nm. For the top Al-contact, the thickness is 100 nm. The HIL-layer made of PEDOT:PSS were spincoated with 1200 rpm for 60 seconds and subsequently 4000 rpm for 20 seconds. Afterwards the devices were annealed for 10 minutes at 140°C.

For the DC and OSC devices, the following structure is used:

ITO / HIL / organic semiconductor / Ba / Al

Ba has a thickness of 5 nm, Al of 100 nm. For devices with MEH-PPV, PEDOT:PSS was processed analogues to the HIL-devices, as described above. For the HIL made of p-PTFF, a solution of 12.5 mg ml-1 in ACN was prepared. To dissolve the p-PTFF, the mixture was heated up to 80°C and then mechanically shaken for 30 seconds. This procedure of heating and shaking was repeated up to 7 times. The p-PTFF was then spincoated with 2000 rpm for 30 seconds.

For the films of pure MEH-PPV, MEH-PPV was dissolved in CB with a concentration of 6 mg ml^{-1} stirred for 16 hours at 60°C and spincoated with 1000 rpm for 60 seconds and subsequently with 4000 rpm for 30 seconds. For the blend of MEH-PPV with CAA, MEH-PPV and CAA were dissolved in CF to achieve an overall concentration of 6 mg ml-1. These films were treated the same way as for pure MHE-PPV. The procedure was analogously repeated for blends with p(CDF-TRFE-CFE), with the difference, that THF as solvent was used.

Pure IT-4F was dissolved in CB at a concentration of 20 mg ml-1, stirred at 60°C for 16 hours and spincoated at 500 rpm for 60 seconds and subsequently at 4000 rpm for 30 seconds. The blends of IT-4F with p(CDF-TRFE-CFE) were prepared by dissolving the IT-4F as well as the p(VDF-TRFE-CFE) in THF with an overall concentration of 20 mg ml^{-1}. The preparation of films from this solution were analogue to pure IT-4F. If the films were annealed, the annealing takes 1 hours at a temperature of 110°C. The blends of IT-4F with the hydrophobic coated TiO2-NPs were prepared with CB as solvent and an overall concentration of 20 mg ml^{-1}. The mass-fraction of TiO_2-NPs were 33 %. The spincoating of the film follows the same procedures as described for pure IT-4F.

For all HO and DC/OSC devices PEDOT:PSS was used with the exception of the DC/OSC devices made of the blend of IT-4F with TiO_2-NPs, were p-PTFF was used.

Device characterization

To determine the electrical properties of the organic semiconductor devices, the current-voltage characteristic curve have been recorded using a Keithley 2400 Voltmeter inside a nitrogen filled glovebox. The dielectric constant was determined using impedance spectroscopy. These measurements were conducted using an Agilent 1284A PERCISION LCR METER also inside a nitrogen filled glovebox.

AFM-measurements were carried out with a Dimension 3100 AFM made by Digital Instruments. The light-microscope picture was recorded with a DMP750P Leica microscope. Thickness measurements were performed with a Brucker Dektak XT profilometer.

5. Ohmic electron injection into organic semiconductors by solution-processed and evaporated organic interlayers

This chapter was 2023 published as “Ohmic electron injection into organic semiconductors by solution-processed and evaporated organic interlayers” in Advanced Material Interfaces, Volume 10, Issue 19, page 2202424 together with Gert-Jan A. H. Wetzelaer and Paul W. M. Blom.

Author Contributions

David Trieb performed the experiments, analyzed the data and wrote the manuscript. Gert-Jan A. H. Wetzelaer and Paul W. M. Blom proposed and supervised the project and corrected the manuscript.

5.1. Summary

Efficient electron injection from an electrode into an organic semiconductor remains a problem to solve for efficient organic semiconductor devices. This chapter presents a general method to form an ohmic electron contact by inserting a thin organic interlayer between the metal electrode and the organic semiconductor. Here, it is demonstrated that inserting an interlayer of a few nanometers of an organic semiconductor with a lower electron affinity than the transport material can improve the injected electron current by over three orders of magnitude. The electron current becomes space-charge limited, demonstrating that the interlayer-enhanced contact is ohmic. The ohmic-contact formation by inserting a thin interlayer is ascribed to the elimination of barrier formation as a result of direct contact between the metal and organic semiconductor. Additionally, it is demonstrated that it is possible to achieve solution processing of such interlayers on top of organic semiconductors. The method is generalized for different interlayer materials as well as for different organic semiconductors, providing a general method for ohmic electron injection in organic devices.

5.2. Introduction

As discussed in Section 2.2.1. ohmic charge injection is essential for all kind of efficient organic semiconducting devices. Typically, metals with a low work function, such as barium or calcium are applied.[140] Additionally, thin interlayers of metal salts like LiF or Cs_2CO_3 are commonly used.[141] For hole injection, transition metal-oxides, such as MoO_3 are often used as an inorganic injection layer, because of their extremely high work function of up to 6.9 eV.[142, 143] However, despite their very high work function, it was recently found that the contacts formed with these metal oxides are non-ohmic. The unexpected hole injection barrier could be eliminated by using thin (3-5 nm) tunneling interlayers of organic semiconductors with a high ionization energy.[59] These interlayers act as a spacer layer, preventing barrier formation upon direct contact between the electrode and the organic semiconductor due to electrostatic interactions. The high ionization energy of the interlayer allows the Fermi-level of the metal to align with the ionization energy of the semiconductor, resulting in an ohmic contact.

Since a hole-injection barrier between MoO_3 and organic semiconductors was found despite the more than sufficiently high work function of the MoO_3 electrode, this raises concerns about the analogous case of electron injection from low work function contacts. Indeed, for the high-mobility electron-transporting polymer poly((N,N'-bis(2-octydodecy)naphthalene-1,4,5,8-bis(dicarboxoimide)-2,6-diyl)-alt-5,5'-(2,2'-bithiophene)) [PNDI(2OD)-2T], Steyrleuthner et al. found that ohmic electron injection could not be achieved, despite the use of a wide range of electrode materials with different work functions.[125] Intriguingly, the electron affinity of PNDI(2OD)-2T is rather high at 3.8 eV, which should in principle be easily accessible for electron injection from low work function metals. As such, it seems that the formation of ohmic electron contacts is not straightforward, similar to the recent observations for the formation of ohmic hole contacts.[6] Multiple reasons have been discussed for the formation of charge-injection barriers between metals and organic semiconductors, such as chemical reactions at the interface leading to Fermi-level pinning states.[144] In addition, the overlap between metallic states and molecular levels give rise to broadening of the latter, leading to an induced density of interface states, to which the Fermi level is pinned.[145] Damage to the organic semiconductor top interface may also occur when a metal is evaporated on top, potentially leading to barrier formation.[42] For hole injection from metal oxides, image potentials due to a dielectric contrast at the interface were associated with barrier formation, which is also generally present at metal-organic interfaces.[143]

For hole injection, the use of thin organic interlayers could solve the problem of barrier formation.[6] As a practical demonstration of the use of tunneling interlayers to form ohmic contacts, a highly efficient single-layer OLED was fabricated, using a C_{60} interlayer for hole injection and a 2,2',2"-(1,3,5-benzinetriyl)-tris(1-phenyl-1-H-benzimidazole) TPBi interlayer for electron injection.[60] As a result of the formed ohmic contacts, a high external quantum efficiency of 19 % was obtained despite the absence of transport and blocking layers, and an extremely low operating voltage could be achieved due to the absence of injection barriers. These results show promise for efficient electron injection by using thin interlayers. As a second example of the use of such an injection strategy, tunneling interlayers have been shown to enhance the hole injection in OFETs.[58]

In this chapter it is demonstrated that ohmic electron contacts can be formed by using thin interlayers of organic semiconductors with a low electron affinity. Moreover, it is shown that these interlayers can be processed from solution, without compromising charge injection. Several interlayer materials are used for efficient electron injection from an aluminum electrode into the polymer PNDI(2OD)-2T and the non-fullerene acceptor IT-4F. These results highlight the potential of using tunneling interlayers in solution-processed organic devices.

5.3. Results and Discussion

To investigate the electron injection in the presence of a thin tunneling interlayer, electron-only devices as displayed schematically in Figure 5.1(a) have been fabricated. The devices are based on the polymer PNDi(2OD)-2T, of which the molecular structure is shown in Figure 5.1(c). The polymer has a high electron mobility and finds applications in n-type transistors and organic solar cells.[146] As trap-free electron transport has been observed for this polymer, the formation of an ohmic electron contact should result in a space-charge-limited current, rendering this polymer ideal for investigating electron injection.[147] Moreover, as observed by Steyrleuthner et al., ohmic electron injection could not be achieved with the conventional method of using low work function electrodes, despite investigating a wide range of injection layers.[125] In our electron-only devices, TPBi was chosen for the interlayer material, situated between the polymer layer and the aluminum top electrode. Usually, TPBi is used as an electron-transport material in organic semiconductor devices. The reason to chose TPBi for the interlayer material is the large energy offset between the lowest unoccupied molecular orbital (LUMO) of PNDi(2OD)-2T and TPBi of 0.9 eV. This is analogous to the interlayer requirement for improving hole injection, for which interlayers with a high ionization energy are required. The work function of the aluminum top electrode is not sufficient for direct electron injection into the LUMO of TPBi. Instead, the TPBi interlayer prevents direct contact between the metal and the polymer and the associated barrier formation upon contact, while the high LUMO of TPBi ensures that the Fermi level of aluminum can align with the LUMO of PNDI(2OD)-2T. The Fermi-level alignment then results in an ohmic contact where charges are transferred from the electrode, through the interlayer, into the polymer. An interlayer with too deep a LUMO (Figure. 5.1(b)), however, would result in Fermi-level pinning of Al below the LUMO of the interlayer, which results in misalignment of the electrode Fermi level with the LUMO of the polymer. Similarly, the work function of the used metal electrode should be at least as low as the electron affinity of the organic semiconductor, to ensure Fermi-level alignment, analogous to the case for hole injection.[59]

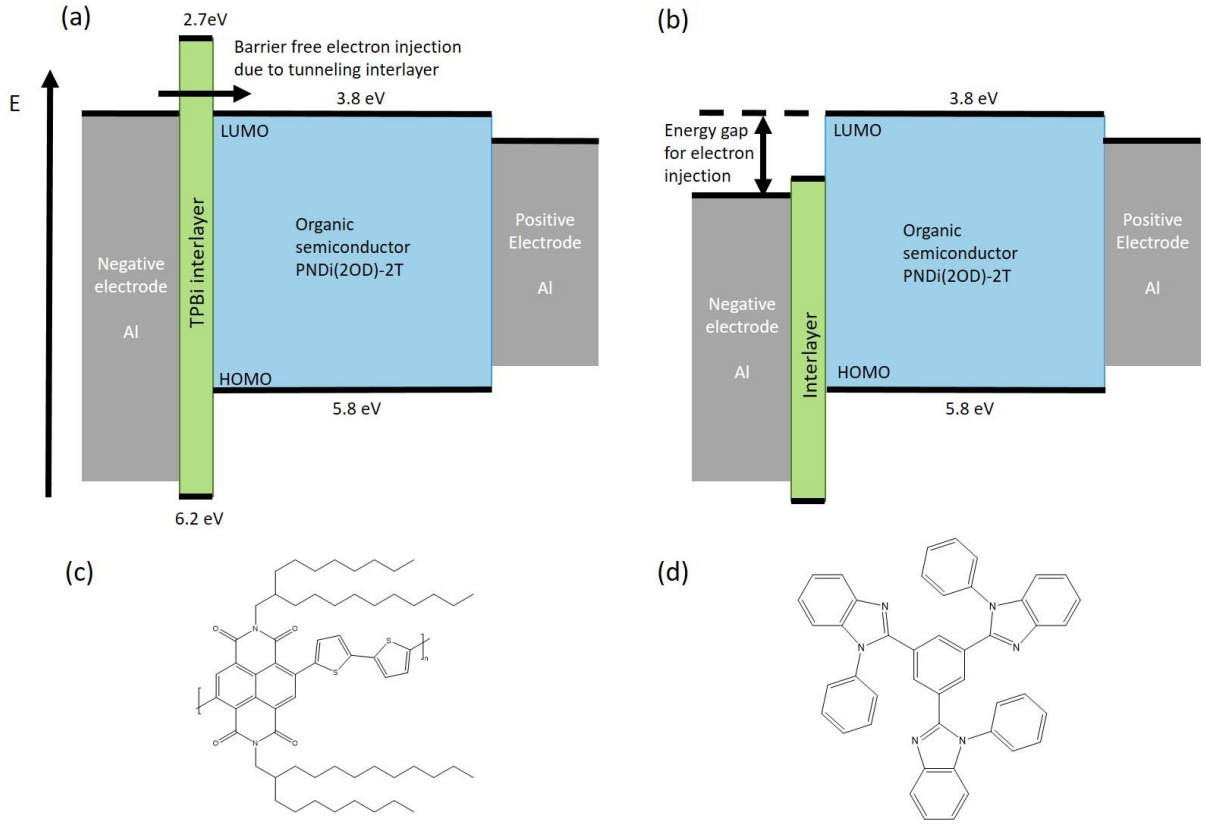

Figure 5.1 (a) Schematic energy band diagram showing Fermi-level alignment between the electrode and the LUMO of PNDI(2OD)-2T, due to a TPBi interlayer. (b) Schematic energy band diagram of a device with an interlayer with a deeper LUMO than PNDI(2OD)-2T, leading to an offset between the electrode Fermi level and the LUMO of PNDI(2OD)-2T. (c) Molecular structure of the organic semiconductor PNDI(2OD)-2T. (d) Molecular structure of the interlayer material TPBi.

To investigate the electron-injection properties, three types of electron-only devices were fabricated: one without interlayer, one with an evaporated interlayer, and one with a solution-processed interlayer. The interlayers were deposited on top of the PNDI(2OD)-2T layer. The solution-processed interlayer was spin coated from an ethanol solution, as ethanol does not affect the layer of the PNDI(2OD)-2T, as observed from AFM measurements, shown in Figure 5.2. In Figure 5.2(a), the AFM image of PNDI(2OD)-2T film is shown as deposited and in Figure 5.2(b) after a post-treatment with ethanol. It appears that the roughness of the film of PNDI(2OD)-2T is not increased after the use of ethanol. Also, no aggregation effects in the film can be determined. This behavior is attributed to the hydrophilic behavior of ethanol making it to a poor solvent in respect to PNDI(2OD)-2T.

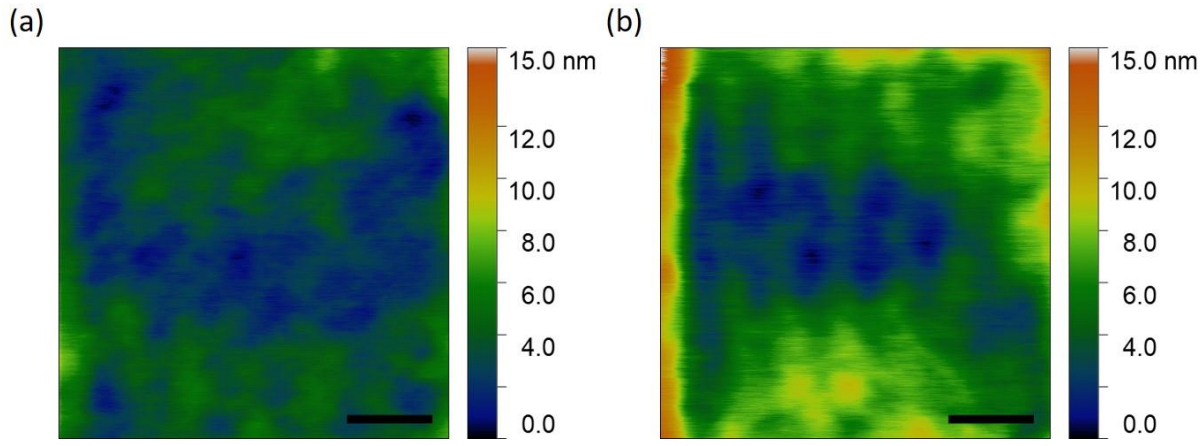

Figure 5.2. AFM images of a PNDI(2OD)-2T-film before (a) and after (b) spin casting ethanol on top. The scale bar is 2 µm.

Details on the solution preparation and the spin-coating procedure are provided in the Experimental Section. The thickness of the interlayer in the devices was 4 nm for both deposition methods. The current density (*J*) vs voltage (*V*) characteristics of these devices are shown in Figure 5.3. Upon insertion of a TPBi interlayer between the polymer and the top electrode, a substantial increase of the electron current density in forward bias is visible in Figure 5.3, where forward bias corresponds to injection from the aluminum top electrode. At 4 V, an increase in current density of about three orders of magnitude is observed, independent of the deposition method of the interlayer. These observations indicate that the electron injection is clearly enhanced by the addition of a tunneling interlayer, and, importantly, that the interlayer can also be processed from solution, without loss of function.

To further investigate the mechanism of electron injection, also electron-only devices with a Ba (5 nm) and LiF (1 nm) interlayer were fabricated, of which the *J*-*V* characteristics are displayed in Figure 5.3. It is observed that the current injected from these conventionally used interlayers is limited by the presence of a charge injection barrier. This is further confirmed when studying the activation energy of the injected current, which is larger in the absence of a TPBi interlayer, also pointing towards an energetic barrier for charge injection. In the case of a TPBi interlayer, reducing the metal work function with an additional barium interlayer (TPBi/Ba/Al) does not further improve the current, showing that Femi-level alignment is already achieved with a TPBi/Al contact.

It is further noted that the current in reverse bias, corresponding to electron injection from the aluminum bottom electrode, remains comparable for all devices. The injected current from the plain aluminum top electrode (forward bias) is lower in comparison, which may have several potential origins, such as damage of the top surface of the organic semiconductor the presence of different interface dipoles formed at the bottom and top electrode, for instance due to an oxide layer at the surface of the bottom electrode. [42, 148]

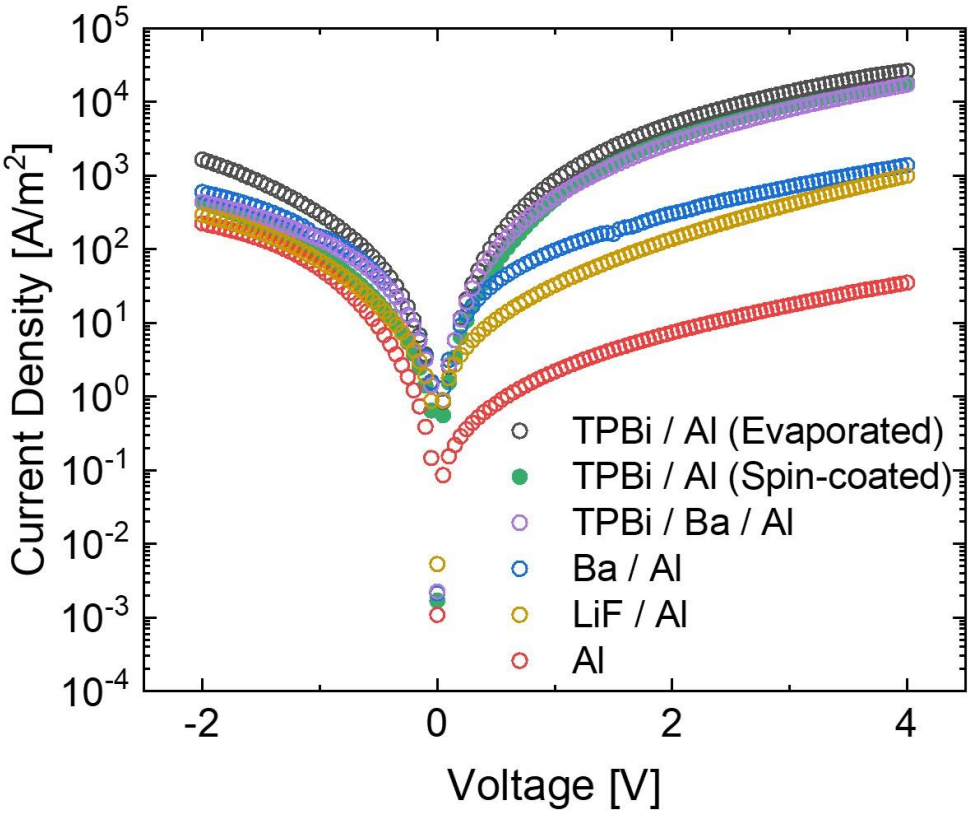

Figure 5.3. Current density versus voltage characteristics for electron only devices of the organic semiconductor PNDi(2OD)-2T, with a TPBi interlayer either thermally evaporated (black empty circles) or spin coated from ethanol solution (green filled circles), with an evaporated TPBi interlayer with Ba(5 nm)/Al(100 nm) on top (purple circles), with only a barium (5 nm) interlayer (blue circles), with only a lithium fluoride (1 nm) interlayer (ocher circles) and without interlayer (red circles).

To confirm that the deposition method the interlayer does not have a significant influence on the morphology, AFM micrographs of the surface of both films were taken (Figure 5.4). In Figure 5.4(a), the surface of the spin-coated TPBi film is shown and in Figure 5.4(b) the evaporated TPBi film as a reference, both on top of the polymer layer. The root mean square (RMS) roughness for the evaporated film is 1.87 ± 0.18 nm, compared to 1.33 ± 0.12 nm for the spin-coated film. This shows that equally smooth films can be obtained by spin coating of the interlayer as compared to evaporated layers. From the associated AFM phase images shown in Figure 5.5(a) for the spincoated TPBi and in Figure 5.5(b) for the evaporated TPBi, it is observed that for both deposition methods a continuous TPBi film is obtained, although it appears that a certain degree of molecular organization is obtained for the spin-coated film. For the layer stack with the spin-coated interlayer, a total thickness (including the polymer layer) of 131 ± 1.4 nm was determined, and 131 ± 3.1 nm for the layer stack with evaporated TPBi. The thickness of the pure PNDI(2OD)-2T film was measured to be 127 nm, confirming that in both cases a TPBi interlayer of 4 nm was present and that the polymer layer thickness remains unaffected by spin coating the interlayer on top.

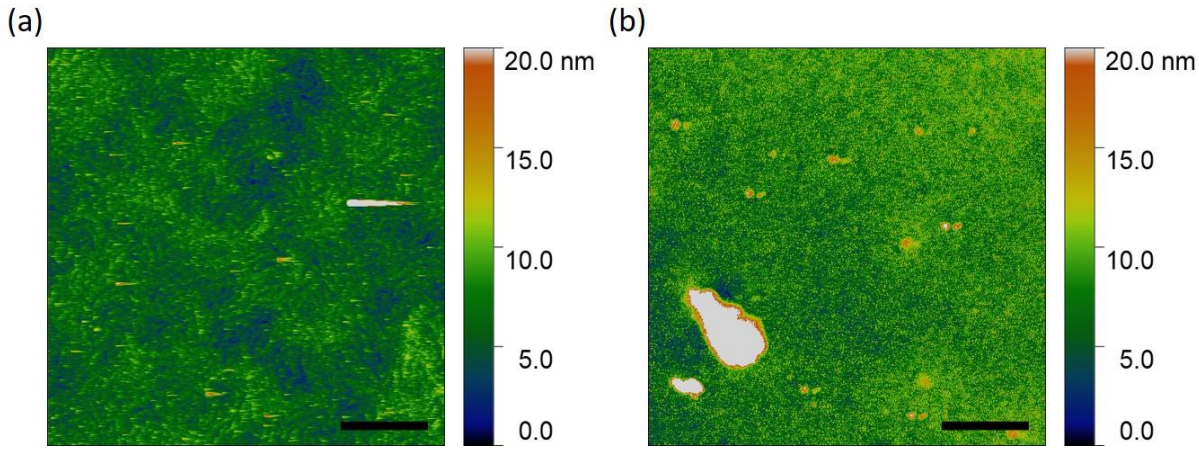

Figure 5.4. AFM images for TPBi deposited on top of PNDi(2OD)-2T via spin coating (a), and thermal evaporation (b). The scale bar is 2 µm.

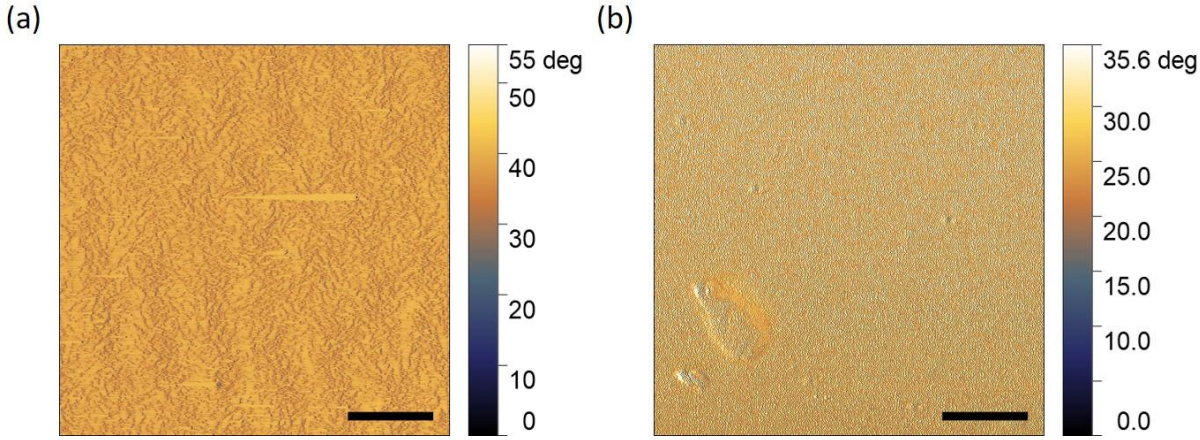

Figure 5.5. AFM phase images associated with the AFM images shown in Figure 3 for TPBi deposited on top of PNDI(2OD)-2T via spin coating (a), and thermal evaporation (b). The scale bar is 2 µm.

To assess whether the use of a TPBi interlayer yields an ohmic electron contact, it is investigated whether the injected current is space-charge limited. For ohmic injection, the magnitude of the space-charge-limited electron current will be determined by the electron mobility of PNDI(2OD)-2T, according to the Mott-Gurney square law, as displayed in Equation 5 in Section 2.2.2.[149]

Fitting the measured electron current with Equation 1 yields a mobility of 5×10^{-8} m^2 V^{-1} s^{-1}. This mobility is equal to the value determined previously for this polymer,[11] indicating that the current is indeed bulk limited and thus the electron contact can be considered ohmic, even without the use of reactive metals.[125]

For a more detailed analysis, temperature-dependent *J-V* curves were measured, as displayed in Figure 5.6. Subsequently, the experimental data was fitted with a numerical drift-diffusion model. This model includes a charge-carrier mobility that is dependent on the electric field, charge-carrier density, and temperature according to the extended Gaussian disorder model (EGDM).[66] The temperature dependence of the *J-V* characteristics is mainly governed by the energetic disorder of the polymer. As observed in Figure 5.6, a decrease in current of about one order of magnitude is observed by going from 295 K to 215 K for both deposition methods of the interlayer. Applying the EGDM, this temperature dependence corresponds to an

energetic disorder σ of 0.09 eV, as obtained previously for electron transport in this polymer.[147] It is noted that it is possible to model the devices from both interlayer deposition methods using the same parameters. No electron trapping was included, which can be expected considering the LUMO energy of PNDI(2OD)-2T is situated inside the trap-free window.[64] From these simulations, a room-temperature electron mobility of 2×10^{-8} m^2 V^{-1} s^{-1} was determined, which is slightly lower than the mobility obtained by Equation 1 since the mobility in the simulation is extrapolated to zero charge-carrier density and electric field. Overall, the simulations show that the current density is indeed governed by the electron-transport properties of PNDI(2OD)-2T and therefore not limited by an injection barrier.

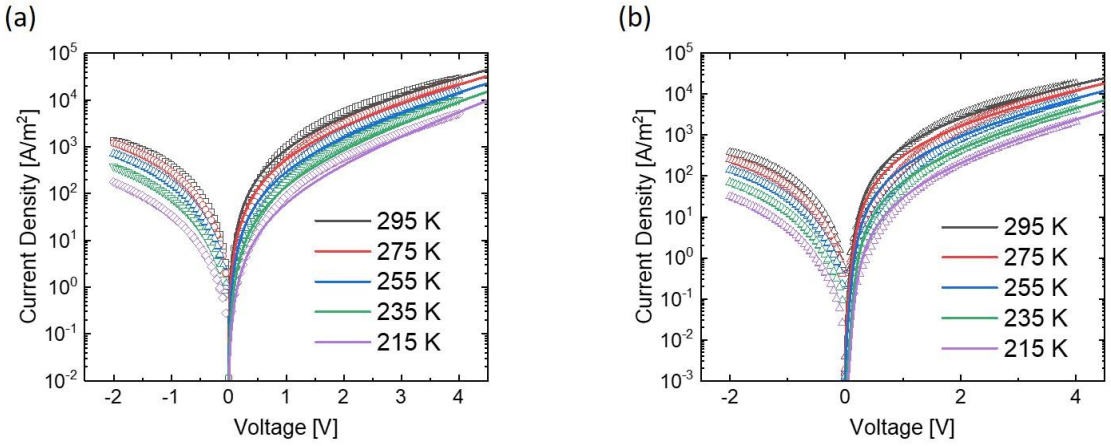

Figure 5.6. Temperature-dependent *J-V* characteristics for electron-only devices of PNDi(2OD)-2T with TPBi interlayers that were either evaporated (a) or spin coated (b). Symbols represent the measured data, the solid lines show the drift-diffusion simulations using the EGDM combined with ohmic injecting contacts. The film thicknesses of the PNDi(2OD)-2T layers equal 119 nm (a) and 129 nm (b).

Another approach to assess the impact of the interlayer on electron injection is by calculating the energy required for electrons to be injected into the organic semiconductor. This can be accomplished by plotting the temperature-dependent current density against the inverse of temperature multiplied by the Boltzmann constant k_b at a constant voltage. Figure 5.7 illustrates this relationship for the current density values measured at 2 V for the various top electrodes. These data points can be fitted using the Arrhenius equation:

$$J = A \exp\left(-\frac{E_a}{k_b T}\right). \tag{16}$$

Where J represents the current density, A is a constant, E_a and is the energy required for injection into the organic semiconductor. The results for E_a obtained from this fitting procedure are summarized in Table 5.1. These findings indicate that for all electrodes employing a TPBi interlayer, E_a is reduced compared to using a metal interlayer or even bare Al. Additionally, it is evident that, as previously discussed, the deposition technique of TPBi did not affect E_a, indicating that a reduction in E_a is consistently achieved regardless of the deposition method. This further substantiates the proposed concept of incorporating an interlayer to achieve ohmic electron injection into an organic semiconductor.

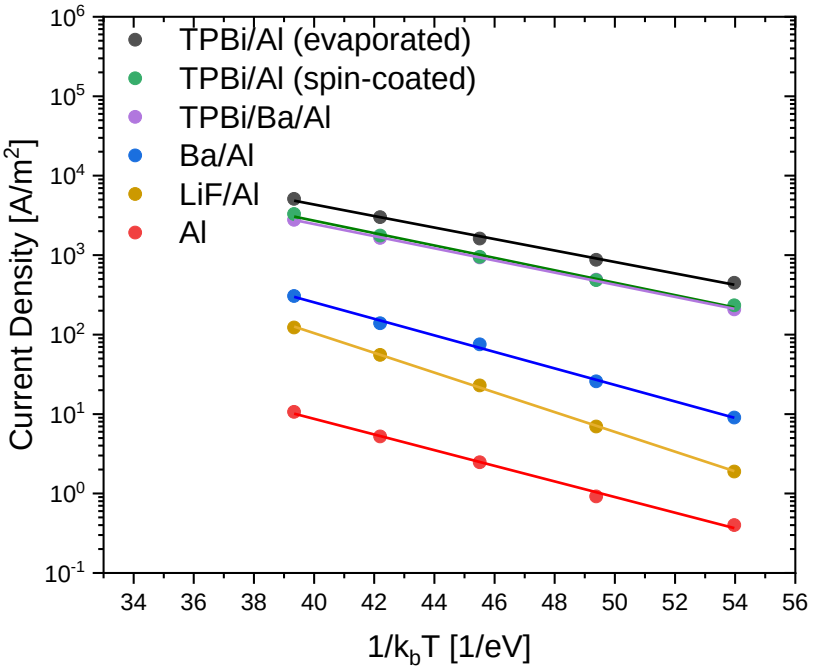

Figure 5.7. Arrhenius-like plot of the current density at 2 V versus the inverse temperature for electron only devices of the organic semiconductor PNDI(2OD)-2T for determination of the activation energy. The symbols represent the experimental data, while the lines are the corresponding fit with the Arrhenius equation. The devices comprise different interlayers at the electron-injecting contact: a TPBi interlayer either thermally evaporated (black) or spin coated from ethanol solution (green), a TPBi interlayer with barium and aluminum on top (purple), with only a barium interlayer (blue), with only a lithium fluoride interlayer (ocher) or without interlayer (red).

Table 5.1. Activation energy for the electron only devices of PNDi(20D)-2T with different interlayers. The data was determined fitting the data shown in Figure 5.7. using an Arrhenius equation.

Interlayer material & top electrode	Activation energy (eV)
TPBi/Al (evaporated)	0.17
TPBi/Al (spin-coated)	0.18
TPBi/Ba/Al	0.18
Ba/Al	0.24
LiF/Al	0.28
Al	0.23

To investigate if the application of a tunneling interlayer for electron injection can be generalized to more materials, also interlayers of bathocuproine (BCP) and 1,3,5-tri(m-pyridin-3-ylphenyl)benzene (TmPyPB) by means of thermal evaporation or spin coating from ethanol solution are applied. These materials are commonly used as electron-transport materials and have electron affinities significantly lower than PNDI(2OD)-2T, which is the expected main requirement for their use as thin interlayers for electron injection. The BCP and TmPyPB interlayers were all spin coated with the same recipe as for TPBi. In Figure 5.8(a) and 5.8(b), the *J-V* curves of devices with the different interlayer materials are shown. It is observed that the current density significantly increases upon application of all interlayers, where the

obtained *J-V* curves of the devices with the various interlayers are all fairly similar. It should be noted that with the spin-coated interlayer of TmPyPB, a slightly lower electron current is obtained, which may be do suboptimal film formation. The results for an evaporated TmPyPB layer show that efficient electron injection is achievable also with this interlayer material. With both spin-coated an evaporated BCP, an even slightly higher current is observed compared to a TPBi interlayer. The current in reverse bias, corresponding to electron injection from the aluminum bottom electrode, also seems to be enhanced, potentially indicating diffusion of the small BCP molecules into the layer. However, this observation is not fully understood. Overall, the improved injected current by the application of organic interlayers with a low electron affinity indicates that this strategy can be generalized to more materials.

After having confirmed that the presented injection strategy is not limited to a single interlayer material, the following step is to substitute the organic semiconductor in which electrons are to be injected. To this end, the non-fullerene acceptor material 3,9-bis(2-methylene-((3-(1,1-dicyanomethylene)-6,7-difluoro)-indanone))-5,5,11,11-tetrakis(4-hexylphenyl)-dithieno[2,3-d:2',3'-d']-s-indaceno[1,2-b:5,6-b']dithiophene (IT-4F) is chosen, which finds application in efficient organic solar cells.[38] IT-4F, as opposed to the polymer PNDI(2OD)-2T is a small molecule, which is expected to render solution processing of the interlayer on top more challenging because of both mechanical properties and solubility. However, as displayed in Figure 5.8(c), the *J-V* curves of electron-only devices of IT-4F yield similar improvements upon application of either evaporated, or spin-coated interlayers. Moreover, also for IT-4F both TPBi and BCP interlayers give similar results, improving the injected electron current by about two orders of magnitude compared to a bare aluminum electrode. These measurements demonstrate that a tunneling interlayer may also improve the electron contact in solar cells based on non-fullerene acceptors, not requiring the use of instable reactive metals, while also being conveniently compatible with solution processing.

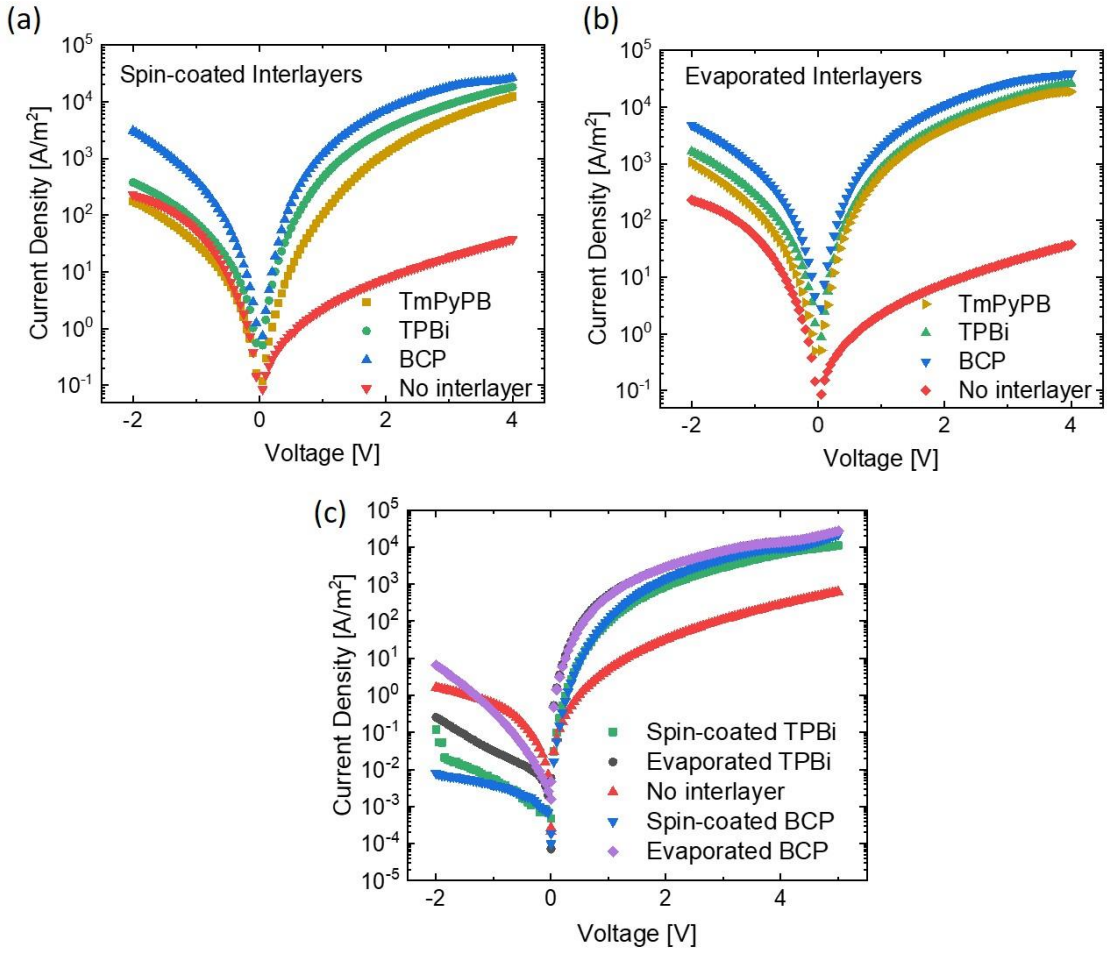

Figure 5.8. *J-V* characteristics of electron-only devices of PNDi(2OD)-T2 employing different interlayer materials applied by spin coating (a) or thermal evaporation (b). (c) *J-V* characteristics of electron-only devices of the organic semiconductor IT-4F with different interlayer materials and different deposition methods. In all cases, application of an interlayer substantially improves the injected electron current in IT-4F.

5.4. Conclusion

In summary, it has been shown that adding a thin organic tunneling interlayer can be used to obtain an ohmic electron contact on organic semiconductors. The main requirement for this interlayer is that the material has a lower electron affinity than the organic semiconductor in which the charge is injected. It was demonstrated that with the help of such an interlayer, ohmic electron injection can be achieved even from a plain aluminum electrode, whereas the conventional method of using low work function reactive metals without interlayers results in injection barriers. In addition, here is also shown that these interlayers can be solution processed on top of organic-semiconductor layers, as demonstrated for the polymer PNDI(2OD)-2T as well as for the non-fullerene acceptor IT-4F. These results show that the use of such interlayers results in superior electron injection compared to reactive metals and are even compatible with solution processing.

5.5. Experimental

Materials

All materials were used as received without further purification. Poly((N,N'-bis(2-octydodecy)naphthalene-1,4,5,8-bis(dicarboxoimide)-2,6-diyl)-alt-5,5'-(2,2'-bithiophene)) (PNDi(2OD)-T2), 2,2',2''-(1,3,5_Benzintiryl)-tris(1-phenyl-1-H-benzimidazole) (TPBi), Bathocuproine (BCP), 1,3,5-Tri(m-pyridin-3-ylphenyl)benzene (TmPyPB) and 3,9-bis(2-methylene-((3-(1,1-dicyanomethylene)-6,7-difluoro)-indanone))-5,5,11,11-tetrakis(4-hexylphenyl)-dithieno[2,3-d:2',3'-d']-s-indaceno[1,2-b:5,6-b']dithiophene (IT-4F) were purchased from Ossilia Ltd. Dried ethanol was purchased from Merck KGaA.

Device fabrication:

The organic semiconductors PNDI(2OD)-T2 and IT-4F were dissolved in chlorobenzene with a concentration of 10 mg/mL for PNDI(2OD)-T2 and 20 mg/mL for IT-4F respectively. The solutions were stirred for 18 hours at 60°C. The interlayer materials TPBi, BCP and TmPyPB were dissolved in dry ethanol with a concentration of 0.5 mg/mL each and stirred for 18 hours at room temperature. Glass substrates were washed with soap, followed by ultrasonic cleaning with acetone and isopropanol, and UV-ozone treatment. All subsequent device fabrication and electrical characterization steps were performed in controlled nitrogen atmosphere. A 30 nm aluminum bottom electrode was thermally evaporated in high vacuum at a base pressure of 1×10^{-6} mbar. The organic semiconductors were spin coated with a speed of 1000 rpm for 60 seconds followed by 30 seconds at 4000 rpm. The solution-processed interlayers were spin coated on top of the organic-semiconductor layers at 3000 rpm for 60 seconds. For the evaporated interlayers, thermal evaporation was carried out in high vacuum at a base pressure of 2×10^{-6} mbar. The devices were completed with a thermally evaporated aluminum top electrode with a thickness of 100 nm.

Device characterization:

All electrical measurements were performed inside a nitrogen-filled glovebox with a Keithley 2400 source meter. Layer thicknesses were measured with a DektakXT profilometer. AFM measurements were performed with a Dimension 3100® AFM.

6. Solution processing in OLEDs

In this chapter, the possibilities of solution processing for organic semiconductors used in OLEDs are elucidated. Currently, highly efficient OLEDs used in commercial applications as well as in academia are fabricated using thermal evaporation, with its drawbacks described in Chapter 2.5.1. To simplify the processability of OLEDs, they should be processed from solution. Here, in the first part of this chapter, solution processed single-layer OLEDs are explored. In the later part of this chapter, the focus will shift towards solution-processed stacking of multilayer systems for efficient solution-processed OLEDs.

6.1. Introduction

Solution processing of organic semiconductors remains a challenge in the field of OLED fabrication. Mostly due to the complex device design of state-of-the-art OLEDs, thermal evaporation has evolved as the leading method to fabricate high-efficiency OLEDs. To fabricate efficient OLEDs from solution, several challenges must be overcome.

As an initial approach, simplifying the device design to only one layer strongly facilitates the application of solution-processed techniques. For solution processing of multilayer OLEDs, each layer must be deposited on top of the underlying layer without causing damage. This presents challenges as the solvent used for the top layer may potentially dissolve the underlying layer. As discussed, the interfaces between different layers are critical for proper device functionality, and each additional layer deposited by solution increases the risk of causing device malfunction. Simplifying the device, particularly through the use of single-layer structures, eliminates the need for multiple layers, thereby reducing the risk associated with stacking multiple layers. Although single-layer devices have historically exhibited lower efficiency compared to multilayer structures, Kotadiya et al. demonstrated that the challenges in constructing efficient single-layer OLEDs can be overcome.[60] For such single-layer applications, the choice of emitter in the OLED must satisfy a range of requirements.[150]

One requirement for the emitter in single layer OLEDs is to exhibit balanced charge transport, where the mobility of both holes and electrons should be comparable. This balance is crucial for establishing a recombination zone in the middle of the emissive layer.[90] Locating the recombination zone in the center of the device is essential for optimizing OLED efficiency by minimizing loss processes attributed to surface plasmons, which can diminish outcoupling efficiency (for further details, refer to Section 2.3). Given that single-layer devices do not employ charge blocking layers, achieving this positioning of the recombination zone must be accomplished by the emitter itself.

Another essential requirement for a solution-processed emitter is its solubility and morphology post-processing. Ideally, an emitter should dissolve in the desired concentration to form a film upon processing. However, certain materials are insoluble in organic solvents. This insolubility can result in the aggregation of the organic semiconductor when attempts are made to dissolve it. This aggregation renders the solution opaque, making it unsuitable for film processing. Even if the film can be dissolved, indicated by a transparent solution,

challenges arise during the processing of the film itself. In organic semiconductors, the film's morphology plays a critical role in charge transport.[151] Intermolecular charge transport in such films relies on phenomena like π-π stacking, which necessitates the correct orientation of the organic semiconductor molecules within the film.[152] Solution processing methods involve a short film formation time, often referred to as a "freeze of solution." Consequently, the orientation of organic semiconductor molecules in the film becomes randomized. This randomization limits the number of molecules able to arrange themselves in an energetically favorable position, crucial for efficient charge transport. If the energetically favorable stacking cannot be achieved during solution processing, charge transport is compromised. Hence, optimization of deposition procedures is essential to maximize the probability of deposited organic semiconductor molecules forming the desired film structure.

In addition to the challenges posed by solution processing of a single film, there are other obstacles to overcome for fully solution-processing an OLED. Even for the single-layer OLED fabricated by Kotadiya et al., an interlayer was required for ohmic electron injection, as discussed in Chapter 5. These layers can be processed from solution on top of organic semiconducting polymers and molecules with long alkyl sidechains. However, for TADF emitters used in highly efficient OLEDs, these materials are neither polymers nor possess long alkyl side chains. Therefore, solution-processing them on top of such materials, especially using the spin-coating method, is likely to physically damage the film. To mitigate this issue, blending the organic semiconductor into a polymer matrix provides the underlying layer with more stability when a layer is solution-processed on top. Previous studies have demonstrated the successful blending of an organic semiconductor into a matrix of an insulating polymer, offering the additional benefit of trap dilution, which reduces the number of trap states in the organic semiconducting film. [120, 153, 154]

In this chapter, two approaches to develop a fully solution-processed OLED are explored. First, in Section 6.2, the investigation revolves around replicating the single-layer OLED design by solution-processing emitters suitable for this design. This aims to provide insights into the challenges of finding a suitable emitter for solution-processed single-layer OLEDs. In Section 6.3, the focus shifts to more traditional multilayer systems and approaches, aiming to solution-process a double-layer system with the dilution of the underlying layer in polystyrene (PS). Such systems with two layers help to fix the recombination zone within a device, eliminating the need for an emitter with balanced charge transport and therefore allowing for a wider range of emitters in exchange with a more complex device structure.

6.2. The way towards solution-processed single-layer OLEDs

In this section, the options of solution processing single-layer OLEDs are investigated. This is carried out using the well-known TADF emitter CzDBA and its tert-butyl substituted variant. In Subsection 6.2.2, several dimethylacridine (DMAC) derivatives are explored for their potential use in single-layer OLED devices.

6.2.1. CzDBA and derivates in solution processed applications

The simplest approach to create a solution-processed single-layer OLED is to replicate a well-established evaporated system using solution-based methods. Therefore, CzDBA is chosen as the emitter, with its molecular structure depicted in black in Figure 6.1(c). CzDBA meets all the requirements for an emitter suitable for a single-layer OLED. It demonstrates balanced charge transport and can be considered trap-free.[78] Single-layer devices made with this emitter have previously exhibited EQEs up to 19 %.[60]. However, adopting this system for a solution-processed OLED is unfortunately not feasible. It has been found that CzDBA cannot be dissolved in a solvent, as evidenced by the milky solution shown in Figure 6.1(a). This indicates that CzDBA forms aggregates instead of being fully dissolved. Such a solution does not form a uniform film upon spin-coating, as depicted in Figure 6.1(b). Even variations in solvent and heating the solvent did not improve the solubility of CzDBA.

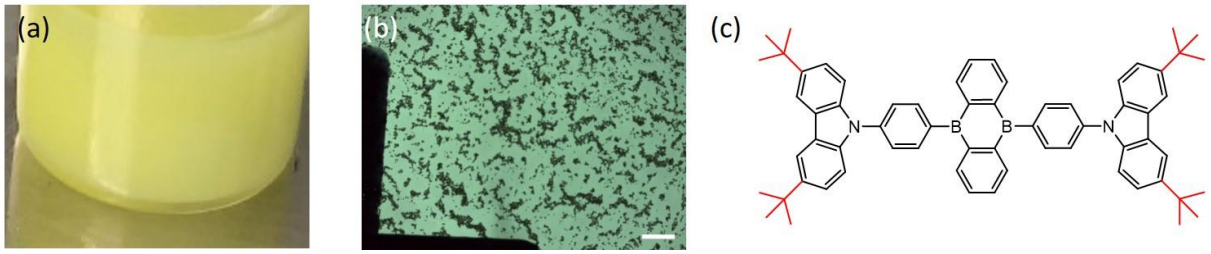

Figure 6.1. (a) Photography of CzDBA aggregate in a toluene solution. (b) Light microscopy image of CzDBA solution processed on top a glass substrate. The scale is 200 µm. (c) Molecular structure of CzDBA (black) and tBuCzDBA (black structure with red tertbutyl side chains).

To overcome the limitations of dissolving CzDBA, tert-butyl-substituted CzDBA (tBuCzDBA) is utilized as the emitting layer.[155, 156] The molecular structure of this compound is depicted in Figure 6.1(c), which consists of the black-displayed structure of CzDBA with the addition of four red-displayed tert-butyl groups. These alkyl groups render tBuCzDBA soluble in a variety of organic solvents, such as toluene, which is used in this study to dissolve tBuCzDBA. Similar to CzDBA, tBuCzDBA also exhibits thermally activated delayed fluorescence (TADF) properties, with two carbazole donor moieties and a central boron-substituted anthracene derivative as the acceptor.

The solution containing tBuCzDBA in chlorobenzene exhibits no signs of aggregation, appearing clear. Consequently, a film can be spin-coated from this solution. Similar to CzDBA, to facilitate charge injection for the formation of an ohmic contact, an interlayer, as discussed in Chapter 5, is required to be deposited atop the tBuCzDBA layer. To protect the tBuCzDBA layer from the effects of ethanol used for the interlayer, tBuCzDBA is blended with polystyrene (PS) in a 50 % (w/w) ratio. The inclusion of PS aims to offer a stable matrix for tBuCzDBA, safeguarding it from the effects of the solvent utilized to process the interlayer atop.

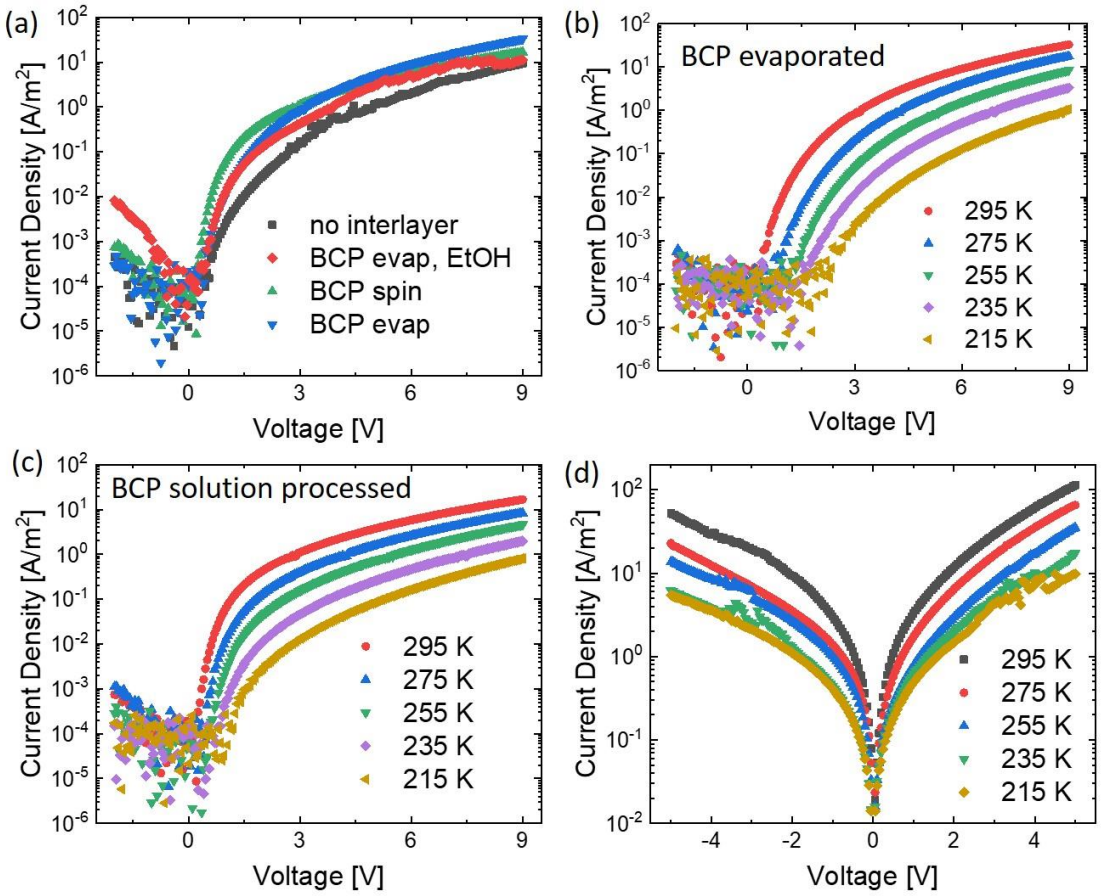

Figure 6.2. (a) J-V characteristics measured at 295K for EO devices made of a tBuCzDBA-PS blend with a 50 % (w/w) amount of PS and a layer thickness of 127 nm. The device structure is Al/tBuCzDBA-PS/interlayer/Ba/Al. The black symbols show the device without use of an interlayer, red the use of evaporated BCP after treatment of the film with EtOH, green the solution deposition of BCP from ethanol solvent and blue as reference the device with the evaporated BCP layer. (b) Here, the temperature dependent J-V characteristic of an EO device of tBuCzDBA-PS blend with an evaporated BCP layer is shown. (c) Temperature dependent J-V characteristic for an EO device of tBuCzDBA-PS blend with a solution processed BCP layer. (d) Temperature dependent HO device of the tBuCZDBA-PS blend with the device structure ITO/PEDOT-PFI/tBuCzDBA/MoO_3/Al.

From the blend of tBuCzDBA with PS, EO devices were fabricated, and their J-V characteristics are illustrated in Figure 6.2. The comparison in Figure 6.2(a) delineates the impact of the interlayer on device performance. Notably, the results indicate that the addition of PS yields a functional device, as evidenced by the typical behavior observed in EO devices. Comparing the black curve without an interlayer to the blue curve with the evaporated interlayer, an increase in current density is apparent, suggesting that the interlayer addition facilitates the formation of an ohmic electron contact, as discussed in Chapter 5. In experiments aiming to deposit the interlayer from solution rather than by evaporation, the influence of EtOH was first tested, as depicted by the red curve in Figure 6.2(a). Only minor differences compared to the blue curve of evaporated BCP without EtOH treatment were observed, indicating that the effect of EtOH on the film is negligible. Subsequently, the green curve of the solution-processed BCP confirms that this interlayer can be processed from solution atop the tBuCzDBA-PS blend, while achieving an ohmic contact comparable to that with evaporated BCP. This conclusion is further supported by the temperature-dependent J-V curves illustrated

in Figure 6.2(b) for the evaporated BCP interlayer and in Figure 6.2(c) for the solution-processed BCP interlayer, respectively. A comparison between these two curves reveals no significant differences, neither in the absolute values of the current density nor in the temperature dependence of the current density. These results affirm that the interlayer strategy presents a viable option for achieving an ohmic electron contact, not only for CzDBA but also for tBuCzDBA.

To fabricate a fully solution-processed single-layer OLED using tBuCzDBA blended with PS, achieving ohmic hole injection is essential. Typically used PEDOT:PSS does not provide an ohmic hole contact. However, doping PEDOT:PSS with 2-[1-[difluoro-[(trifluoroethenyl)oxy]methyl]-1,2,2,2-tetrafluoroethoxy]-1,1,2,2,-tetrafluorosulfonic acid, commonly known as Nafion, can further reduce the injection barrier and enable an ohmic contact, even for materials with a deep HOMO [157]. Therefore, a device was fabricated using ITO and PEDOT:PSS doped with Nafion for hole injection, tBuCzDBA doped with PS as the emissive layer, and a BCP interlayer for ohmic electron contact, all covered with an Al electrode. The resulting current density, luminance, and EQE curves are plotted in Figure 6.3.

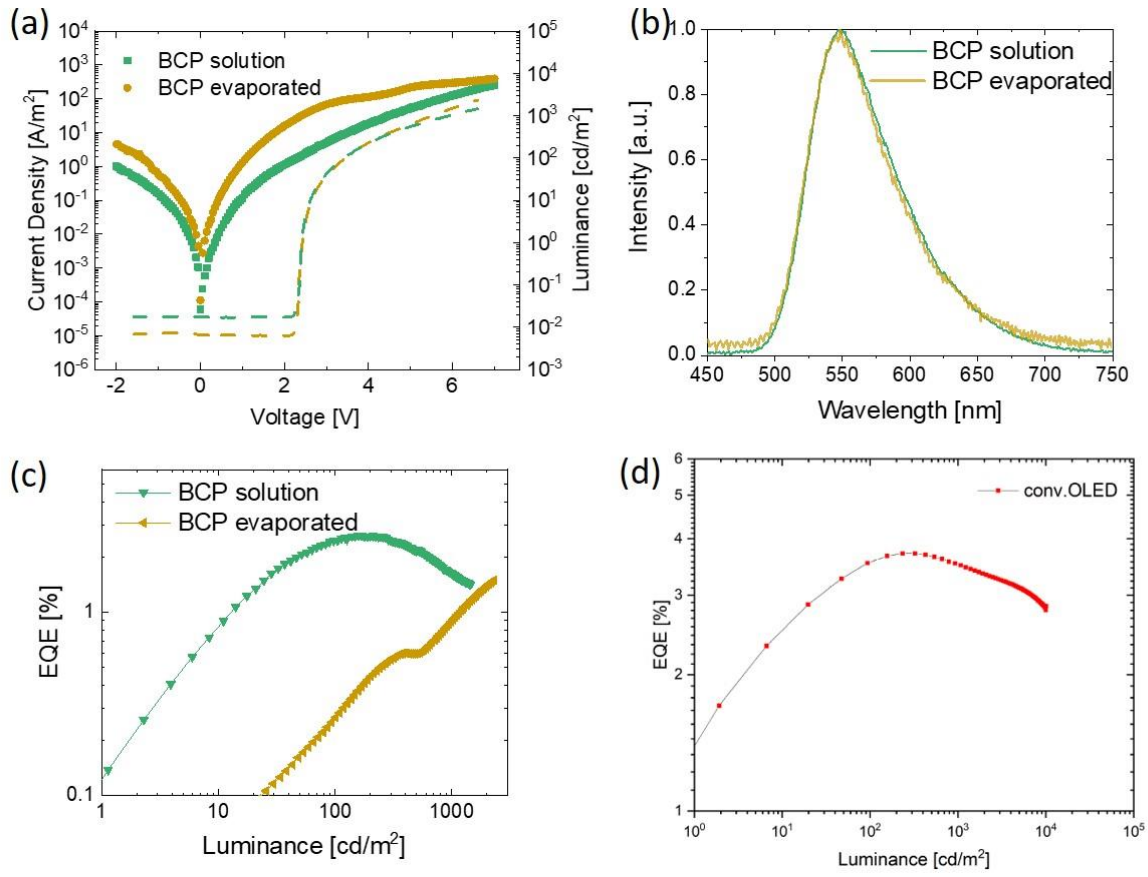

Figure 6.3. (a) Current density and luminance of a single layer OLED made of tBuCzDBA blended with 50 % (w/w) ratio of PS. The device structure is ITO/PEDOT-PFI/tBuCzDBA-PS/BCP/Ba/Al. Green shows a solution processed BCP-layer while ocher represents an evaporated BCP-layer. Filled symbols represent the current density while the dashed line represents the photocurrent density. (b) Electroluminescence spectra of the OLEDs described in Figure 6.3(a). (c) Resulting EQE versus luminance plots for the OLEDs described in Figure 6.3(a). (d) Reference EQE-plot for a fully evaporated single layer tBuCzDBA OLED from [158].

From the J-V curve, depicted by the filled symbols in Figure 6.3(a), a deviation from the typical OLED curve can be observed due to the high leakage current in the device, which suppresses the distinct area of the diffusion current, making the built-in voltage challenging to extract from this plot. However, for the different methods of interlayer deposition, namely evaporated (ocher) and solution processed (green), a higher leakage current is observed for the evaporated method, although both achieve the same values at 7V. In contrast, the luminance curve, shown by the dashed line in Figure 6.3(a) exhibits the expected behavior, with no discernible differences between the two interlayer deposition methods. The electroluminescence (EL) spectra provided in Figure 6.3(b) indicate that the deposition method of the interlayer does not affect the electroluminescence, as both curves overlap. The measured maximum of the EL spectra at 549 nm for the tBuCzDBA:PS blends aligns with the values reported for neat films of tBuCzDBA ranging from 546 to 553 nm, suggesting that the blending of an emitter with PS did not influence the performance of the emitter [159]. From the current density, photocurrent density, and EL spectra, the EQE can be determined. The resulting EQE versus luminance plot is shown in Figure 6.3(c). Notably, for the OLED with the solution processed BCP layer, a maximum EQE of 3.5 % is attained, whereas for the evaporated BCP layer, the EQE reaches only 1.5 %, which is probably due to the higher leakage current. These recorded values are in line with the measured 4 % EQE for the fully evaporated system, as reported by Mahni Fatahi, shown in Figure 6.3(d).[158]

The measured EQE-values are significantly lower than those obtained for CzDBA, even with a comparable device structure. The reason for the significantly lower efficiency lies in the imbalanced charge transport exhibited by tBuCzDBA. A comparison between the electron and hole currents displayed in Figure 6.2 reveals, that the hole current of tBuCzDBA doped with PS is approximately on order of magnitude larger than the respective electron current. This is in line with previous results obtained by Mahni Fatahi. He determined for pure tBuCzDBA an electron mobility of $2.3 \cdot 10^{-10}$ $m^2(Vs)^{-1}$ and a hole mobility of $1.8 \cdot 10^{-9}$ $m^2(Vs)^{-1}$.[158] It is still under investigation why the addition of the four tertbutyl groups to CzDBA has such a significant influence on charge transport, as they theoretically should not affect the donor or acceptor moieties. However, as observed, the EQE of this single-layer TADF-OLED is significantly lower than that of a CzDBA OLED or even multilayer OLEDs. Nevertheless, the experiments serve as a proof of principle that the PS doping of a TADF emitter did not diminish the efficiency compared to the pure and evaporated material. Additionally, it is demonstrated that the application of the solution-processed interlayer is successfully implemented in OLED fabrication.

6.2.2. DMAC-Derivates for solution processing

Due to the previously discussed limitations of CzDBA and tBuCzDBA, investigations into other emitters suitable for application in single-layer OLEDs were initiated. In this subsection, the focus is on emitters that utilize a dimetylacridin (DMAC) group as donor moieties of a TADF molecule. The first molecule in this series tested is bis[4-(9,9-dimethyl-9,10-dihydroacridine)phenyl]methanone (DMAC-BP). This green-emitting TADF molecule features a benzophenone acceptor unit coupled with two DMAC donors. The molecular structure of this molecule is displayed in Figure 6.4 (left). DMAC-BP garnered interest in this study due to

its high PLQY and bipolar charge transfer properties. Its high PLQY allows it to be utilized in OLEDs as an emissive layer without the need for other dopants.[160] The suitability of this molecule as a TADF emitter arises from its short conjugation length with the donor and acceptor moieties, leading to a high triplet energy and therefore a small singlet-triplet energy gap of approximately 0.07 eV.[161]

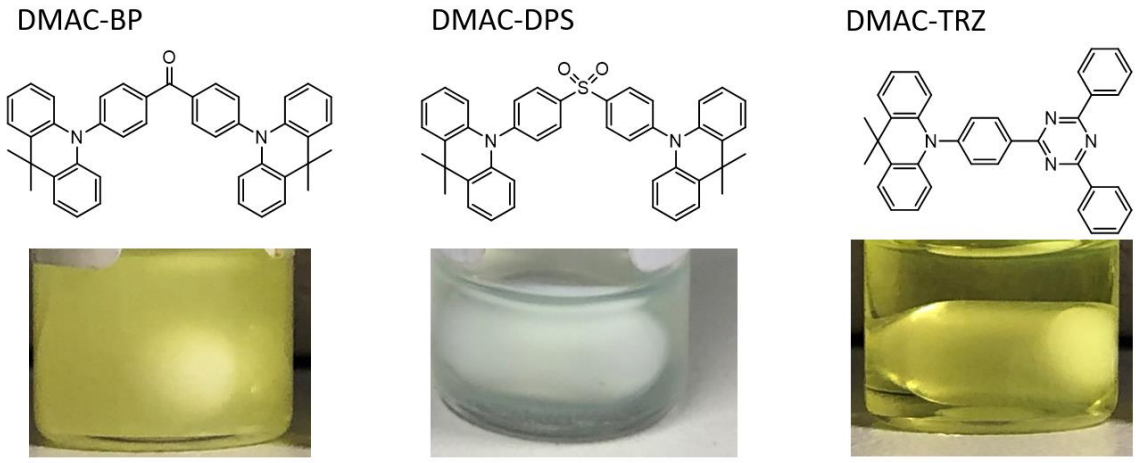

Figure 6.4. Left: molecular structure and solution of DMAC-BP in chlorobenzene. Middle. Molecular structure and solution of DMAC-DPS in chlorobenzene. Right. Molecular structure and solution of DMAC-TRZ in chlorobenzene.

Upon attempting to dissolve DMAC-BP, difficulties arose. Similar to CzDBA, the experiments to dissolve DMAC-BP in organic solvents resulted in an opaque solution. An example of such behavior is illustrated in Figure 6.4 (left), which depicts a photograph of a solution of DMAC-BP in chlorobenzene. It is noteworthy that the white coloration in the middle of the picture arises from the stirring bar. The insolubility of DMAC-BP renders it unsuitable for application in solution-processed OLEDs.

To further investigate and identify a suitable emitter for solution processing, a slight modification was made to the emitter utilized. Instead of the benzophenone acceptor of DMAC-BP, sulfonyldibenze was employed as the acceptor unit in 10,10'-(4,4'-Sulfonylbis(4,1-phenylene))bis(9,9-dimethyl-9,10-dihydroacridine (DMAC-DPS). The molecular structure of this material is depicted in Figure 6.4 (middle). Unlike DMAC-BP, DMAC-DPS emits blue light. Similar to DMAC-BP, DMAC-DPS also exhibits a high PLQY and can be utilized as an undoped emissive layer.[162] In contrast to DMAC-BP, DMAC-DPS is soluble in organic solvents, as evidenced by the transparent solution obtained upon dissolving DMAC-DPS in chlorobenzene, as shown in Figure 6.4 (middle).

A third TADF emitter utilizing a DMAC-donor moiety is examined in this study. This compound, 10-(4-(4,6-Diphenyl-1,3,5-triazin-2-yl)phenyl)-9,9-dimethyl-9,10-dihydroacridine (DMAC-TRZ), employs 2,4,6-triphenyl-1,3,5-triazine as the acceptor moiety. Similar to DMAC-DPS, DMAC-TRZ emits blue light and can serve as an emitter in an undoped emissive layer to fabricate an efficient OLED.[163] Additionally, it has been reported that DMAC-TRZ is expected to exhibit balanced charge transport, fulfilling another requirement for a single layer OLED.[164]

The solution prepared from DMAC-TRZ in chlorobenzene is transparent, as depicted in Figure 6.4 (right), rendering DMAC-TRZ a promising candidate for solution processing.

Out of the three tested candidates, only two, DMAC-DPS and DMAC-TRZ, provided clear solutions. They were employed in an initial experiment to fabricate EO devices from solution and compared to EO devices with evaporated organic semiconductor layer to assess the performance of the solution-processed film relative to the evaporated one. The resulting temperature-dependent J-V characteristics are depicted in Figure 6.5.

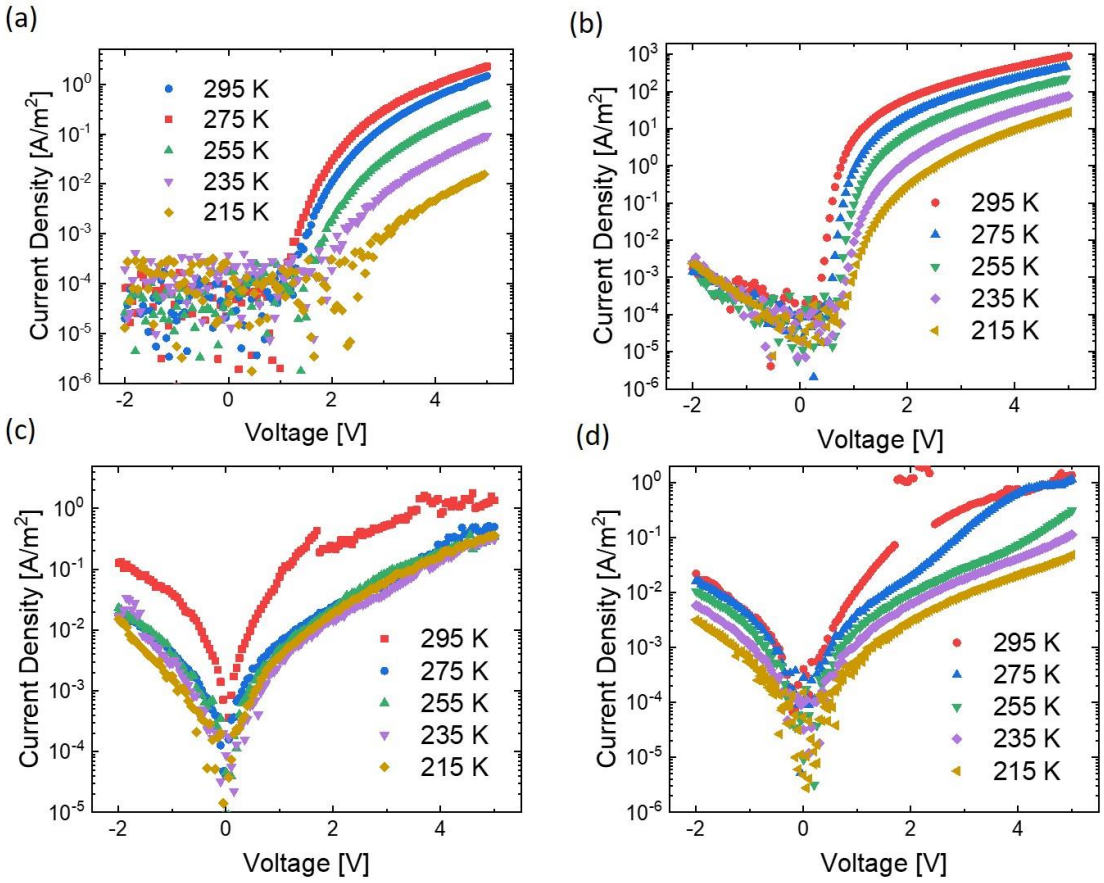

Figure 6.5. J-V curves of temperature dependent EO-devices of DMAC-DPS and DMAC-TRZ with different deposition methods and the device structure Al/active layer/TPBi/Ba/Al. (a) DMAC-DPS evaporated. (b) DMAC-TRZ evaporated. (c) DMAC-DPS solution processed. (d) DMAC-TRZ solution processed.

For the evaporated DMAC-DPS, a typical temperature-dependent J-V curve is recorded, as displayed in Figure 6.5(a). It exhibits the anticipated trend of decreasing current with decreasing temperature, consistent with behavior expected for organic semiconductors. The significant decrease in current density between 295K and 215K, spanning three orders of magnitude, indicates substantial energetic disorder. Similarly, for an EO device made of evaporated DMAC-TRZ, a decrease in current density with decreasing temperature is observed, as shown in Figure 6.5(b). It is notable that a high electron current is observed for DMAC-TRZ.

When attempting solution processing of both TADF materials, issues arise. For the EO of solution-processed DMAC-DPS, the *J-V* curves displayed in Figure 6.5(c) exhibit no

temperature dependence. Consequently, the measured current likely results from leakage current rather than organic semiconducting behavior of DMAC-DPS. For the EO J-V curves of solution-processed DMAC-TRZ, displayed in Figure 6.5(d), a temperature dependence is observed. However, the measured current density is three orders of magnitude lower than for the EO with evaporated DMAC-TRZ. It is assumed that the rapid film formation using the solution deposition method leads to poor molecular arrangement within the film, thereby reducing conductivity. This is further confirmed by the HO-devices for both materials as displayed in Figure 6.6. Here, the same differences in the temperature dependence between solution processed and evaporated materials are observed. In Figure 6.6(a and b) the temperature dependent *J-V* characteristic for the evaporated materials show the typical temperature dependent behavior. For the devices with the solution processed DMAC-layer, the temperature dependent *J-V* characteristic displayed in Figure 6.6(c and d) show the absence of the temperature dependence, indicating a current dominated by leakage current.

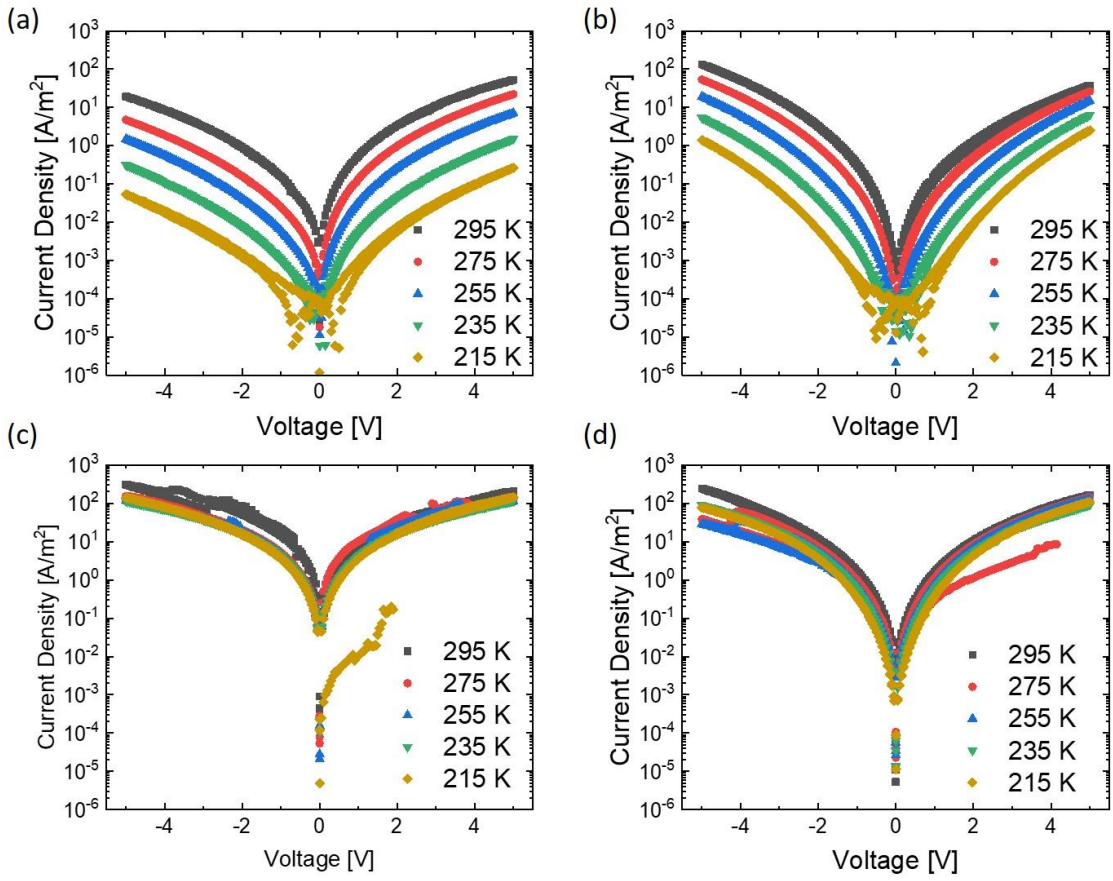

Figure 6.6. J-V curves of temperature dependent HO-devices of DMAC-DPS and DMAC-TRZ with different deposition methods and the device structure ITO/PEDOT:PSS/active layer/MoO_3/Al. (a) DMAC-DPS evaporated. (b) DMAC-TRZ evaporated. (c) DMAC-DPS solution processed. (d) DMAC-TRZ solution processed.

In this section, it has been demonstrated that numerous challenges persist in creating a single-layer device from solution. The stringent requirements imposed on the emitter reduce the pool of available candidates significantly. Even minor structural modifications aimed at enhancing solubility could render an emitter unsuitable for an efficient OLED. Furthermore, it has been illustrated that the morphology of solution-processed films can differ from

evaporated ones, presenting additional hurdles for solution processing to achieve a suitable morphology of the used materials to achieve good organic semiconducting properties from solution processed organic semiconductors.

6.3. Double layer OLEDs

Due to the challenges posed by the emitters in fabricating a single-layer OLED from solution, the focus shifts to fabricating double-layer OLEDs from solution. To stack multiple layers on top of each other, the application of the orthogonal solvent method is necessary.[165] This method utilizes different solvents, which are either hydrophilic or hydrophobic. Some materials, especially polymers, are insoluble in hydrophilic solvents but can be deposited from hydrophobic solvents. Then, the second layer can be deposited from a hydrophilic solvent, analogous to the interlayer deposition discussed in Chapter 5. Another requirement for stacking several layers from solution on top of each other is to make the underlying layer stable against the forces introduced by solution processing the top layer. This can be achieved by blending the underlying layer into a polymer matrix. Polymers have the advantage, due to their high molar mass, of being stable against the physical forces arising from solution processing the top layer and therefore protect the underlying organic semiconductor inside the polymer matrix.

The challenges for creating such a multilayer system include finding a solution-processable emitter that can be blended with a polymer to form a stable underlying layer. Ideally, this blend should not compromise the performance of the organic semiconductor. Additionally, the solvent used for the top layer should ideally not affect the underlying layer. Moreover, the second layer of the OLED, which should serve as a HBL or an ETL, needs to be processed from a hydrophilic solvent while maintaining its desired properties.

This device structure is examined using two different emitter compounds. First, in Subsection 6.3.1, 2,3,4,6-Tetra(9H-carbazol-9-yl)-5-fluorobenzonitrile (4CzFCN) is utilized as the test emitter, followed by Subsection 6.3.2, which explores the use of 2,6-di(9H-carbazol-9-yl)-3,5-bis(3,6-di-tert-butyl-9H-carbazol-9-yl)benzonitrile (2tCz2CzBN) as the emitter. For both of these emitters, the feasibility of solution processing, blending with an insulating polymer, and the ability to deposit the second layer on top of the underlying emissive layer are investigated.

6.3.1. 4CzFCN in solution processed applications

In this subsection, the emitter 4CzFCN was selected as the test candidate for the proposed double-layer solution-processed OLED system. This emitter, as depicted in Figure 6.8(b), comprises four carbazole donor moieties connected to a central phenyl-ring, which is further substituted with a nitrile and a fluorine group to act as an acceptor. This molecule is reported to be solution-processable and demonstrates good TADF performance.[166]

A preliminary assessment of the performance of 4CzFCN was conducted by fabricating EO-devices using this material. These devices were prepared in various configurations, including with and without an interlayer to assess its impact on electron injection. Additionally, the feasibility of creating a blend of 4CzFCN with PS using chlorobenzene as solvent was examined,

along with its influence on device performance. Finally, the effect of ethanol on subsequent solution processing experiments was investigated. Here, ethanol serves as hydrophilic solvent, which should not influence the underlying layer. For all these devices, the current density was measured at different temperatures to analyze charge transport characteristics, as depicted in Figure 6.7.

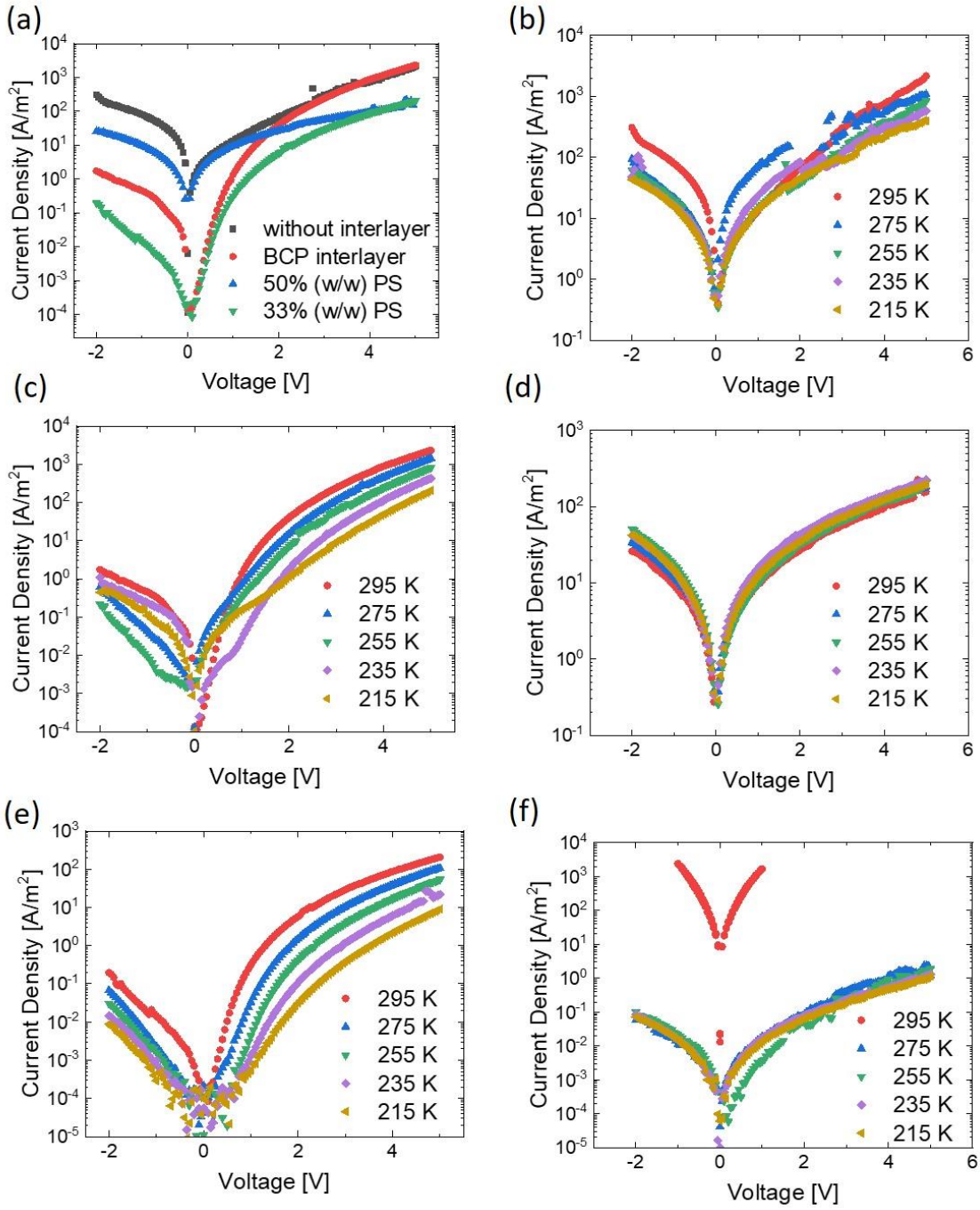

Figure 6.7. Different J-V characteristic of EO-devices made of 4CzFCN with and without interlayer and blends with PS. The device structure for all devices is Al/4CzFCN/interlayer/Ba/Al. (a) Comparison of J-V diagrams of EOs measured at 295K of 4CzFCN with (red) and without (black) interlayer as well as 50 % (w/w) PS blend (blue) and 33 % (w/w) PS blend (green) both with BCP interlayer. Here, the layer thicknesses for the different films a determined to be 35 nm for the pure 4CzFCN, 55 m for the 50 % (w/w) PS blend and 51 nm (w/w) for the 33 % (w/w) PS blend. (b) Temperature dependent J-V characteristic of an EO device of 4CzFCN without BCP interlayer. (c) Temperature dependent J-V curve of an EO device made of 4CzFCN with an evaporated BCP interlayer. (d)

Temperature dependent J-V curve of an EO device made of 4CzFCN with 50 % (w/w) of PS with an evaporated BCP interlayer. (e) Temperature dependent J-V curve of an EO device of 4CzFCN with 33 % (w/w) of PS with an evaporated BCP interlayer. (f) Temperature dependent J-V curve of an EO device of 4CzFCN with 33 % (w/w) of PS with a solution processed BCP interlayer.

In Figure 6.7(a), the J-V curves of several devices were compared at 295 K. A device without an interlayer, depicted in black, exhibited a high leakage current in the low voltage region compared to a device with an interlayer, shown in red. When comparing the temperature-dependent J-V scans, as illustrated for the device without an interlayer in Figure 6.7(b) and with an interlayer in Figure 6.7(c), it becomes evident that the device without the interlayer shows a lower temperature dependence, indicating a higher leakage current. This is further supported by the high current density observed in the low voltage regime. Conversely, the EO-device with the interlayer, as depicted in Figure 6.7(c), demonstrates that a solution-processed neat film of 4CzFCN with an interlayer yields an organic semiconducting device that behaves as expected.

For further investigations, it is necessary to solution process on top of the 4CzFCN layer from solution. However, as the neat film of 4CzFCN is expected to be damaged upon solution processing on top of it, it is imperative to embed the 4CzFCN in a polymer matrix to ensure a stable film during solution processing. Therefore, the influence of PS blending on the charge transport characteristics was tested. A PS with a molar mass of m = 2375 g mol^{-1} was utilized for these experiments. In a preliminary test, an EO-device was fabricated using a blend with 50 % (w/w) of PS. The resulting J-V curve, displayed in Figure 6.7(d), shows an absence of temperature dependence. This suggests that with the high amount of PS, the organic semiconducting behavior of the 4CzFCN is suppressed, due to the high leakage currents occurring with the high amount of PS.

Subsequently, a second test was conducted with a lower amount of only 33 % (w/w) of PS. The resulting temperature-dependent J-V curves, depicted in Figure 6.7(e), indicate that in this case, the semiconducting behavior is retained, as a decrease in current density with a decrease in temperature is observed. Also, from Figure 6.7(a), a comparison between the neat film of 4CzFCN with the BCP interlayer (red) and the 33 % (w/w) PS blend (green) reveals that both curves exhibit the same shape, with the current density for the blend being one order of magnitude lower compared to the neat film. This decrease in current density is expected due to the lower amount of hopping sites in the PS-blended film. Additionally, the decrease in current density for the 33 % (w/w) PS blend compared to the neat film while decreasing the temperature is comparable (see Figure 6.7(c) for the neat film and Figure 6.7(e) for the 33 % (w/w) PS blend). This result shows that a dilution of 33% (w/w) of PS within a 4CzFCN film does not diminish the charge transport in 4CzFCN.

To gain further insights into the stability of the PS-blended film against solvents like ethanol, attempts were made to process the interlayer from solution, as described in Chapter 5. However, Figure 6.7(f) reveals that for the 33 % (w/w) blend, which worked with the evaporated interlayer, the solution processing led to a leakage current-dominated device. This is evident from the absence of temperature dependence in the current density curves. These initial experiments demonstrate the potential of solution processing 4CzFCN but also highlight

challenges associated with blending the film with PS and solution processing on top of this films.

After testing the solution processability of 4CzFCN, the focus shifts towards OLEDs. Figure 6.8(a) illustrates a sketch of the OLED, along with the structural formulas of the organic semiconductors used in the OLED (Figure 6.8(b-d)).

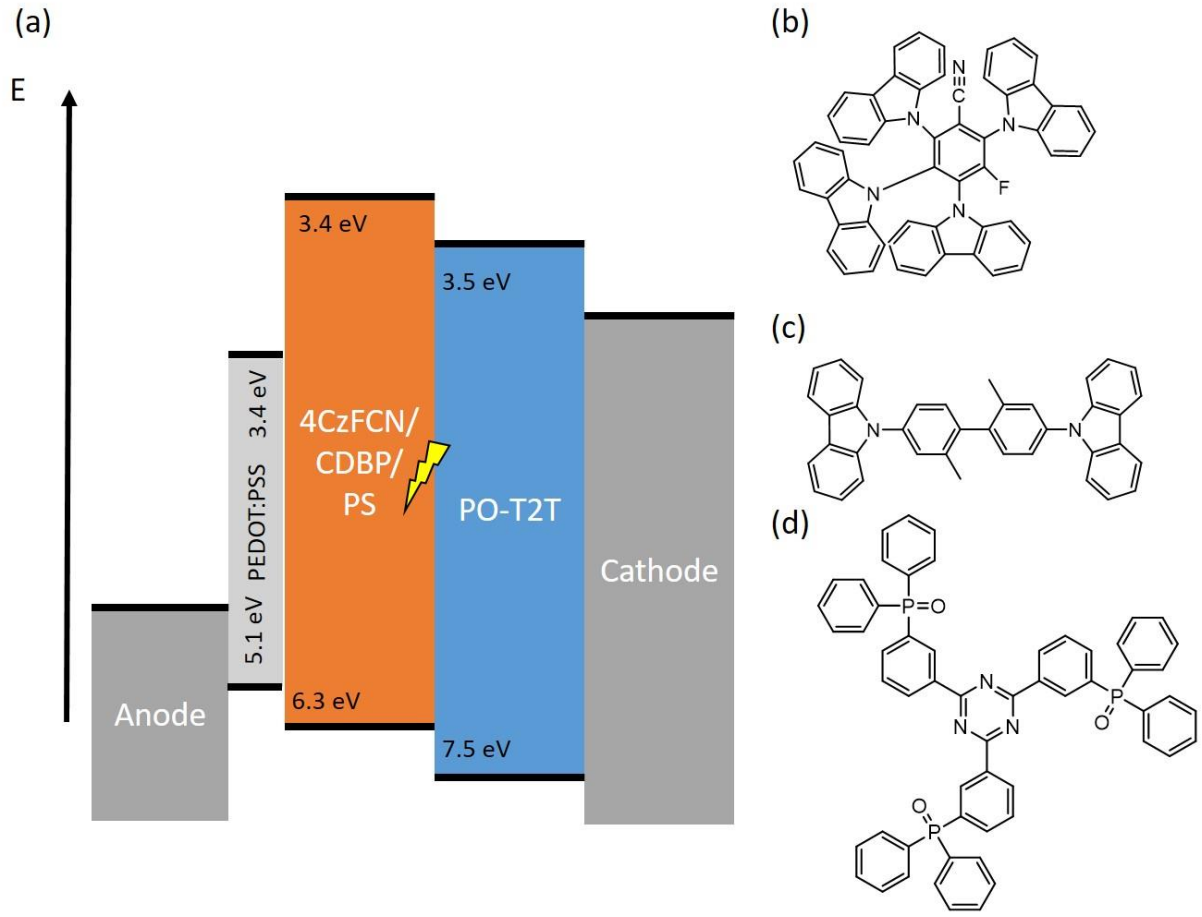

Figure 6.8. (a) Sketch of the double layer device fabricated in this Subsection. (b) Molecular structure of 4CzFCN. (c) Molecular structure of CDBP. (d) Molecular structure of PO-T2T.

As 4CzFCN does not exhibit balanced charge transport, it is necessary to add another layer to prevent the recombination of the charges and the decay of the excitons near the metal cathode to prevent loss processes like surface plasmons.[167, 168] Therefore, a layer of 2,4,6-Tris[3-(diphenylphosphinyl)phenyl]-1,3,5-triazine (PO-T2T) is inserted between the cathode and the 4CzFCN. PO-T2T is known as an ETL and HBL material, and its molecular structure is shown in Figure 6.8(d).[169] The effect of PO-T2T is to shift the recombination zone to the interface between the 4CzFCN and the PO-T2T. Due to the energy levels of PO-T2T, the holes, injected from the anode, cannot travel through the PO-T2T layer to the cathode. However, the electrons injected from the cathode can travel through the PO-T2T layer. Therefore, the first time holes and electrons meet and can recombine is at the interface of PO-T2T and 4CzFCN. Since the layer of PO-T2T is thick, around 50 nm, the recombination zone is far away from the metallic cathode, hindering the emergence of surface plasmons.

A further necessity to fabricate OLEDs from 4CzFCN is the introduction of a host material that is blended together with the 4CzFCN. Therefore, 4,4'-Bis(9-carbazolyl)-2,2'-dimethylbiphenyl (CDBP) is used as the host material, whose molecular structure is displayed in Figure 6.8(c). This host is necessary to prevent loss processes like self-quenching of the triplet excited state of the emitter.[170] Such self-quenching could occur when the excited triplet state of two excited molecules interact with each other in a process called triplet-triplet annihilation (TTA).[171] The used host material CDBP acts as a spacer between the emitter molecules inside the emissive film. The molecular design of this host material, especially through the two methyl groups at the phenyl rings, which introduce a steric twisting to the molecules, leads to a high triplet energy.[172] This high triplet energy helps to suppress loss processes like TTA. Another advantage of using a host for 4CzFCN is the minimization of the formation of dimers from 4CzFCN, which could introduce other loss processes.[173]

To assess the impact of the PO-T2T layer on OLED performance, OLEDs were fabricated and compared with and without the presence of an evaporated PO-T2T layer. Additionally, an OLED with only a thin TPBi interlayer was included for comparison. The emissive layer of these OLEDs comprised 75 % (w/w) CDBP blended with 25 % (w/w) of 4CzFCN. The resultant OLED characteristics are depicted in Figure 6.9.

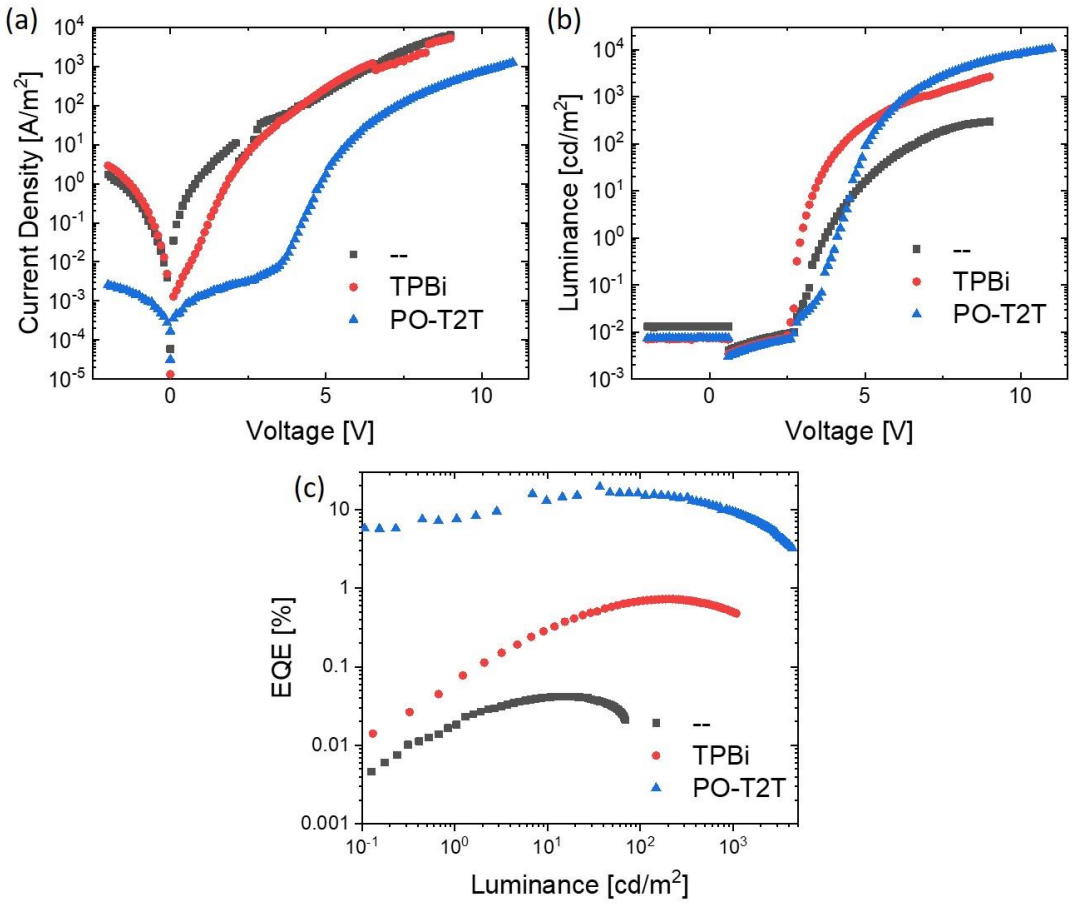

Figure 6.9. OLED performance of 4CzFCN:CDBP as emissive layer without (black), TPBi interlayer (red) or PO-T2T layer (blue) as second layer. The device structure is ITO/PEDOT:PSS/PVK/4CzFCN:CDBP/(inter)layer/LiF/Al. (a) J-V diagrams of the before mentioned OLEDs. (b) Luminance versus voltage of before mentioned OLEDs. (c) EQE versus luminance of before mentioned OLEDs.

As depicted in Figure 6.9(a), OLEDs without any second layer (black) or with a thin TPBi interlayer (red) exhibit high leakage currents in the low voltage regime, lacking the expected distinct shape of a typical J-V curve for OLEDs. However, with the insertion of the PO-T2T layer (blue), the J-V curve assumes the expected shape characteristic of OLEDs. In Figure 6.9(b), the luminance is noticeably low without an interlayer compared to OLEDs with an interlayer or a PO-T2T layer. Consequently, the resulting EQE is lowest without any interlayer, approximately 0.02 %. With the inclusion of a TPBi interlayer, there is a significant increase in EQE to around 1 %. The highest EQE is achieved with the PO-T2T interlayer, reaching a maximum of 19 %. This result underscores the necessity of employing a second layer for achieving efficient OLEDs utilizing 4CzFCN and CDBP in the emissive layer.

In the subsequent investigation, the potential for diluting the emissive layer containing 4CzFCN and CDBP in PS while maintaining its efficiency was explored. OLEDs were fabricated with the active layer consisting of 33 % (w/w) of PS (Figure 6.10(a)) or 50 % of PS (Figure 6.10(b)). The ratio of 4CzFCN to CDBP was kept constant, mirroring previous experiments. Additionally, a comparison was made to assess the film's resilience to solution processing of the second layer, with the PO-T2T layer either solution processed or evaporated on top of the emissive layer blended with PS. The resulting device characteristics are depicted in Figure 6.10.

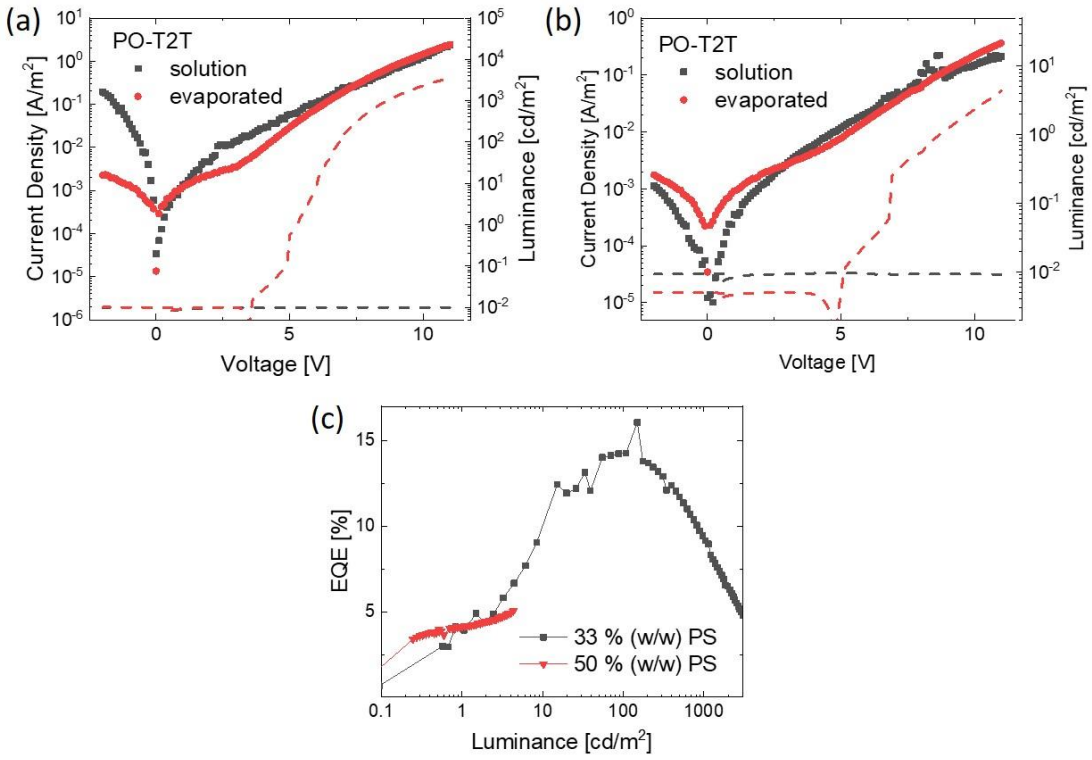

Figure 6.10. (a) Current density (solid symbols) and luminance (dashed lines) versus voltage plots of OLEDs with an emissive layer of 4CzFCN and CDBP in a matrix of 33 % (w/w) of PS. The device structure was ITO/PEDOT-PSS/4CzFCN:CDBP:PS/PO-T2T/LiF/Al. PO-T2T was either solution processed (black) or evaporated (red). (b) Current density (solid symbols) and luminance (dashed lines) versus voltage plots of OLEDs with an emissive layer of 4CzFCN and CDBP in a matrix of 50 % (w/w) of PS. PO-T2T was either solution processed (black) or evaporated (red). (c) EQE versus luminance plots for the OLEDs with evaporated PO-T2T layer and either 33 % (w/w) PS (black) or 50 % (w/w) PS (red).

In Figure 6.10(a), for the blend with 33 % (w/w) of PS, it is evident that the J-V curve of 4CzFCN with CDBP and PS, followed by evaporated PO-T2T (red, filled symbols), exhibits the anticipated shape, albeit with an overall reduced current density compared to devices without PS (see Figure 6.9(a), blue curve). Although the luminance (red, dashed line) is diminished with the addition of PS compared to the film without PS, the curve's shape remains consistent. In Figure 6.10(c), the resulting EQE for this OLED is plotted (black curve), revealing a maximum EQE of 15 %. This is slightly lower than observed without the addition of PS to the active layer. Conversely, when the PO-T2T layer is solution processed (Figure 6.10(a), black, filled symbols), the resulting J-V curve is dominated by leakage current, and the typical shape of an OLED J-V curve is not evident. Moreover, no luminance can be recorded (black, dashed line), leading to an inability to determine EQE. It is hypothesized that the low amount of PS causes damage to the underlying emissive layer during the solution processing of the PO-T2T layer, resulting in an OLED that does not function as expected.

Increasing the amount of PS to 50 % (w/w) in the emissive layer aimed to enhance its resistance to solution processing. However, the resulting J-V curves in Figure 6.10(b) for evaporated PO-T2T (red, filled symbols) show that the OLED is now dominated by leakage current, with the three distinct regimes no longer observable. Additionally, the luminance (red, dashed line) is further reduced compared to the OLED with only 33 % (w/w) of PS in the active layer. This reduction leads to a maximum EQE of only 5 %, as displayed in Figure 6.10(c) (red curve). Even with this higher amount of PS, a solution-processed PO-T2T layer still damages the underlying film, resulting in no measurable luminance (Figure 6.10(b), black, dashed line) and a J-V curve dominated by leakage current (black, filled symbols). Consequently, no EQE can be determined.

This subsection has highlighted both the potentials and limitations of 4CzFCN as an emitter. It was demonstrated that 4CzFCN can be successfully processed from solution and blended with a host material. Additionally, the application of a second layer to fix the recombination zone in the middle of the device, thereby suppressing loss processes at the metallic cathode, proved to be successful. However, the dilution of 4CzFCN in PS did not yield the desired results, drastically diminishing OLED performance. Consequently, the solution processing of the second PO-T2T layer could not be successfully performed. Thus, in the next subsection, the focus will shift to exploring another emitter to identify a suitable system in which the emitter can be successfully blended with PS and the second layer solution processed on top.

6.3.2. 2tCz2CzBN as solution processable emitter blended with an insulating polymer

As of writing this thesis, this subsection is prepared as a manuscript for publication under the title “Solution-processed organic light-emitting diodes based on a thermally activated delayed fluorescence emitter blended with an insulating polymer” together with Gert-Jan A. H. Wetzelaer and Paul W. M. Blom.

Author contributions.

David Trieb performed the experiments, analyzed the data and wrote the manuscript. Gert-Jan A. H. Wetzelaer and Paul W. M. Blom proposed and supervised the project and corrected the manuscript.

Introduction

In the field of emitter development Tang and Co-workers published an emitter called 2,6-di(9H-carbazol-9-yl)-3,5-bis(3,6-di-tert-butyl-9H-carbazol-9-yl)benzonitrile (2tCz2CzBN).[174] [175] This blue TADF emitter can be solution processed. With a multilayer structure consisting of 7 layers they achieved for an undoped 2tCz2CzBN emissive layer a maximum EQE of 21.6 %.[176]

Recently, it has been shown that blending semiconducting polymers with an insulating polymer can paradoxically improve the charge transport of the film by means of the dilution of charge traps.[153] As a result of the reduced trap density, the efficiency of polymer OLEDs was increased while reducing material costs at the same time, as the emissive layer can consist of up to 90 % of a cheap insulator, such as polystyrene.[120, 154] Here, the use of polystyrene as an insulating host for a TADF emitter is explored. It is demonstrated that blends of the TADF-emitter 2tCz2CzBN with polystyrene can be used in highly efficient solution-processed OLEDs, with an even improved efficiency compared to the thermally evaporated counterpart. Here, it is demonstrated that the use of polystyrene can render the emissive layer resistant to solution processing of a layer on top. As a proof of principle, fully solution-processable TADF OLEDs by means of using polystyrene in the emissive layer is demonstrated. The results therefore show the combined advantage of increased stack integrity and reduced costs by using an insulating polymer as a host in solution-processed OLEDs.

Results and Discussion

First, OLEDs based on evaporated 2tCz2CzBN were fabricated. In Figure 6.11(a), a schematic energy-level diagram of the device is shown. For hole injection the ITO-anode is covered with a layer of PEDOT:PSS, on top of which a layer of poly(vinyl carbazole) (PVK) with a thickness of 15 nm is spin coated.. The insertion of the PVK-layer between the PEDOT:PSS and the emitter blocks the electron leakage and improves the hole injection.[177] For the emissive layer, 2tCz2CzBN was chosen, which has a sky-blue emission spectrum. Additionally, an electron-transport and hole-blocking layer of PO-T2T was used. For electron injection, a thin (4 nm) tunneling 2,2',2''-(1,35-Benzinetriyl)-tris(1-phenyl-1-H-benzimidazole) (TPBi) interlayer was used in combination with a LiF(1 nm)/Al contact. The TPBi interlayer enables electronic decoupling between the PO-T2T layer and the cathode, to achieve ohmic electron injection.[59]

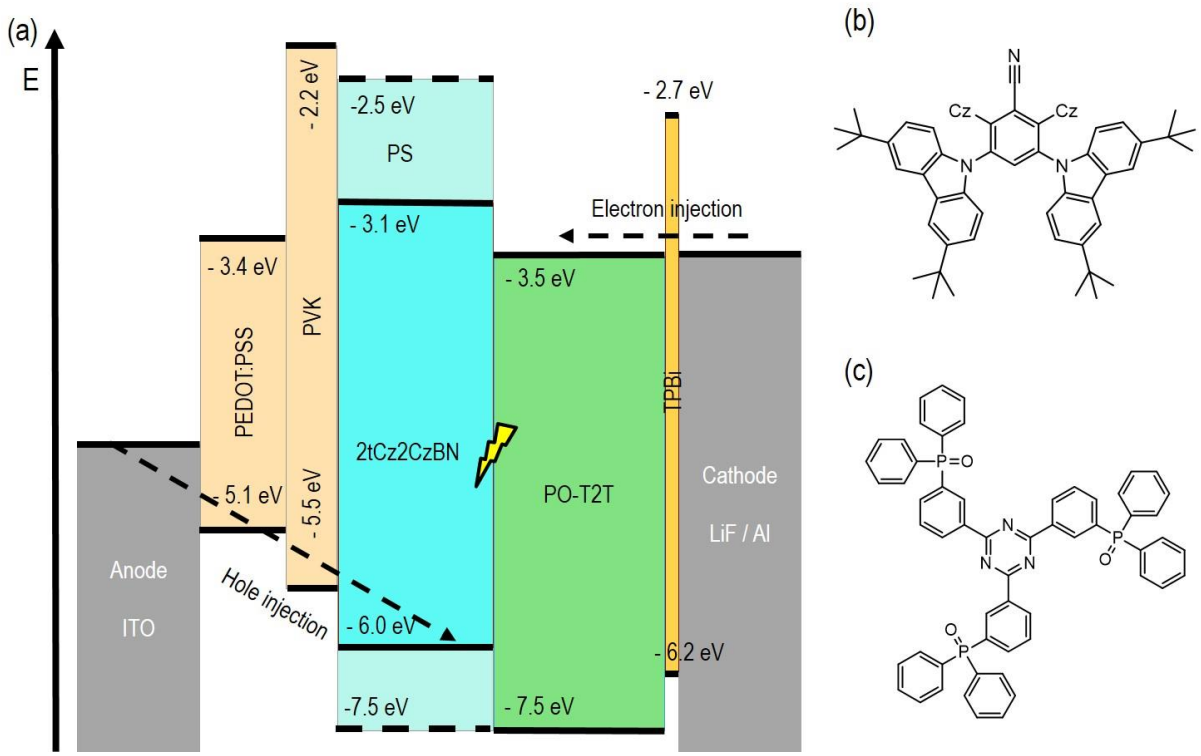

Figure 6.11 (a) Device sketch showing the different layers for the OLED design used in this study. Energy levels of the materials in respect to the vacuum energy are shown as well for all the materials used. The lighting symbol at the interface between 2tCz2CzBN and PO-T2T shows the recombination zone for this OLED. (b) The molecular structure of the TADF-emitter 2tCz2CzBN where Cz represents a carbazole unit. (c) The molecular structure of the electron transport material PO-T2T.

As a reference for the solution-processed OLEDs, a control device is fabricated, in which 2tCz2CzBN and PO-T2T were both evaporated. The current-density and luminance vs voltage characteristics are displayed in Figure 6.12(a). The turn-om voltage determined at 1 cd m^{-2} was 2.7 V. The EQE (Fig. 11(b)) reaches a maximum of 19.7 % at 8 cd m^{-2}, At a luminance of 100, the EQE is 18.0 %, which is higher than the reported 11.6 % for multilayer OLEDs with 2tCz2CzBN at 100 cd m^{-2}.[176] The electroluminescence-spectra (Figure 6.12(c)) exhibit a maximum at 493 nm, corresponding to sky-blue emission.

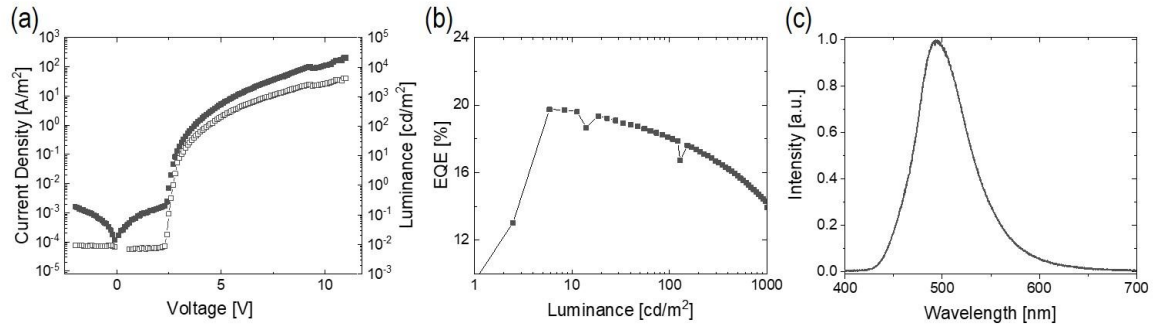

Figure 6.12. Characteristics for a device, where 2tCz2CzBN and PO-T2T were both evaporated with the following device structure: ITO/PEDOT:PSS/PVK/2tCz2CzBN/PO-T2T/TPBi/LiF/Al. Here (a) shows the current density (filled squares) and Photocurrent (empty squares) versus voltage graph, (b) the EQE versus luminance and (c) the Electroluminescence spectra of this device.

With the OLED based on an evaporated emissive layer and electron-transport layer, a proper benchmark for the solution-processed devices is established. As a next step, the 2tCz2CzBN-layer was solution processed from toluene, while keeping the rest of the OLED stack the same. The device characteristics are displayed in Figure 6.14. While the brightness reaches comparable levels compared to the OLED with an evaporated 2tCz2CzBN layer, a higher turn-on voltage (5.0 V @ 1 cd m^{-2}) is observed, potentially indicating compromised charge injection. The EQE at 100 cd m^{-2}, however, equals 17.9 %, which is comparable to the OLED with an evaporated 2tCz2CzBN emissive layer.

To explore if the electron-transport layer, PO-T2T can also be processed from solution, electron-only devices of this material in an Al(30 nm)/PO-T2T/TPBi(4 nm)/LiF(1 nm)/Al(100 nm) structure have been fabricated, where PO-T2T is either evaporated or solution-processed. For evaporated PO-T2T a thickness of 50 mn was determined, for solution processed PO-T2T 89 nm. It is found that PO-T2T dissolves well in ethanol, which would be an orthogonal solvent for the emissive layer. As show in Figure 6.13, the electron current for the PO-T2T single-carrier devices is very similar for the evaporated and the solution-processed layer. Only a shift in the built-in voltage is observed, which is likely due to the effect of the solvent on the work function of the Al bottom electrode. The charge transport of the evaporated and solution-processed PO-T2T is almost identical, as also evidenced by the same temperature dependence of the electron current. Therefore, solution processing of the PO-T2T electron-transport layer seems a viable option.

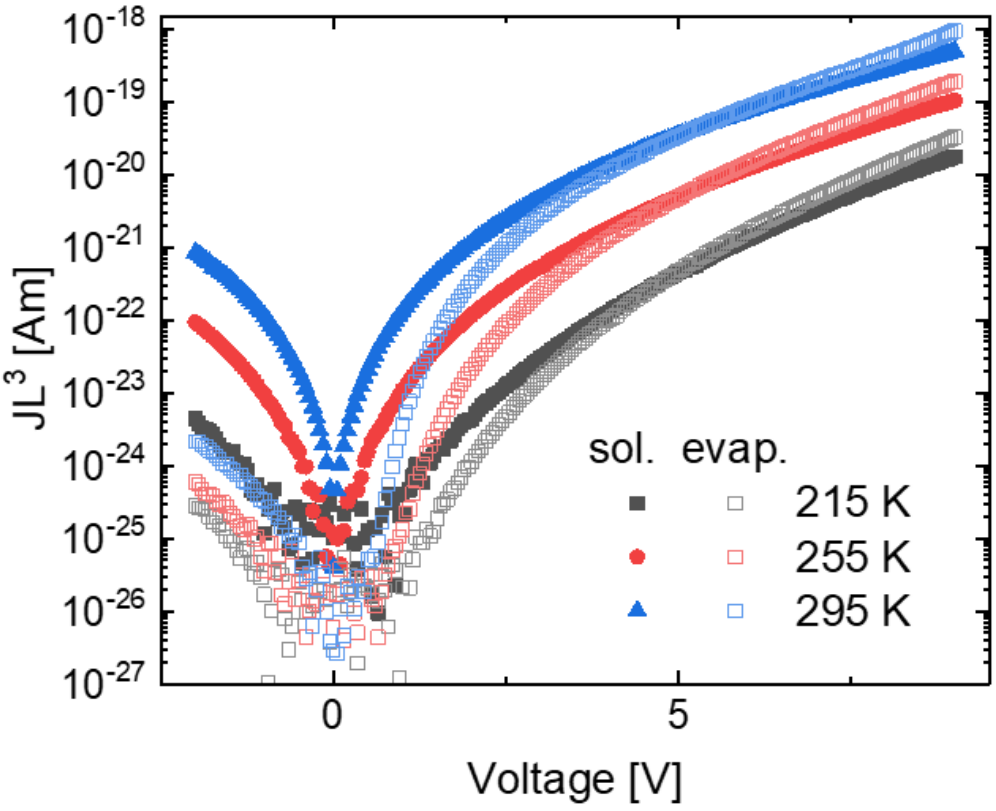

Figure 6.13. Electron only device characteristics of PO-T2T, which is either solution, processed from Ethanol (filled symbols) or evaporated (empty symbols). The data for both devices is recorded at different temperatures. The device structure for the devices was Al/PO-T2T/TPBi/LiF/Al.

Even though 2tCz2CzBN is insoluble in ethanol, it is found that spin coating ethanol on top of a 2tCz2CzBN layer completely removes the film. This demonstrate that the small-molecular film is unable to resist the physical forces associated with spin coating a solution on top. To improve the mechanical resistance of the emissive layer, the possibility of blending the emitter with an insulating polymer, in this case polystyrene were explored. Previous research has shown that blending semiconducting polymers with insulation polymers results in improved electrical characteristics, which comes from a mechanism referred to as “trap dilution”. A second advantage is that the material costs reduce substantially, as the fraction of the cheap insulating polymer in the film can be up to 90 %. If this strategy can also be applied to small-molecular emitters is currently unknown. Therefore, blends of 2tCz2CzBN and PS were used as an emissive layer with an evaporated PO-T2Tlayer in the OLEDs described here. In these blended films the amount of the emitter 2tCz2CzBN was fixed to 33 % (w/w). Blends with PS of different molecular weight were compared, as displayed in Figure 6.14 (for details to the used PS see Table 6.1 in the experimental section). Compared to the OLEDs with neat 2tCz2CzBN, the OLEDs based on the PS-blended emissive layers show a lower current density. The lower current density is expected, as the average distance between the semiconducting (2tCz2CzBN) molecules increases. This effect is larger than in blends of conjugated polymers with insulators, as the long conjugated chains create percolation pathways even at very high insulator fractions. Nevertheless, even at 67 % (w/w) PS, a significant current density is obtained for the 2tCz2CzBN OLEDs, with a correspondingly high brightness. No significant effects of the polystyrene molecular weight were observed.

The EQE of the devices with a blend of PS with 2tCz2CzBN (Figure 6.14(c)) reaches a maximum of 22.8 % and is comparable for all three different PS molecular weights. As a result, the maximum EQE is larger than observed for devices with a neat film of 2tCz2CzBN, independent of the deposition method of 2tCz2CzBN. At a luminance of 100 cd m^{-2} for all PS-based OLEDs, an EQE of 17.7 % is determined. This value is virtually identical to the value obtained for OLEDs based on solution-processed and evaporated neat films of 2tCz2CzBN. As a result, blending the emitter with a large fraction of polystyrene results in highly efficient solution-processed TADF OLEDs.

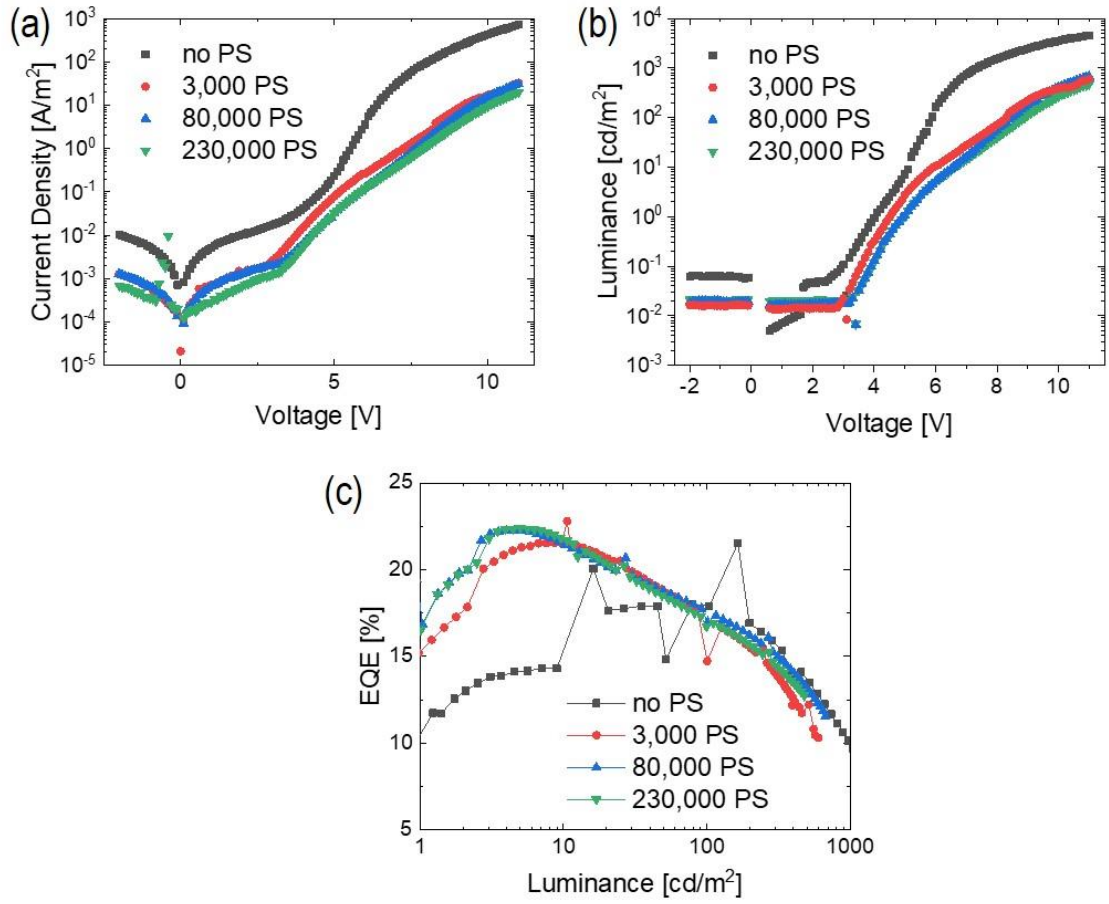

Figure 6.14. Solution processed layers of 2tCz2CzBN as neat film (black) or as blend with polystyrene with different molecular mass. The amount of polystyrene is 66 % (w/w) for all blends, where the molecular mass of PS varies from 3,000 $\frac{g}{mol}$ (red), over 80,000 $\frac{g}{mol}$ (blue) to 230,000 $\frac{g}{mol}$ (green). The device structure for the devices is ITO/PEDOT:PSS/PVK/4CzFCN-PS/PO-T2T (evaporated)/TPBi/LiF/Al. (a) Here the current density versus voltage behavior is shown for all devices mentioned before. (b) Here the photocurrent versus voltage behavior is shown for all the devices mentioned before. (c) Here the EQE versus luminescence is shown for all the devices mentioned before.

As a next step, it is investigated whether the addition of PS increases the resistance of the emissive layer to spin coating a subsequent layer. Therefore, the solvents ethanol and isopropanol were spin coated on top of the PS-diluted emissive layer. Spin coating of the pure solvents did not affect the layer thickness, indicating that the addition of PS reinforces the emissive layer substantially, as pristine 2tCZ2CzBN was completely washed away in the same experiment. To further explore the effect of spin coating solvents on top of the emissive layer, OLEDs were fabricated, in which pure ethanol or isopropanol was spin coated on top, before evaporating the PO-T2T electron-transport layer.

In Figure 6.16, the OLED characteristics are shown after exposing the emissive layer to solvent by means of spin coating. Compared to the devices without solvent exposure (blue symbols in Figure 6.16(a)) the effect on the current density is insignificant. The same applies to the electroluminescence were no difference in the spectra with and without alcohol treatment can be observed, as displayed in Figure 6.15(b).

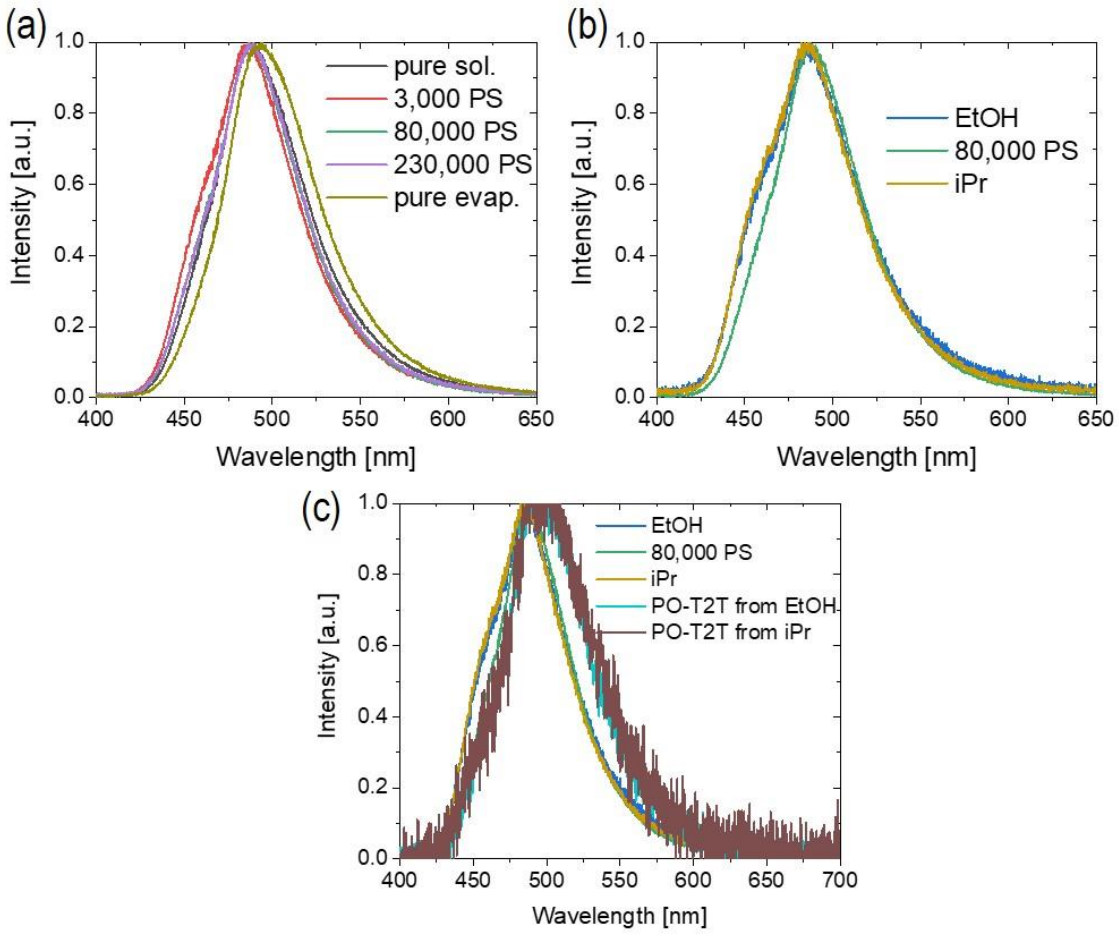

Figure 6.15. Electroluminescence spectra for all devices presented in this study. (a) Electroluminescence spectra for devices with solution processed 2tCz2CzBN, evaporated 2tCz2CzBN and blends of 2tCz2CzBN with PS with different molar mass. (b) Electroluminescence spectra for devices where the emissive layer is a blend of 2tCz2CzBN with 80,000 PS, where the surface is not threated (green), threated with EtOH (blue) or isopropanol (ocher). (c) Electroluminescence spectra as in b added with the electroluminescence spectra for devices where the PO-T2T is solution processed from ethanol (turquoise) or isopropanol (brown).

However, the device exposed to ethanol shows a slightly higher leakage current, which may indicate a small effect of ethanol on the underlying layer. This is also reflected in the EQE, which is lowered to a maximum of 12.6 % in the case of ethanol exposure. For the isopropanol-exposed emissive layer, the OLED exhibits a maximum EQE of 17.1 %. The EQE at a luminance of 100 cd m^{-2} for the devices treated with isopropanol reduces further to 9.8 %, with ethanol to 8.1 %. While these values are lower compared to the OLEDs in which the emissive layer is not exposed to an alcohol, still decent EQEs are achieved, demonstrating that the addition of polystyrene is effective in increasing the resistance of the layer to solvent exposure. The hypothesis to explain this behavior is the OH-Group of the alcohols used in these devices. The OH-Groups could be the origin of electron traps .[72] The lower EQE of the devices treated with ethanol compared to isopropanol could be explained with the fact that ethanol is primary alcohol, whereas isopropanol is a secondary alcohol. So, for ethanol the OH-group is far more exposed to the organic semiconductor compared to the more shielded OH-group in isopropanol. In that case, the amount of electron traps in the ethanol treated device would be larger as compared to the isopropanol threated device. Therefore, a larger drop in efficiency is not unexpected for the device treated with ethanol.

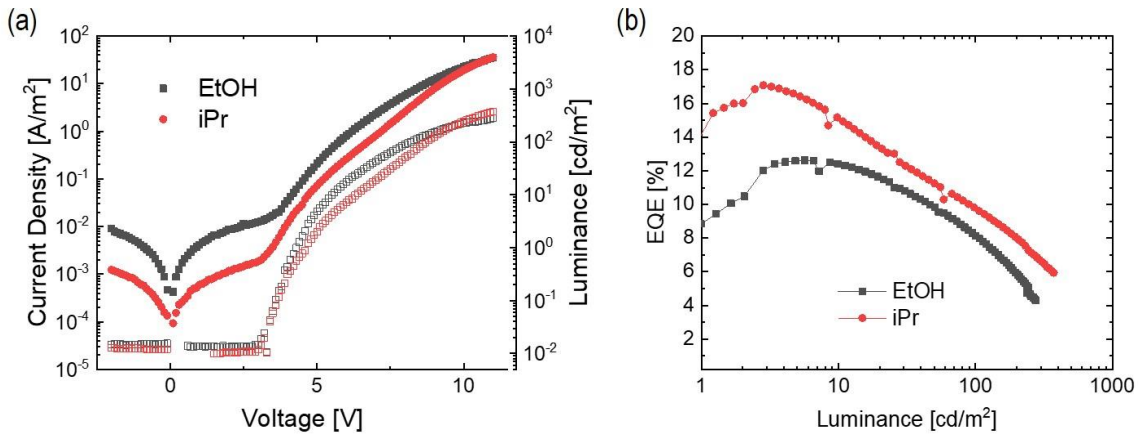

Figure 6.16. Influence of solvents to 2tCz2CzBN-PS blended layers. After spincoating the 2tCz2CzBN-PS layer, Ethanol (black) or Isopropanol (red) where spincoated on top of 2tCz2CzBN-PS layer. Thereafter, PO-T2T was evaporated. The full device structure is ITO/PEDOT:PSS/PVK/2tCz2CzBN-PS/PO-T2T/TPBi/LiF/Al. (a) Current density (filled symbols) and photocurrent density (empty symbols) versus voltage characteristics of the device mentioned above. (b) EQE versus luminescence characteristics for the devices mentioned above.

Since the emissive layer is more resistant to subsequent spin coating by the addition of polystyrene, it is investigated if fully solution-processed OLEDs are feasible by spin coating the PO-T2T as well. For these devices, the emissive layer consists again of a blend of 2tCz2CzBN and 80,000 PS, where the amount of PS is 67 % by weight. The PO-T2T layer was then processed from either isopropanol or ethanol. As is evident from the current density and luminance characteristics in Figure 6.17(a), the current density and luminance are slightly reduced. Again, it is observed, that the use of ethanol as a solvent leads to a higher leakage current.

At higher voltage, the luminance seems to saturate, which was not observed for devices with an evaporated electron-transport layer. The origin of this effect is currently unclear. The EQE of the fully solution processed devices (Figure 6.17(b)) is 11.2 % and 10.2 % for PO-T2T layers processed from ethanol and isopropanol, respectively. The lower efficiency when using isopropanol does not originate from the solvent itself (Figure 6.17), indicating that the film formation of PO-T2T may be inferior when processed from isopropanol, compared to ethanol. Nevertheless, these experiments demonstrate that a fully solution-processed OLED is feasible when reinforcing the emissive layer with polystyrene.

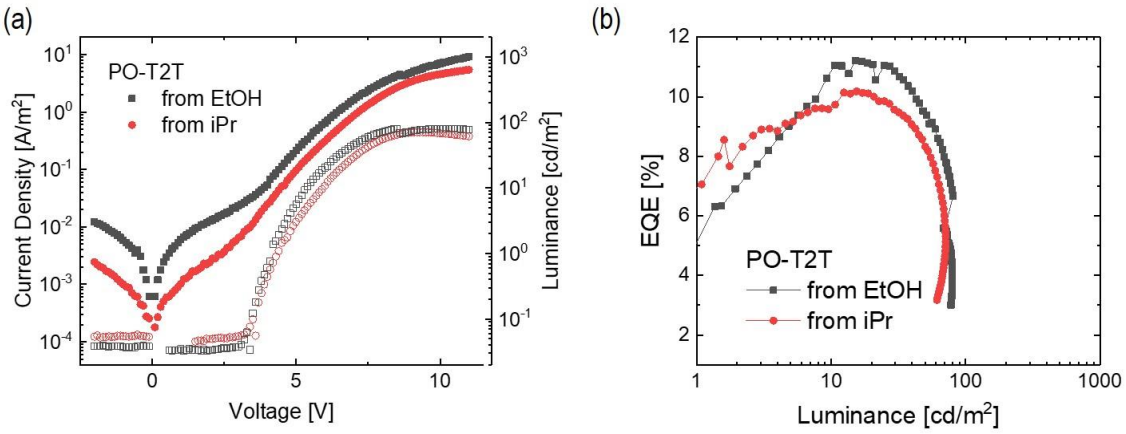

Figure 6.17. Device characteristics for a device, where the 2tCz2CzBN-PS blend as well as the PO-T2T is processed from solution. PO-T2T is processed from either Ethanol (black) or isopropanol (red). The full device structure is ITO/PEDOT:PSS/PVK/2tCz2CzBN-PS/PO-T2T/TPBi/LiF/Al. (a) Current density (filled symbols) and photocurrent density (empty symbols) versus voltage characteristics for the devices mentioned above. (b) EQE versus luminance characteristics for the device mentioned above

Conclusion

In conclusion, it was demonstrated that blending a TADF emitter with polystyrene can result in increased stack integrity in solution-processed OLEDs. The use of an insulator in the emissive layer did not reduce the EQE, maintaining values of above 20 % for sky-blue OLEDs. It was shown that it is possible to deposit an electron-transport layer from an alcohol solution on top of the polystyrene-blended emissive layer, whereas an emissive layer of the pristine TADF emitter is completely removed upon exposure to an alcohol by means of spin coating. While the fully solution-processed OLED stack is not as efficient as solution-processed devices with an evaporated electron-transport layer, the use of cheap polymer insulators as host materials is a viable option from the perspective of stack integrity and material costs in solution-processed OLEDs.

6.4. Conclusion

In summary, this chapter discusses strategies aimed at establishing a fully solution-processed OLED. However, it also highlights several challenges that must be overcome. For the simplest system of a single-layer OLED, numerous requirements are imposed on the emitter, including balanced charge transport and a high PLQY to function efficiently. Developing an emitter that meets all these criteria while also being solution-processable has thus far proven to be challenging. Additionally, the chapter demonstrates that even for emitters that can be successfully dissolved, this does not guarantee that they can be solution-processed to form an organic semiconducting film. This underscores the importance of the morphology of organic semiconductor films in ensuring proper device function.

As the fabrication of single-layer devices from solution remains unattainable due to the absence of suitable emitters, attention is redirected towards processing more traditional multilayer systems from solution. However, challenges arise in ensuring the stability of underlying layers against the forces exerted during the solution processing of subsequent layers. One approach to address this issue involves diluting the emissive layer in an insulating

polymer like PS. Success in this regard depends on the morphology of the emissive film, which may not always be optimal. If successful, a second layer can be solution processed on top using the orthogonal solvent method. While it has been found that the ETL material PO-T2T can be successfully processed from solution, challenges persist in processing PO-T2T atop the emissive layer, as the solvent used appears to damage the underlying layer.

6.5. Experimental Section

This section provides the used materials and methods for the experiments presented in this section

Materials

5,10-Bis(4-(9H-carbazol-9-yl)-2,6-dimethylphenyl)-5,10-dihydroboranthrene (CzDBA), 5,10-Bis(4-(3,6-di-tert-butyl-9H-carbazol-9-yl)-2,6-dimethylphenyl)-5,10-dihydroboranthrene (tBuCzDBA), 10-(4-(4,6-Diphenyl-1,3,5-triazin-2-yl)phenyl)-9,9-dimethyl-9,10-dihydroacridine (DMAC-TRZ), 10,10'-(4,4'-Sulfonylbis(4,1-phenylene))bis(9,9-dimethyl-9,10-dihydroacridine (DMAC-DPS), Bis[4-(9,9-dimethyl-9,10-dihydroacridine)phenyl]methanone (DMAC-BP), 2,2',2"-(1,3,5-Benzinetriyl)-tris(1-phenyl-1-H-benzimidazole) (TPBi), Bathocuproine (BCP), 2,4,6-Tris[3-(diphenylphosphinyl)phenyl]-1,3,5-triazine (PO-T2T), 2,3,4,6-tetrakis(9H-carbazole-9-yl)−5-fluorobenzonitrile (4CzFCN) and 9-[4-(4-Carbazol-9-yl-2-methylphenyl)-3-methylphenyl]carbazole, 9,9'-(2,2'-Dimethylbiphenyl-4,4'-diyl)bis(9H-carbazole) (CDBP) were purchased from Ossilla Ltd. Ethanol dried (max 0.01 % water) and 2-propanol 99.9 % (isopropanol, iPr) were purchased from Merck KGaA. Poly(3,4-ethylenedioxythiophene) polystyrene sulfonate (PEDOT:PSS) were purchased as Clevios^{TM} PEDOT:PSS from Heraeus. Poly(N-Vinylcarbazole) (PVK) were purchased from Polysciences Inc. 2,6-di(9H-carbazol-9-yl)-3,5-bis(3,6-di-tert-butyl-9H-carbazol-9-yl)benzonitrile (2tCz2CzBN) were synthesized by Daniel G. Congrave and Hugo Bronstein from the university of Cambridge, Cambridge, UK. ethanesulfonyl fluoride, 2-[1-[difluoro-[(trifluoroethenyl)oxy]methyl]-1,2,2,2-tetrafluoroethoxy]-1,1,2,2,-tetrafluoro-, with tetrafluoroethylene (Nafion) was purchased from FUJIFILM Wako Pure Chemical Coroporation. All these materials were used without further purification. Chlorobenzene, chloroform, toluene were purchased from Fisher chemicals and purified by an MBSPS5 from MBAUN.

The used polystyrenes all synthesized in house. Their properties are listed in Table 6.1.

Table 6.1. Used polystyrenes in this study and their properties.

Name in this thesis	$\bar{M}_n$ / $\frac{\mathbf{g}}{\mathbf{mol}}$	$\bar{M}_w$ / $\frac{\mathbf{g}}{\mathbf{mol}}$	Đ
3,000 PS	2,735	2,896	1.06
80,000 PS	83,832	86,042	1.03
230,000 PS	222,161	238,890	1.07

Device fabrication

Cleaning of the substrates was done as described in Chapter 4.

For hole injection, PEDOT:PSS was processed as described in Chapter 4. As alternative for the OLEDs using tBuCzDBA, PEDOT:PSS mixed with Nafion was used. Therefore, 3000 µl of PEDOT:PSS were mixed with 4572 µl water and 1800 µl of Nafion. The solution was stirred for 16h and the spin-coated on top the pre-cleaned substrates with 1000 rpm for 3 seconds and subsequently with 3000 rpm for 60 seconds and afterwards annealed for 10 minutes at 120°C. For the OLEDs with 2tCz2CzBN and 4CzFCN, PVK was solution processed on top of the PEDOT:PSS from a solution of PVK dissolved in chlorobenzene at a concentration of 5 mg ml^{-1}. This solution was spincoated under inert conditions for 60 seconds at 3000 rpm and subsequently annealed for 10 minutes at 100°C.

tBuCzDBA was processed from toluene at a concentration of 15 mg ml^{-1}. For the PS-blends, 3,000 PS was used also at a concentration of 15 mg ml^{-1}. The spincoating of these layers were done at 1000 rpm for 60 seconds and subsequently with 4000 rpm for 30 seconds. BCP was solution processed as described in Chapter 5.

DMAC-DPS was dissolved in chloroform at a concentration of 12 mg ml^{-1}. DMAC-TRZ was dissolved in chloroform at a concentration of 12 mg ml^{-1}. DMAC-BP was tried to be dissvoled in chlorobenzene at a concentration of 10 mg ml^{-1}. All solutions were spincoated at 1000 rpm for 60 seconds and subsequently with 4000 rpm for 30 seconds.

Pure 4CzFCN was dissolved in chlorobenzene at a concentration of 10 mg ml^{-1}. For the blends of 4CzFCN with CDBP both materials were dissolved on chlorobenzene at mixed to give a total concentration of 10 mg ml^{-1}, containing 25 % (w/w) 4CzFCN and 75 % (w/w) CDBP. For the blends with PS, a solution of 3,000 PS was added to this solution. All of these solutions were spincoated at 1000 rpm for 60 seconds and subsequently with 4000 rpm for 30 seconds.

2tCz2CzBN and the 2tCz2CzBN-PS blends were dissolved in Toluene with a total concentration of 10 mg ml^{-1}. For the 2tCz2CzBN-PS blends the amount of PS was 66 % (w/w). These solutions were spincoated with 2000 rpm for 60 seconds.

PO-T2T was dissolved either in ethanol or isopropanol with a concentration of 15 mg ml^{-1}. It was spincoated with 3000 rpm for 60 seconds.

If the materials were not solution processed, they were evaporated using a COAT340-ORG organic Evaporation system from Vactec at a vacuum of $1 \cdot 10^{-6}$ mbar.

Metals were evaporated using a COAT340 evaporation system from Vactec at a vacuum of $5 \cdot 10^{-7}$ mbar.

In the following, the device structures for the devices discussed in this chapter are listed.

- Al / tBuCzDBA with PS / BCP / Ba / Al
- ITO / PEDOT:PSS with Nafion / tBuCzDBA (with and without PS) / BCP / Ba / Al
- ITO / PEDOT:PSS with Nafion / tBuCzDBA (with and without PS) / MoO_3 / Al
- Al / DMAC-DPS / TPBi / Ba / Al
- Al / DMAC-TRZ / TPBi / Ba / Al
- Al / 4CzFCN (with and without PS) / BCP / Ba / Al
- ITO / PEDOT:PSS / PVK / 4CzFCN:CDBP (with and without PS) / PO-T2T / TPBi / LiF / Al
- Al / PO-T2T / TPBi / LiF / Al

- ITO / PEDOT:PSS / PVK / 2tCz2CzBN (with and without PS) / PO-T2T / TPBi / LiF / Al

Device characterization

All electrical measurements were performed with a Keithley 2400 source meter inside a nitrogen-filled glovebox. The light output was measured with a Si photodiode with NIST-traceable calibration. The detection area of the photodiode (1 cm^2) was also larger than the emitting area of the OLEDs measured in this study. To capture all photons, to diode was place close to the OLED but not in contact. To prevent scattered light from the substrate edges or from other sources than the OLED, the sample holder masked the OLED. The electroluminescence spectra were recorded a USB4000-UV-vis-es spectrometer. Thickness measurements were performed with a DektakXT profilometer.

7. Summary and Outlook

This Thesis has elucidated the advantages and challenges of solution processing of organic semiconductors as well as fabricating blends of organic semiconductors with other materials to enhance the film properties.

In a first project, it has been demonstrated that blending organic semiconductor films with materials possessing a high dielectric constant can increase the overall dielectric constant of the films. However, this enhancement comes at the expense of diminished charge transport in the organic semiconductor, rendering such films unsuitable for applications in single-layer OSCs. Future research in the field of single-layer OSCs could focus on synthesizing organic semiconductors with intrinsically increased dielectric constants or on developing dopants that increase the dielectric constant without significantly impacting the morphology of the organic semiconductors and therefore diminish the charge transport.

Moreover, it has been demonstrated that the interlayer strategy, previously established for achieving ohmic hole injection, can also be effectively applied to achieve ohmic electron injection into organic semiconductors. This underscores the broad applicability and versatility of the interlayer concept, providing a straightforward means to generate ohmic contacts by employing a thin interlayer. Additionally, the feasibility of processing the interlayer from solution, utilizing techniques such as spin-coating, has been confirmed. Future research endeavors could extend this solution-processing approach to larger-scale fabrication methods, including printing techniques, thereby facilitating the scalable production of organic electronic devices.

The final project of this thesis centers on employing solution processing methods for OLED fabrication. While recent advancements have demonstrated the feasibility of producing efficient single-layer OLEDs by thermal evaporation, attempts to replicate such systems from solution proved unsuccessful due to the inability to identify an emitter possessing all the requisite characteristics within a single material. Consequently, an alternative approach was pursued, focusing on constructing a multilayer system with solution processing of the necessary layers using the orthogonal solvent method. To stabilize the underlying films against the disruptive forces introduced during spin-coating of the top layer, the organic semiconductor was diluted within a PS matrix. Although this was achieved, along with the successful processing of a second layer using a hydrophilic solvent required for the orthogonal solvent method, the stacking of layers resulted in a significant efficiency loss compared to evaporated systems. Future research directions could explore the quest for suitable emitters for solution-processed single-layer OLEDs or the development of a more stable matrix for emitters during the application of the second layer using the orthogonal solvent method.

In conclusion, solution processing offers a rapid and convenient method for the fabrication of organic semiconductors. However, this approach presents challenges in controlling the morphology of the film during deposition, which remains a bottleneck alongside solubility issues encountered with certain organic semiconductors. Blending organic semiconductors with other materials can broaden the application potential of organic semiconductors.

Nonetheless, as in solution processing, the resulting film's morphology is paramount, determining whether the blended film exhibits organic semiconducting behavior or if these properties are diminished or quenched. Continued research efforts in this area are essential to address these challenges and unlock the full potential of solution-processed organic semiconductors.

8. Used tools

Beside the previously mentioned methods in the experimental section the following methods were applied to work out this thesis. Plotting of the data was done using the software Origin in the 2019 version. AFM-images were processed using Gwyddion. Microscope pictures were edited using ImageJ. The calculation of the EQE was done with a python script written by Yungui Li in 2020. The artificial intelligence (AI) language model ChatGPT 3.5 did spelling and grammar correction of this text. This text was created using Microsoft Office Word.

9. Declaration

I hereby declare that I wrote the dissertation submitted without any unauthorized external assistance and used only source acknowledged in this work. All textual passages which are appropriate verbatim or paraphrased from published and unpublished texts as well as all information obtained from oral sources, are dully indicated and listed in accordance with bibliographical rules. In carrying out this research, I complied with the rules of standard scientific practice as formulated in the statutes of Johannes Gutenberg-University Mainz to insure standard scientific practice.

Date, Place	Signature

10. Acknowledgment

11. References

[1] N. D. Treat, P. Westacott, N. Stingelin, *Annual Review of Materials Research* **2015**, *45*, 459-490.

[2] H. Bronstein, C. B. Nielsen, B. C. Schroeder, I. McCulloch, *Nature Reviews Chemistry* **2020**, *4*, 66-77.

[3] A. Buckley, R. Ragni, A. Operamolla, G. M. Farinola, Z. Wang, M. G. Helander, Z.-H. Lu, L. F. Gildea, J. A. Gareth Williams, Z. Dechun, B. D'Andrade, B. Lüssem, M. Furno, K. Leo, H. Bässler, A. Köhler, M. Gerken, A. V. Tishchenko, M. Cocchi, N. Danz, M. Flämmich, D. Deganello, A. C. Grimsdale, J.-H. Jou, S. Kumar, Y.-C. Jou, A. Lääperi, A. Buckley, C. Yates, J. Meyer, P. Görrn, T. Riedl, S. Prasad, J. Woon Park, C. Kristukat, T. Gerloff, M. Hoffmann, K. Diekmann, *Organic light-emitting diodes (OLEDs)*, Woodhead Publishing Limited, **2013**.

[4] H. C. Longuet-Higgins, L. Salem, *Proceedings of the Royal Society A* **1959**, *251*, 172-185.

[5] W. Brütting, *Physics of Organic Semiconductors*, Wiley-VCH, **2005**.

[6] The Nobel comittee, "The Nobel Prize in Chemistry 2000", to find under https://www.nobelprize.org/prizes/chemistry/2000/summary/, **2000**.

[7] H. Bässler, *physica status solidi (b)* **1993**, *175*, 15-56.

[8] R. M. Metzger, *Unimolecular and Supramolecular Electronics I*, Springer, **2012**.

[9] H. Bässler, A. Köhler, *Electronic Processes in Organic Semiconductors*, Wiley-VCH, **2015**.

[10] E. M. Conwell, *Physical Review* **1956**, *103*, 51-61.

[11] G. Domingo, *Semiconductor Basics: A Qualitative, Non-mathematical Explanation of How Semiconductors Work and How They Are Used*, Wiley VCH, **2020**.

[12] H. Sirringhaus, *Advanced Materials* **2005**, *17*, 2411-2425.

[13] A. Heck, J. J. Kranz, M. Elstner, *Journal on Chemical Theory and Computation* **2016**, *12*, 3087-3096.

[14] R. A. Marcus, *The Journal of Chemical Physics* **1956**, *24*, 966-978.

[15] R. A. Marcus, *Annual Review* **1964**, *15*, 155-196.

[16] N. J. van der Kaap, I. Katsouras, K. Asadi, P. W. M. Blom, L. J. A. Koster, D. M. de Leeuw, *Physical Review B* **2016**, *93*, 140206.

[17] B. Van der Zee, Johannes Gutenberg-Universität Mainz (Mainz), **2022**.

[18] J. H. Burroughes, D. D. C. Bradley, A. R. Brown, R. N. Marks, K. Mackay, R. H. Friend, P. L. Burns, A. B. Holmes, *Nature* **1990**, *347*, 539-541.

[19] M. Kuik, G. J. Wetzelaer, H. T. Nicolai, N. I. Craciun, D. M. De Leeuw, P. W. Blom, *Advanced Materials* **2014**, *26*, 512-531.

[20] S. R. Marder, K.-S. Lee, *Photoresponsive Polymers II*, Springer, **2008**.

[21] S. Griggs, A. Marks, H. Bristow, I. McCulloch, *Journal of Material Chemistry C* **2021**, *9*, 8099-8128.

[22] P. W. M. Blom, *Advanced Materials Technologies* **2020**, *5*, 2000144.

[23] B. Zhang, Y. Cheng, *The Chemical Record* **2019**, *19*, 1624-1643.

[24] K. Philipps, Johannes Gutenberg-Universität Mainz (Mainz), **2021**.

[25] P. Friederich, V. Meded, A. Poschlad, T. Neumann, V. Rodin, V. Stehr, F. Symalla, D. Danilov, G. Lüdemann, R. F. Fink, I. Kondov, F. von Wrochem, W. Wenzel, *Advanced Functional Materials* **2016**, *26*, 5757-5763.

[26] A. Köhler, H. Bässler, *Materials Science and Engineering: R: Reports* **2009**, *66*, 71-109.

[27] C. Adachi, M. A. Baldo, M. E. Thompson, S. R. Forrest, *Journal of Applied Physics* **2001**, *90*, 5048-5051.

[28] B. Minaev, G. Baryshnikov, H. Agren, *Physical Chemistry Chemical Physics* **2014**, *16*, 1719-1758.

[29] C. Adachi, A. S. D. Sandanayaka, *CCS Chemistry* **2020**, *2*, 1203-1216.

[30] D. Volz, M. Wallesch, C. Fléchon, M. Danz, A. Verma, J. M. Navarro, D. M. Zink, S. Bräse, T. Baumann, *Green Chemistry* **2015**, *17*, 1988-2011.

[31] H. Uoyama, K. Goushi, K. Shizu, H. Nomura, C. Adachi, *Nature* **2012**, *492*, 234-238.

[32] F. B. Dias, T. J. Penfold, A. P. Monkman, *Methods and Applications in Fluorescence* **2017**, *5*, 012001.

[33] Y. Tao, K. Yuan, T. Chen, P. Xu, H. Li, R. Chen, C. Zheng, L. Zhang, W. Huang, *Advanced Materials* **2014**, *26*, 7931-7958.
[34] A. Endo, K. Sato, K. Yoshimura, T. Kai, A. Kawada, H. Miyazaki, C. Adachi, *Applied Physics Letters* **2011**, *98*, 083302.
[35] X. Yin, Y. He, X. Wang, Z. Wu, E. Pang, J. Xu, J. A. Wang, *Frontiers in Chemistry* **2020**, *8*, 725.
[36] Y. Xiao, H. Wang, Z. Xie, M. Shen, R. Huang, Y. Miao, G. Liu, T. Yu, W. Huang, *Chemical Science* **2022**, *13*, 8906-8923.
[37] R. Braveenth, K. Raagulan, Y.-J. Kim, B.-M. Kim, *Materials Advances* **2023**, *4*, 374-388.
[38] J. Hou, O. Inganas, R. H. Friend, F. Gao, *Nature Materials* **2018**, *17*, 119-128.
[39] B. G. Krishna, D. S. Ghosh, S. Tiwari, *Chemistry of Inorganic Materials* **2023**, *1*.
[40] A. P. Kulkarni, C. J. Tonzola, A. Babel, S. A. Jenekhe, *Chemistry of Materials* **2004**, *16*, 4556-4573.
[41] G. G. Malliaras, J. C. Scott, *Journal of Applied Physics* **1998**, *83*, 5399-5403.
[42] Y. Shen, A. R. Hosseini, M. H. Wong, G. G. Malliaras, *Chemphyschem* **2004**, *5*, 16-25.
[43] N. B. Kotadiya, Karlsruher Instituts für Technologie (Karlsruhe), **2020**.
[44] A. Kumatani, Y. Li, P. Darmawan, T. Minari, K. Tsukagoshi, *Scientific Reports* **2013**, *3*, 1026.
[45] T. van Woudenbergh, P. W. M. Blom, J. N. Huiberts, in *Advances in Solid State Physics, Vol. 42*, Springer, **2002**, pp. 495-503.
[46] M. Waldrip, O. D. Jurchescu, D. J. Gundlach, E. G. Bittle, *Advanced Functional Materials* **2019**, *30*.
[47] J. C. Scott, G. G. Malliaras, *Chemical Physics Letters* **1999**, *299*, 115-119.
[48] H. Bässler, *Polymers for Advanced Technologies* **1998**, *9*, 402-418.
[49] V. I. Arkhipov, E. V. Emelianova, Y. H. Tak, H. Bässler, *Journal of Applied Physics* **1998**, *84*, 848-856.
[50] A. J. Heeger, I. D. Parker, Y. Yang, *Synthetic Metals* **1994**, *67*, 23-29.
[51] H. Ishii, K. Sugiyama, E. Ito, K. Seki, *Advanced Materials* **1999**, *11*, 605-625.
[52] I. Lange, J. C. Blakesley, J. Frisch, A. Vollmer, N. Koch, D. Neher, *Physical Review Letters* **2011**, *106*, 216402.
[53] M. Oehzelt, N. Koch, G. Heimel, *Nature Communications* **2014**, *5*, 4174.
[54] M. Fahlman, S. Fabiano, V. Gueskine, D. Simon, M. Berggren, X. Crispin, *Nature Reviews Materials* **2019**, *4*, 627-650.
[55] J. C. Blakesley, N. C. Greehnam, *Journal of Applied Physics* **2009**, *106*, 034507.
[56] S. Olthof, W. Tress, R. Meerheim, B. Lüssem, K. Leo, *Journal of Applied Physics* **2009**, *106*, 103711.
[57] B. Lüssem, M. Riede, K. Leo, *physica status solidi (a)* **2012**, *210*, 9-43.
[58] K. Zhang, N. B. Kotadiya, X. Y. Wang, G. J. A. H. Wetzelaer, T. Marszalek, W. Pisula, P. W. M. Blom, *Advanced Electronic Materials* **2020**, *6*, 1901352.
[59] N. B. Kotadiya, H. Lu, A. Mondal, Y. Ie, D. Andrienko, P. W. M. Blom, G. A. H. Wetzelaer, *Nature Materials* **2018**, *17*, 329-334.
[60] N. B. Kotadiya, P. W. M. Blom, G.-J. A. H. Wetzelaer, *Nature Photonics* **2019**, *13*, 765-769.
[61] J. J. M. van der Holst, M. A. Uijttewaal, B. Ramachandhran, R. Coehoorn, P. A. Bobbert, G. A. de Wijs, R. A. de Groot, *Physical Review B* **2009**, *79*, 085203.
[62] P. W. M. Blom, M. J. M. de Jong, M. G. van Munster, *Physical Review B* **1997**, *55*, 656-659.
[63] P. W. M. Blom, M. J. M. de Jong, J. J. M. Vleggaar, *Applied Physics Letters* **1996**, *68*, 3308-3310.
[64] N. B. Kotadiya, A. Mondal, P. W. M. Blom, D. Andrienko, G. A. H. Wetzelaer, *Nature Materials* **2019**, *18*, 1182-1186.
[65] P. Kordt, J. J. M. van der Holst, M. Al Helwi, W. Kowalsky, F. May, A. Badinski, C. Lennartz, D. Andrienko, *Advanced Functional Materials* **2015**, *25*, 1955-1971.
[66] W. F. Pasveer, J. Cottaar, C. Tanase, R. Coehoorn, P. A. Bobbert, P. W. Blom, D. M. de Leeuw, M. A. Michels, *Physical Review Letters* **2005**, *94*, 206601.
[67] M. Pope, H. P. Kallmann, P. Magnante, *The Journal of Chemical Physics* **1963**, *38*, 2042-2043.
[68] C. W. Tang, S. A. VanSlyke, *Applied Physics Letters* **1987**, *51*, 913-915.

[69] G. Hong, X. Gan, C. Leonhardt, Z. Zhang, J. Seibert, J. M. Busch, S. Brase, *Advanced Materials* **2021**, *33*, e2005630.
[70] J. Shinar, *Organic Light-Emitting Devices*, Springer, **2004**.
[71] H. Kim, C. M. Gilmore, A. Piqué, J. S. Horwitz, H. Mattoussi, H. Murata, Z. H. Kafafi, D. B. Chrisey, *Journal of Applied Physics* **1999**, *86*, 6451-6461.
[72] H. F. Haneef, A. M. Zeidell, O. D. Jurchescu, *Journal of Materials Chemistry C* **2020**, *8*, 759-787.
[73] B. van der Zee, Y. Li, G. J. A. H. Wetzelaer, P. W. M. Blom, *Advanced Electronic Materials* **2022**, *8*.
[74] S. W. Culligan, A. C. A. Chen, J. U. Wallace, K. P. Klubek, C. W. Tang, S. H. Chen, *Advanced Functional Materials* **2006**, *16*, 1481-1487.
[75] R. Meerheim, M. Furno, S. Hofmann, B. Lüssem, K. Leo, *Applied Physics Letters* **2010**, *97*, 253305.
[76] Y. Li, N. B. Kotadiya, B. Zee, P. W. M. Blom, G. J. A. H. Wetzelaer, *Advanced Optical Materials* **2021**, *9*.
[77] G. Zhang, C. Xie, P. You, S. Li, *Introduction to Organic Electronic Devices*, Springer, **2022**.
[78] W. Liu, N. B. Kotadiya, P. W. M. Blom, G. J. A. H. Wetzelaer, D. Andrienko, *Advanced Materials Technologies* **2020**, *6*, 2000120.
[79] J.-H. Lee, C.-H. Chen, P.-H. Lee, H.-Y. Lin, M.-k. Leung, T.-L. Chiu, C.-F. Lin, *Journal of Materials Chemistry C* **2019**, *7*, 5874-5888.
[80] N. I. Craciun, J. Wildeman, P. W. Blom, *Physical Review Letters* **2008**, *100*, 056601.
[81] G. A. H. Wetzelaer, M. Kuik, H. T. Nicolai, P. W. M. Blom, *Physical Review B* **2011**, *83*, 165204.
[82] L. M. Rosenberg, M. A. Lampert, *Journal of Applied Physics* **1970**, *41*, 508-521.
[83] P. W. M. Blom, M. J. M. de Jong, S. Breedijk, *Applied Physics Letters* **1997**, *71*, 930-932.
[84] G. J. A. H. Wetzelaer, N. J. Van der Kaap, L. J. A. Koster, P. W. M. Blom, *Advanced Energy Materials* **2013**, *3*, 1130-1134.
[85] W. Shockley, W. T. Read, *Physical Review* **1952**, *87*, 835-842.
[86] R. N. Hall, *Physical Review* **1952**, *87*, 387-387.
[87] B. Van der Zee, Y. Li, G. A. H. Wetzelaer, P. W. M. Blom, *Advanced Materials* **2022**, *34*, e2108887.
[88] K. Thakur, B. van der Zee, G. J. A. H. Wetzelaer, C. Ramanan, P. W. M. Blom, *Advanced Optical Materials* **2021**, *10*.
[89] I. Rorich, O. V. Mikhnenko, D. Gehrig, P. W. Blom, N. I. Craciun, *Journal of Physical Chemistry B* **2017**, *121*, 1405-1412.
[90] O. Sachnik, Y. Li, X. Tan, J. J. Michels, P. W. M. Blom, G. A. H. Wetzelaer, *Advanced Materials* **2023**, *35*, e2300574.
[91] S. Forget, S. Chenais, D. Tondelier, B. Geffroy, I. Gozhyk, M. Lebental, E. Ishow, *Journal of Applied Physics* **2010**, *108*, 064509.
[92] H. S. Kim, S.-R. Park, M. C. Suh, *The Journal of Physical Chemistry C* **2017**, *121*, 13986-13997.
[93] A. Salehi, X. Fu, D. H. Shin, F. So, *Advanced Functional Materials* **2019**, *29*.
[94] D. Kearns, M. Calvin, *The Journal of Chemical Physics* **1958**, *29*, 950-951.
[95] C. W. Tang, *Applied Physics Letters* **1986**, *48*, 183-185.
[96] G. Yu, J. Gao, J. C. Hummelen, F. Wudl, A. J. Heeger, *Science* **1995**, *270*, 1789-1791.
[97] V. Ivasyshyn, G. Ye, S. Rousseva, J. C. Hummelen, R. C. Chiechi, (Ed.: S. K. Kurinec), **2018**.
[98] N. S. Sariciftci, L. Smilowitz, A. J. Heeger, F. Wudl, *Science* **1992**, *258*, 1474-1476.
[99] M. Hiramoto, S. Izawa, *Organic Solar Cells*, Springer, **2021**.
[100] J. Yu, J. Huang, H. Lin, Y. Jiang, *Journal of Applied Physics* **2010**, *108*, 113111.
[101] D. Bartesaghi, C. Perez Idel, J. Kniepert, S. Roland, M. Turbiez, D. Neher, L. J. Koster, *Nature Communications* **2015**, *6*, 7083.
[102] R. E. Bird, R. L. Hulstrom, *Solar Energy* **1983**, *30*, 563-573.
[103] Z. Zhou, S. Xu, J. Song, Y. Jin, Q. Yue, Y. Qian, F. Liu, F. Zhang, X. Zhu, *Nature Energy* **2018**, *3*, 952-959.
[104] B. Lipovšek, F. Smole, M. Topič, I. Humar, A. R. Sinigoj, *AIP Advances* **2019**, *9*, 055026.

[105] J. Brebels, J. V. Manca, L. Lutsen, D. Vanderzande, W. Maes, *Journal of Materials Chemistry A* **2017**, *5*, 24037-24050.
[106] C. Schmitz, P. Pösch, M. Thelakkat, H.-W. Schmidt, *Physical Chemistry Chemical Physics* **1999**, *1*, 1777-1781.
[107] K. S. Sree Harsha, *Principles of Vapor Deposition of Thin Films*, Elsevier Science, **2006**.
[108] MBraun, "OLEDs / Organic Electronics", to find under https://www.mbraun.com/de/anwendungen/oleds-organische-elektronik.html, **2024**.
[109] Canon, "Technologies in OLED display manufacturing", to find under https://global.canon/en/technology/oled-display-2023s.html, **2023**.
[110] S.-I. Park, Y.-J. Quan, S.-H. Kim, H. Kim, S. Kim, D.-M. Chun, C. S. Lee, M. Taya, W.-S. Chu, S.-H. Ahn, *International Journal of Precision Engineering and Manufacturing-Green Technology* **2016**, *3*, 397-421.
[111] A. Kaliyaraj Selva Kumar, Y. Zhang, D. Li, R. G. Compton, *Electrochemistry Communications* **2020**, *121*.
[112] O. Yildiz, Z. Wang, M. Borkowski, G. Fytas, P. W. M. Blom, J. J. Michels, W. Pisula, T. Marszalek, *Advanced Functional Materials* **2021**, *32*.
[113] Z. Lu, C. Wang, W. Deng, M. T. Achille, J. Jie, X. Zhang, *Journal of Materials Chemistry C* **2020**, *8*, 9133-9146.
[114] A. Teichler, J. Perelaer, U. S. Schubert, *Journal of Materials Chemistry C* **2013**, *1*, 1910-1924.
[115] Y. Diao, L. Shaw, Z. Bao, S. C. B. Mannsfeld, *Energy & Environmental Science* **2014**, *7*, 2145-2159.
[116] N. Sahu, B. Parija, S. Panigrahi, *Indian Journal of Physics* **2009**, *83*, 493-502.
[117] S. Ho, S. Liu, Y. Chen, F. So, *Journal of Phtonics for Energy* **2015**, *5*, 057611.
[118] A. A. Zakhidov, J. K. Lee, H. H. Fong, J. A. DeFranco, M. Chatzichristidi, P. G. Taylor, C. K. Ober, G. G. Malliaras, *Advanced Materials* **2008**, *20*, 3481-3484.
[119] B. S. Yilbas, A. Al-Sharafi, H. Ali, *Self-Cleaning of Surfaces and Water Droplet Mobility*, Science Direct, **2019**.
[120] E. Khodabakhshi, P. W. M. Blom, J. J. Michels, *Applied Physics Letters* **2019**, *114*, 093301.
[121] P. J. Flory, *The Journal of Chemical Physics* **1941**, *9*, 660-660.
[122] M. D. Lechner, K. Gehrke, E. H. Nordmeier, *Makromolekulare Chemie*, Springer, **2014**.
[123] L. J. A. Koster, S. E. Shaheen, J. C. Hummelen, *Advanced Energy Materials* **2012**, *2*, 1246-1253.
[124] S. O. Morgna, W. A. Yager, *Industrial and Engineering Chemistry* **1940**, *32*, 1519-1528.
[125] R. Steyrleuthner, M. Schubert, F. Jaiser, J. C. Blakesley, Z. Chen, A. Facchetti, D. Neher, *Advanced Materials* **2010**, *22*, 2799-2803.
[126] J. Roncali, I. Grosu, *Advanced Science* **2019**, *6*, 1801026.
[127] A. Ullah, A. ur Rahman, C. Won Ahn, M. u. Rahman, A. Ullah, Z. u. Rehman, M. Javid Iqbal, I. W. Kim, *Polymer Engineering & Science* **2015**, *55*, 1396-1402.
[128] H. Bao, J. Song, J. Zhang, Q. Shen, C. Yang, Q. Zhang, *Macromolecules* **2007**, *40*, 2371-2379.
[129] R. Fries, M. Simko, *nano trust dosiers* **2012**, *33*, 1-4.
[130] C. Kasparek, R. Rohloff, J. J. Michels, N. I. Crăciun, J. Wildeman, P. W. M. Blom, *Advanced Electronic Materials* **2017**, *3*.
[131] S. Y. Leblebici, T. L. Chen, P. Olalde-Velasco, W. Yang, B. Ma, *ACS Appl Mater Interfaces* **2013**, *5*, 10105-10110.
[132] N. P. Young, N. P. Balsara, in *Encyclopedia of Polymeric Nanomaterials*, **2014**, pp. 1-7.
[133] X. Zhang, D. Zhang, Q. Zhou, R. Wang, J. Zhou, J. Wang, H. Zhou, Y. Zhang, *Nano Energy* **2019**, *56*, 494-501.
[134] W. Zhu, X. Chen, Q. M. Zhang, *Polymer* **2023**, *285*, 126309.
[135] D. Reyes-Coronado, G. Rodriguez-Gattorno, M. E. Espinosa-Pesqueira, C. Cab, R. de Coss, G. Oskam, *Nanotechnology* **2008**, *19*, 145605.
[136] K. L. Mittal, B. Lindman, *Surfactants in Solution*, Springer, **1984**.
[137] H. Tang, K. Prasad, R. Sanjinès, P. E. Schmid, F. Lévy, *Journal of Applied Physics* **1994**, *75*, 2042-2047.

[138] W. Zhao, S. Li, H. Yao, S. Zhang, Y. Zhang, B. Yang, J. Hou, *Journal of the American Chemical Society* **2017**, *139*, 7148-7151.
[139] A. G. Ricciardulli, B. van der Zee, K. Philipps, G. A. H. Wetzelaer, R. Q. Png, P. K. H. Ho, L. L. Chua, P. W. M. Blom, *APL Materials* **2020**, *8*, 021101.
[140] R. H. Friend, R. W. Gymer, A. B. Holmes, J. H. Burroughes, R. N. Marks, C. Taliani, D. D. C. Bradley, D. A. Dos Santos, J. L. Bredas, M. Lögdlund, W. R. Salaneck, *Nature* **1999**, *397*, 121-128.
[141] B. F. Bory, P. R. F. Rocha, R. A. J. Janssen, H. L. Gomes, D. M. De Leeuw, S. C. J. Meskers, *Applied Physics Letters* **2014**, *105*, 123302.
[142] M. Kröger, S. Hamwi, J. Meyer, T. Riedl, W. Kowalsky, A. Kahn, *Organic Electronics* **2009**, *10*, 932-938.
[143] M. Kröger, S. Hamwi, J. Meyer, T. Riedl, W. Kowalsky, A. Kahn, *Applied Physics Letters* **2009**, *95*, 123301.
[144] J. Hwang, A. Wan, A. Kahn, *Materials Science and Engineering: R: Reports* **2009**, *64*, 1-31.
[145] H. Vázquez, R. Oszwaldowski, P. Pou, J. Ortega, R. Pérez, F. Flores, A. Kahn, *Europhysics Letters (EPL)* **2004**, *65*, 802-808.
[146] L. Gao, Z. G. Zhang, L. Xue, J. Min, J. Zhang, Z. Wei, Y. Li, *Advanced Materials* **2016**, *28*, 1884-1890.
[147] G.-J. A. H. Wetzelaer, M. Kuik, Y. Olivier, V. Lemaur, J. Cornil, S. Fabiano, M. A. Loi, P. W. M. Blom, *Physical Review B* **2012**, *86*, 165203.
[148] A. Ioannidis, J. S. Facci, M. A. Abkowitz, *Journal of Applied Physics* **1998**, *84*, 1439-1444.
[149] J. A. Rohr, D. Moia, S. A. Haque, T. Kirchartz, J. Nelson, *Journal of Physics: Condensed Matter* **2018**, *30*, 105901.
[150] K. H. Lin, G. A. H. Wetzelaer, P. W. M. Blom, D. Andrienko, *Frontiers in Chemistry* **2021**, *9*, 800027.
[151] V. N. Hamanaka, E. Salsberg, F. J. Fonseca, H. Aziz, *Organic Electronics* **2020**, *78*, 105509.
[152] Z. Ma, H. Geng, D. Wang, Z. Shuai, *Journal of Materials Chemistry C* **2016**, *4*, 4546-4555.
[153] D. Abbaszadeh, A. Kunz, G. A. Wetzelaer, J. J. Michels, N. I. Craciun, K. Koynov, I. Lieberwirth, P. W. Blom, *Nature Material* **2016**, *15*, 628-633.
[154] A. Kunz, P. W. M. Blom, J. J. Michels, *Journal of Materials Chemistry C* **2017**, *5*, 3042-3048.
[155] T. L. Wu, J. Lei, C. M. Hsieh, Y. K. Chen, P. Y. Huang, P. T. Lai, T. Y. Chou, W. C. Lin, W. Chen, C. H. Yu, L. Y. Hsu, H. W. Lin, C. H. Cheng, *Chemical Science* **2022**, *13*, 12996-13005.
[156] M. Cinquino, C. T. Prontera, A. Maggiore, A. Zizzari, M. Pugliese, F. Mariano, V. Valenzano, I. E. Palamà, R. Manfredi, G. Gigli, V. Maiorano, *Advanced Electronic Materials* **2023**, *10*.
[157] O. Sachnik, Y. Ie, N. Ando, X. Tan, P. W. M. Blom, G. A. H. Wetzelaer, *Advanced Materials* **2024**, *36*, e2311892.
[158] M. Fatahi, Johannes Gutenberg-Universität Mainz (Mainz), **2022**.
[159] Y. Liu, Y. Wu, T. Wang, Q. Wang, X. Han, X. Wu, H. Tong, L. Wang, *Organic Electronics* **2023**, *113*, 106720.
[160] Q. Zhang, D. Tsang, H. Kuwabara, Y. Hatae, B. Li, T. Takahashi, S. Y. Lee, T. Yasuda, C. Adachi, *Advanced Materials* **2015**, *27*, 2096-2100.
[161] X. Jiang, H. Lin, C. Xue, G. Zhang, W. Jiang, G. Xing, *Journal of Materials Science: Materials in Electronics* **2020**, *31*, 19136-19145.
[162] Z. Liu, F. Cao, T. Tsuboi, Y. Yue, C. Deng, X. Ni, W. Sun, Q. Zhang, *Journal of Materials Chemistry C* **2018**, *6*, 7728-7733.
[163] R. Dhali, D. K. A. Phan Huu, F. Bertocchi, C. Sissa, F. Terenziani, A. Painelli, *Physical Chemistry Chemical Physics* **2021**, *23*, 378-387.
[164] Y. Wada, K. Shizu, S. Kubo, T. Fukushima, T. Miwa, H. Tanaka, C. Adachi, H. Kaji, *Applied Physics Express* **2016**, *9*, 032102.
[165] K. Matsuoka, K. Albrecht, A. Nakayama, K. Yamamoto, K. Fujita, *ACS Appl Mater Interfaces* **2018**, *10*, 33343-33352.
[166] Y. J. Cho, B. D. Chin, S. K. Jeon, J. Y. Lee, *Advanced Functional Materials* **2015**, *25*, 6786-6792.

[167] Z. He, C. Wang, J. Zhao, X. Du, H. Yang, P. Zhong, C. Zheng, H. Lin, S. Tao, X. Zhang, *Journal of Materials Chemistry C* **2019**, *7*, 11806-11812.
[168] W. Jing, D. Song, B. Qiao, Z. Xu, J. Chen, L. Zhou, B. Li, S. Zhao, *Organic Electronics* **2020**, *82*, 105703.
[169] J. Zhao, C. Zheng, Y. Zhou, C. Li, J. Ye, X. Du, W. Li, Z. He, M. Zhang, H. Lin, S. Tao, X. Zhang, *Materials Horizons* **2019**, *6*, 1425-1432.
[170] K. Stavrou, L. G. Franca, A. P. Monkman, *ACS Appl Electron Mater* **2020**, *2*, 2868-2881.
[171] B. van der Zee, Y. Li, G.-J. A. H. Wetzelaer, P. W. M. Blom, *Physical Review Applied* **2022**, *18*, 064002.
[172] S. Tokito, T. Iijima, Y. Suzuri, H. Kita, T. Tsuzuki, F. Sato, *Applied Physics Letters* **2003**, *83*, 569-571.
[173] K. Albrecht, K. Matsuoka, K. Fujita, K. Yamamoto, *Angewandte Chemie International Edition* **2015**, *54*, 5677-5682.
[174] F. M. Xie, S. J. Zou, Y. Li, L. Y. Lu, R. Yang, X. Y. Zeng, G. H. Zhang, J. Chen, J. X. Tang, *ACS Appl Mater Interfaces* **2020**, *12*, 16736-16742.
[175] S. J. Zou, F. M. Xie, M. Xie, Y. Q. Li, T. Cheng, X. H. Zhang, C. S. Lee, J. X. Tang, *Advanced Science* **2020**, *7*, 1902508.
[176] F.-M. Xie, Z.-D. An, M. Xie, Y.-Q. Li, G.-H. Zhang, S.-J. Zou, L. Chen, J.-D. Chen, T. Cheng, J.-X. Tang, *Journal of Materials Chemistry C* **2020**, *8*, 5769-5776.
[177] B. Li, D. Song, Z. Xu, B. Qiao, W. Zheng, J. Yang, W. Jing, S. Zhao, *Organic Electronics* **2020**, *83*, 105721.